UNIVERSITÉ LAVAL
QUÉBEC, CANADA

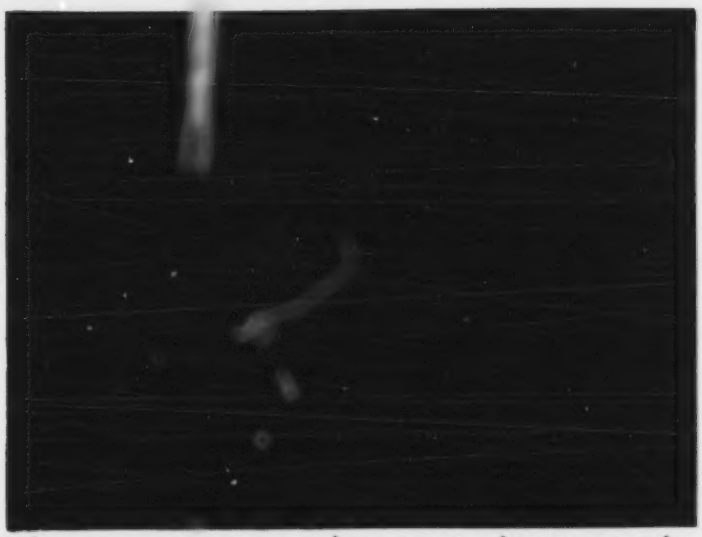

DÉPARTEMENT DE MINES ET MÉTALLURGIE

Work on this project was conducted under the auspices of
the Canada Centre for Mineral and Energy Technology,
Energy, Mines and Resources, Canada.

DSS FILE NUMBER:	12ST.23440-4-9220
DSS CONTRACT SERIAL NO.:	1ST84-00358
CANMET PROJECT NUMBER:	360251
CANMET SCIENTIFIC AUTHORITY:	L.E. COLLINS

ULTRA TO LOW CARBON BORON HSLA* STEELS: INFLUENCE OF ALLOYING AND PROCESSING ON THE TRANSFORMATION KINETICS AND MECHANICAL PROPERTIES (UP-L-263)

FINAL REPORT

by

M.R. Krishnadev (Professor)
S. Dionne (Graduate Student)
Université Laval

171 pp

MICROMEDIA

91-00725/

SUMMARY

In recent years, the need for steels with improved strength and toughness levels for use in energy conversion and transportation systems has led to development of many HSLA steels. However, the use of boron additions in these steels has been limited in spite of the fact that boron is an attractive alloying addition from the point of view of economic and metallurgical considerations. The principal aim of this project was to evaluate the influence of micro and low alloy additions and of prior thermomechanical history of austenite on the transformation kinetics and final mechanical properties of boron-containing extra low carbon HSLA steels.

Relationships were established between the composition, microstructure and mechanical properties of the low carbon,boron-containing,controlled rolled,experimental steels. Compositional ranges investigated were: C = 0.02 to 0.06, B = 0 to 30 ppm and N = 30 to 100 ppm. The influence of the cooling rate on the transformation behaviour of these steels was investigated using deformation dilatometry. Continuous cooling transformation (CCT) diagrams were generated and the optimum amount of boron to be added for satisfactory hardenability was determined. A yield strength of 426 MPa and tensile strength of 600 MPa were achieved in the air cooled base alloy + 16 ppm B whereas the base alloy alone had a yield strength of 409 MPa and a tensile strength of 473 MPa. The effects of carbon, nitrogen and other alloying elements (Ti, Nb, Al, Cu and Mo) on the boron hardenability effect were investigated. The experimental boron containing compositions had similar strength and ductility levels, although some decrease in boron effectiveness and strength was noted for the higher carbon alloys. The results have also brought to light the importance of adequate control of the amount and distribution of inclusions in these steels in order to obtain the desired boron hardenability effect.

It was found that a cooling rate of $8°Cs^{-1}$ improved toughness but did not significantly increase the strength of the steels. All the experimental steels, whether air cooled or accelerated cooled, had excellent low temperature toughness with transition temperatures less than -60°C (55J criterion). These results prove that boron can be used effectively to improve tensile properties without having detrimental effects on the toughness of low carbon controlled rolled steels.

RÉSUMÉ

Les besoins récents en aciers très résistants et tenaces, destinés à l'emploi dans les systèmes de conversion et de transport énergétique, ont conduit au développement de plusieurs nouveaux aciers HSLA. Cependant, en dépit de nombreux avantages aux points de vue économique et métallurgique, le bore a été peu employé comme élément d'alliage lors de l'élaboration de ces aciers. Le principal objectif de ce projet était donc d'évaluer l'influence de faibles additions de certains éléments d'alliage et de l'histoire thermomécanique de l'austénite sur la cinétique de transformation et les propriétés mécaniques finales d'aciers HSLA au bore, à très faible teneur en carbone et ayant subi un laminage contrôlé.

Des relations ont été établies entre la composition, la microstructure et les propriétés mécaniques de ces aciers expérimentaux. La composition des aciers variait entre 0,02 à 0,06% C, 0 à 30 ppm B et 30 à 100 ppm N. L'influence de la vitesse de refroidissement sur la transformation de ces aciers a été étudiée à l'aide de la dilatométrie avec déformation. Les courbes de transformation en refroidissement continu ont été mesurées pour certaines compositions et la quantité optimum de bore à ajouter pour obtenir une trempabilité satisfaisante a été déterminée. Une limite élastique de 426 MPa et une résistance à la traction de 600 MPa ont été obtenues pour l'acier ayant la composition de base + 16 ppm bore. L'acier ayant la composition de base seulement avait une limite élastique de 409 MPa et une résistance à la traction de 473 MPa. L'influence du carbone, de l'azote et d'autres éléments d'alliage (Ti, Nb, Al, Cu, Mo) sur l'effet du bore sur la trempabilité a été étudiée. Tous les aciers expérimentaux avaient des propriétés de résistance et de ductilité semblables. Cependant, on a noté une certaine diminution dans l'efficacité du bore à retarder la transformation austenite-ferrite pour les aciers ayant une teneur en carbone plus élevée. Les résultats ont également mis en évidence la nécessité de contrôler la quantité et la distribution des inclusions dans ces aciers afin d'obtenir un effet optimum du bore sur la trempabilité.

L'utilisation d'une vitesse de refroidissement de $8°Cs^{-1}$ au lieu d'un refroidissement à l'air a résulté en une certaine amélioration de la ténacité de ces aciers mais n'a pas causé d'augmentation significative de leur résistance. Tous les aciers expérimentaux étudiés possédaient une excellente tenacité, qu'ils aient été refroidis à l'air ou de façon accélérée. La température de transition (critère 55J) était inférieure à -60°C dans tous les cas. Les résultats démontrent donc que l'addition de bore permet d'améliorer la résistance sans entraîner d'effets désavantageux sur la ténacité des aciers à faible teneur en carbone ayant subi un laminage contrôlé.

CHAPTER ONE

INTRODUCTION

In recents years, the need for steels with improved strength and toughness levels for use in energy conversion and transportation systems has led to development of many HSLA steels. However, the use of boron additions in these steels has been limited in spite of the fact that boron is an attractive alloying addition from the point of view of economic and metallurgical considerations.

The incentive for the use of boron in steels is derived from the fact that very minute additions (0,0005 to 0,0030 wt%) impart substantial hardenability to the steel. Thus, this element may be used effectively to replace other costly hardenability promoters such as chromium, nickel, molybdenum, manganese and others.

Boron has a synergistic effect with molybdenum in suppressing $\gamma \rightarrow \alpha$ transformation and based on this effect, low carbon Mo-B bainitic steels were developed quite some time ago. Recently it has been found that boron has a similar synergistic effect with niobium. These synergistic effects can be used advantageously to achieve higher section capability in HSLA steels and also realize higher strength levels (> 450 MPa) with leaner compositions. Up to now, the tendency has been to use other alloying elements to achieve this goal due to the difficulty perceived in producing consistent hardenability effect via boron additions and the controversy associated with the influence of boron on toughness and hot shortness. In this context, it is worth while to recall that at present, section capability of HSLA steels is usually limited to 18 mm in the controlled rolled condition and 50 mm in the quench and tempered condition. Also, the

strength levels realized are limited to 480 MPa. Thus there is considerable scope for the use of boron (i.e. the exploitation of boron's influence on the transformation and precipitation kinetics) in HSLA steels, particularly in the light of the need for strong, tough, weldable steels for Arctic structural aplications and heavy section pressure vessel applications. However, to exploit the potential of boron fully, many fundamental and practical aspects of boron usage in controlled rolled HSLA steels need to be clarified.

The principal aim of this project was therefore to evaluate the influence of micro and low alloying elements and prior thermomechanical history of austenite on the transformation kinetics and final mechanical properties of boron containing extra low carbon HSLA (High Strength Low Alloy) steels. The first objective was to investigate the relation between carbon, nitrogen and boron.levels and the hardenability effect of boron. The second objective was to evaluate the effects of other alloying elements (Cu, Mo, Nb, Ti) on the ability of boron to suppress the $\gamma \rightarrow \alpha$ transformation. The third objective was to discover how thermomechanical processing affects the transformation kinetics and final mechanical properties of boron-HSLA steels.

The composition of the experimental steels was based on Nippon steels ULCB Grade 483 line pipe steel: 0,02 C, 1,9 Mn, 0,003 S, 0,04 Nb, 0,016 Ti and 0,001 B (nitrogen around 40 ppm). However the carbon level (0,015 to 0,066%), the nitrogen level (32 to 102 ppm) and the boron level (10 to 37 ppm) were varied considerably to investigate the specific effects of higher nitrogen contents and different boron and carbon contents on boron hardenability. Such a systematic variation in composition was required as Canadian steel makers did not have the capability to achieve simultaneously extra low carbon levels and nitrogen levels and will be reluctant to produce boron HSLA steels until relations between alloy chemistry, process variables and final mechanical properties in these classes of steels are made clear.It is very likely that Canadian steel makers will soon have such capability, and the present results can be readily adapted to their needs. Compositions containing 0,305 Cu and 0,195 Mo were also included so that the results would be of relevance to the development of X-80 grade line pipe for sour gas applications. Steels containing 0,06 C were also prepared so that the results would be of relevance to the development of heavy section steel for offshore structures. To extend the strenght range of compositions and to define the

parameters for adopting "OLAC" (on-line accelerated cooling) technology for the processing of boron HSLA steels, accelerated cooling after final rolling has also been employed.

The knowledge of the effects of composition and cooling rate on the $\gamma \rightarrow \alpha$ transformation is very important as these effects determine to a great extent the final microstructure and consequently, the final mechanical properties. To develop an in-depth understanding of the transformation behaviour of boron-HSLA steels, CCT diagrams were generated using quench-deformation dilatometry. The effects of varying the austenitizing temperature and time, the percentage of hot deformation, deformation temperature and the cooling rate on the transformation behaviour were also evaluated.

Extensive microscopy (optical, SEM, TEM) was used to characterize the microstructural features of plate and dilatometry specimens. The boron distribution was determined using autoradiography. In addition, oblique sectionning techniques were used to relate the fracture characteristics to the microstructure and, in turn, to the mechanical properties.

Mechanical properties were evaluated in the as-rolled as well as in the tempered (600°C - 1 hour) conditions. Tensile tests were carried out to characterize strength and ductility. Instrumented impact testing was used to determine crack initiation and propagation resistance and the dynamic fracture toughness K*d.

CHAPTER TWO

REVIEW OF LITERATURE

2.1 Distribution of Boron in Steel

2.1.1 Boron in Solution

Conflicting opinions exist in the literature as to whether boron forms an interstitial or a substitutional solid solution with iron. The atomic size of boron is borderline for both types of solution. Comparison of diffusion data for boron with that of known interstitials such as carbon and nitrogen seems to indicate that boron is interstitially dissolved in austenite [1,2]. It has been suggested [3] that association of boron atoms with vacancies may help to accommodate the large atomic radius of the boron atoms to interstitial sites. On the other hand, the activation energy for boron diffusion in ferrite is of the order expected for substitutional solid solutions [2].

2.1.2 Segregation of Boron to the Austenite Grain Boundaries

If steel containing boron is maintained at the austenitizing temperature for some time, no segregation of boron to the grain boundaries takes place [77]. Upon cooling from the austenitizing temperature, segregation of the boron to the austenite grains boundaries and/or precipitation of boron-rich phases will occur [3,4,5].

If austenite in which boron is homogeneously dissolved is quenched at very high rates rapid enough, no segregation of boron to the grain boundaries is observed

(2,6,7,77). However, if the quenching rate is lower than some critical value, non equilibrium segregation of boron will take place. A mechanism involving boron-vacancy interactions has been put forward to explain this phenomenon (2,3,4,6,8,77). At a given austenite temperature, boron atoms (B), vacancies (V) and boron-vacancy complexes (C) are in thermodynamic equilibrium:

$$[V] + [B] = [C]$$

During cooling, the steel becomes supersaturated with respect to the vacancies and boron atoms. In an attempt to reestablish equilibrium, the excess vacancies and complexes will tend to move from the middle of the austenite grains towards the boundaries as these constitute infinite vacancy sinks. This will cause grain boundary enrichment in boron as the temperature decreases. For this mechanism to be operative during cooling, the mobility of the complexes must be greater than that of the individual boron atoms and vacancies. If cooling is initiated from higher austenitizing temperatures, a greater concentration of excess vacancies and complexes will exist at lower temperatures and the amount of boron segregated to the grain boundaries will increase.

If cooling rate is slow, an equilibrium concentration of boron atoms and vacancies is maintained in the austenite by the bulk diffusion of the excess vacancies and boron atoms to the grain boundaries. In this case, the equilibrium segregation theory predicts that higher grain boundary concentrations of boron will be achieved at lower austenite temperatures (9):

$$C_{gb} = \frac{A\,C_{gi}\,[\exp(Q/RT)]}{1 + AC_{gi}\,[\exp(Q/RT)]}$$

A is constant.
C_{gi} is the boron concentration in the grain interior.
C_{gb} is the boron concentration in the grain boundary.

When the austenite is deformed at a temperature below the recrystallization stop temperature, the diffusion of the boron atoms is interrupted by the strong deformation. Only a faint boron segregation can then be detected at the deformed austenite grains (10). However, boron atoms will also segregate to defects such as deformation bands and twin boundaries inside the austenite grains giving an

almost uniform appearance to the boron distribution [11,12]. Austenite deformed at a temperature higher than the recrystallization stop temperature will immediately recrystallize after deformation. The boron atoms will be trapped by the sweeping austenite grain boundaries because the sweeping velocity of the boundaries is not much different from the grain boundary diffusion velocity of boron [10,13]. As the temperature decreases, the bulk diffusion of boron will become increasingly important because the sweeping velocity of the boundaries decreases sharply with temperature. Boron segregation to the boundaries will then be enhanced, resulting in intensive profiles of boron at the recrystallized boundaries [10].

In the segregation mechanisms considered above, it was assumed that no interactions occurred between boron and other alloying elements usually encountered in steels. Boron containing phases and their influence on boron segregation and hardenability mechanisms will be examined in the following section

2.1.3 Boron Phases

Boron Nitride

In steels where there is no control of the nitrogen content, the most commonly occurring boron phase is boron nitride. Crystallography of boron nitride has been investigated by Watanabe and Ohtani [7]. The structure of boron nitride is hexagonal close-packed. Boron and nitrogen atoms form two dimensional nets by covalent bonding. Each layer of nets combines with others by Van der Waals forces giving a spherulite morphology similar to that of spherical graphite. Solubility of boron and nitrogen in equilibrium with boron nitride can be described by an equation of the form:

$$[B]\,[N] = K \quad (13)$$

where $K=A \exp(-Q/RT)$ is the solubility product (A is a constant) and [B] and [C] are the boron and nitrogen concentrations respectively. Boron nitrides precipitate upon cooling from the austenitizing temperature. Preferred nucleation sites are sulfide and oxide inclusions such as MnS and Al_2O_3 [14,15,16,17]. Boron nitrides

also precipitate on the austenite grain boundaries because the boron atoms combine with nitrogen atoms after segregation to the boundaries [7,9].

Boron nitride precipitates have a detrimental effect on hardenability as they prevent further atomic boron segregation to the grain boundaries and may act as ferrite nucleation sites. To prevent their formation, the free nitrogen content of the steel must be reduced to below 30 ppm [10,18] by careful steelmaking practice. Boron nitride precipitation may also be controlled by addition of elements like titanium, aluminium and zirconium which are strong nitride formers [4,5,19]. Reducing the number of MnS and Al_2O_3 inclusions [15,16] will also help to insure sufficient free boron for hardenability. High temperature deformation treatments such as forging are also reported to retard precipitation of boron nitride [10,20].

Borocarbides

In steels where the nitrogen content is well controlled (below the 20-30 ppm level) the principal boron rich phase is a borocarbide of the form $M_{23}(C,B)_6$ where M is Fe with possible substitution by Cr, Mn and Mo and where carbon and boron can replace one another to a considerable extent [2,4,15,18,21,22]. The crystal structure of $M_{23}(C,B)_6$ is face-centered cubic [3,23]. $M_{23}(C,B)_6$ is nucleated at the austenite grain boundaries after the beginning of boron segregation and grows with a parallel (cube-cube) orientation relationship to one of the austenite grains [3,4,9,22]. The coherent interface between the precipitate and austenite grains has reduced energy thus inhibiting ferrite nucleation on that side of the grain boundary. The other interface is fully incoherent and may act as a nucleation site for ferrite. If the $M_{23}(C,B)_6$ precipitates are small enough so that they do not provide large extra areas for ferrite nucleation, the net effect will be a reduction of the ferrite nucleation rate [3,4,5,22].

Precipitation of large $Fe_{23}(C,B)_6$ on TiN and MnS inclusions at the inclusion/matrix interface has also been reported [15]. This emphasizes the importance of inclusion control to avoid the formation of large boron nitrides and borocarbides which are difficult to subsequently redissolve and hence are very detrimental to hardenability. Borocarbide precipitation kinetics follow the classical nucleation and growth theories developed to describe diffusion-controlled solid-state transformations [4,5,22]. Borocarbides are reported to precipitate from the

cooling austenite in the temperature range 1000°C to about 600°C depending upon the carbon and boron contents of the steel [2,5,7,9,18,22]. The presence of carbide forming elements such as chromium, molybdenum and niobium seems to promote finer $M_{23}(C,B)_6$ precipitates and enhances the boron hardenability effect [18,21,22]. Borocarbide precipitation proceeds with the fastest kinetics in the temperature range 700-800°C [2,22].

When the steel is reaustenitized after cooling, the austenitizing temperature required for complete dissolution of the $M_{23}(C,B)_6$ depends on the boron and carbon contents. Larger volume fractions and/or sizes of $M_{23}(C,B)_6$ precipitates require higher austenitizing temperatures and/or longer austenitizing times [2,5,18]. Dissolution of borocarbides upon reheating is reported to start in the range 900-930°C [7,18] and complete dissolution is achieved for temperatures above 1000°C [3]. Too high an austenitizing temperature may cause a fade in the boron hardenability effect because the dissolved boron will combine with any free nitrogen to form BN [7,24] or will exceed the optimum range for hardenability [21].

When the steel is cooled from the austenitizing temperature, BN will precipitate faster than the $M_{23}(C,B)_6$ at the higher temperatures because of the high diffusivity and great affinity for one another of the boron and nitrogen atoms [7,9,14]. As the austenite reaches lower temperatures (near 900°C), it becomes increasingly difficult for the iron atoms to diffuse over the relatively large distances required for the growth of the BN precipitates. Precipitation of $M_{23}(C,B)_6$, on the other hand, requires iron and substitutional atoms to diffuse over smaller distances to accommodate the borocarbide structure. At the lower temperatures then, it is the $M_{23}(C,B)_6$ precipitation which will be favoured [7].

Other Boron Rich Phases

Other boron containing phases have been indentified in alloy steels. Fe_2B has been detected in high boron austenitic steels [2,5]. Evidence was found of boron dissolution in the carbides NbC and V_4C_3 to form Nb(B,C) and $V_4(B,C)_3$ [2,5]. Also, Mo_3B_2, Nb_3B_2 and V_3B_2 with some substitution by iron atoms have been identified in steels. Coarse boron oxides (B_2O_3) and complex boron containing inclusions such as the borosilicate $FeO{\cdot}SiBO_2$ are reported to diminish available soluble boron in low nitrogen steels [4,5,18,22].

Because iron borocarbide ($Fe_{23}(C,B)_6$) is a more stable phase than iron borocementite ($Fe_3(C,B)$), $Fe_{23}(C,B)_6$ is the phase which forms during cooling in the range 950 to 600°C [5]. However, further transformation below 600°C will form borocementite as a metastable intermediate phase at the grain boundaries [5,22]. Boron is reported to replace carbon up to 80% in $Fe_3(C,B)$.

2.2 Boron Hardenability Mechanisms

Morral and Cameron [25] have reviewed the boron hardenability mechanisms proposed in the literature to date and have selected four mechanisms as being the most likely to occur in steels. All of these mechanisms assume that hardenability is influenced by the retardation of the ferrite nucleation. Since ferrite nucleates mainly on austenite grain boundaries, the mechanisms account for changes that might occur there during austenitization and transformation. Boron is reported to have little effect by itself on the ferrite growth rate [22]. However combined additions of Mo+B or Nb+B can slow down the parabolic growth rate of ferrite substantially. This indicates that the influence of the alloying elements on the ferrite growth rate is related to a reduction in carbon diffusivity, which is the rate controlling parameter for ferrite growth [22]. Boron does not change the M_S temperature [19,26].

2.2.1 Reduction in Austenite Grain Boundary Energy

The first mechanism suggested is that by segregating to the austenite grains boundaries, boron reduces their energy and makes them less favourable sites for ferrite nucleation.

2.2.2 Reduction in Diffusivity

In steels, it is usually assumed that the rate controlling parameter of ferrite nucleation is the carbon atom jump frequency. It is possible that boron reduces the diffusivity of carbon by blocking interstitial sites at the grain boundary or by increasing the modulus of the boundary [2]. This hypothesis has not yet been verified experimentally however.

2.2.3 Reduction in Number of Nucleation Sites

High angle austenite grains boundaries are composed of regions of relatively high and low atom density. The regions of low atom density are favoured sites for ferrite nucleation. By poisoning these sites either by filling the free volume, by segregating there [2] or by precipitating on the sites as borocarbides [4], boron may be reducing the ferrite nucleation density. If all the grain boundary sites are contaminated by boron atoms, the ferrite will have to nucleate elsewhere and at a much reduced rate.

2.2.4 Nucleation of Ferrite on Borocarbides

The precipitation of boron nitrides and/or borocarbides reduces the concentration of boron at the austenite grain boundaries and diminishes the hardenability effect. According to the site competition mechanism described above, the borocarbides at the grain boundaries will block ferrite nucleation if they are small enough. The interfaces of sufficiently large borocarbides will act as ferrite nucleation sites.

It is not yet possible to determine which of these mechanisms is the most valid because the methods used to detect boron in steels (autoradiography, SIMS, ion microprobe) do not have sufficient resolution to distinguish between atomic segregation and small precipitates at the grain boundaries [4,22].

2.3 Factors Controlling Effective Boron Content

In order to achieve the full potential of boron to enhance hardenability, it is necessary to prevent the formation of boron oxides and boron nitrides so that sufficient boron is left free to segregate to the austenite grain boundaries. Formation of B_2O_3 can be prevented by making the boron addition to aluminum killed steel and by using adequate ladle and casting practices to avoid reoxidisation of the melt [27,28].

Loss of effective boron due to formation of boron nitride can be prevented by the addition of strong nitride formers such as Al, Zr and Ti [4,5,19,27,29,30]. Kapadia and coworkers [5,31] have developped a formula to calculate the effective boron

content (B_{eff}) for hardenability from the total boron content (B_{total}) and the amount of nitride forming element added to the steel:

$$B_{eff} = B_{total} - [N - 0{,}002 - Ti/5 - Zr/15]$$

"N", "Ti" and "Zr" are the nitrogen, titanium and zirconium contents respectively. The 0,002 term represents the nitrogen content normally expected to be bound to Al, Si and V in low alloy steels [19].

Usually, only titanium is added to boron steels because it is three times more effective than zirconium in combining with nitrogen [27]. If $Ti < 5\ (N - 0{,}002)$, some boron will be lost as boron nitride. However, if the titanium addition exceeds the required amount, TiC may be formed with potential detrimental effects to the toughness [29,30]. Use of titanium as a denitrider may pose problems when factors such as stable production of large heats with variable nitrogen contents and variable boron and titanium yields are considered [30]. A solution to these problems is to use a less strong nitride former such as aluminum. Aluminum additions are used extensively in Europe and Japan to control effective boron [27,30]. Excessive additions of aluminum should be avoided as it will decrease hardenability, causing enlargement of the austenite grains and a deterioration of toughness [30]. Aluminum is reported to be more easy to contain in ranges effective for denitrization but harmless to toughness [30].

Upon air cooling aluminum treated steels from the austenitizing temperature, boron nitride will form before aluminum nitride because of the greater diffusivity of the boron atoms in the austenite [7,29]. This will cause a loss in hardenability effect. The hardenability can be restored by subsequent reaustenitizing at a high temperature (such as 1000°C) or for longer times in order to allow the steel to reach the equilibrium state of the Fe-Al-B-N system. Aluminum nitride will then nucleate and grow out of the existing boron nitride according to the reaction:

$$BN + [Al] \rightarrow AlN + [B]$$

leaving the boron atoms free to segregate to the austenite grains boundaries [7,10,24,29].

2.3.1 Optimum Boron Content for Hardenability

Some authors [4,18,22] define the optimum boron content for hardenability as varying from 10 to 30 ppm of acid soluble boron. Acid soluble boron is boron which is not combined as boron nitride or boron oxides. Other researchers [21,29] have determined optimum boron concentrations of 3 to 5 ppm. This content is the dissolved boron content in equilibrium with precipitated boron at the quenching temperature. Variations in optimum boron contents recommended in the literature may be due to the different austenite grains size and alloying additions of the materials investigated and also to the different techniques used to measure the boron concentration [5,27].

It is considered better to add a slight excess of boron to the recommended amount in order to ensure a reduced but more reproducible effect [5]. On the other hand, excessive boron levels may cause hot shortness and brittleness. If the boron content exceeds 30 ppm, coarse $F_{23}(C,B)_6$ may form which will drastically reduce the low temperature toughness [11].

The optimum content of solute boron depends on the amount of boron atoms required to segregate to the ferrite nucleation sites to inhibit ferrite nucleation. Because of the greater number of ferrite nucleation sites in controlled rolled steels compared to conventional quenched and tempered steels, more boron is required in controlled rolled steels. Proposed optimum boron content in solution in controlled rolled steels is around 10 ppm [11] compared to the 3-5 ppm required in quenched and tempered steels.

2.3.2 Effects of Carbon on Boron Hardenability

It is widely accepted that the boron hardenability effect is strongest in lower carbon steels. This can be explained by the fact that boron is mainly effective in suppressing proeutectoid ferrite nucleation. Its effect will then be highest when it is the austenite → ferrite transformation that controls hardenability and not the austenite → pearlite transformation as in the higher carbon steels [4,5,18,22].

The optimum boron content for hardenability does not seem to be related to the carbon content of the steel [5]. The boron hardenability effect decreases linearly

from a maximum at very low carbon contents to no effect at all for a carbon content of 0,9%. However, lineal analysis of data on boron containing steels with varying carbon contents has revealed that the variation in boron hardenability effect with steel composition cannot be explained by carbon content alone: other alloying elements also exert a strong influence (5)

2.3.3 Effects of Other Microalloying Elements on Boron Hardenability

In a C-Mn steel, the hardenability is increased with increasing additions of individual alloying elements such as carbon, nitrogen, molybdenum, manganese and silicon. The effectiveness of the alloying addition decreases in the order listed, on a weight percent basis. Small additions of niobium, vanadium and titanium also increase hardenability. The hardenability is decreased however if the microalloy addition exceeds the carbon-alloy solubility product as this will cause a loss of carbon and alloying element from solution due to precipitation of microalloy carbides (32). Some of the elements listed above show synergistic interactions in combination with other alloying elements, apart from their individual hardenability effects . Synergistic effects are reported between Mo and B (4,24), Cu and B (33,34), and Nb and B (4,11,33,34). Since HSLA steels are often microalloyed with Nb, the following section will provide more details on the effects of niobium in boron containing HSLA steels.

2.3.4 Niobium Containing Boron HSLA Steels

Effects of Niobium on Recrystallization of Austenite

The temperature at which complete recrystallization of austenite occurs during rolling of microalloyed steels increases with an increase in the level of microalloy in solution at the start of deformation. The magnitude of this effect increases for the different microalloying elements in the order V < Ti < Nb (35). The mechanism by which microalloying retards recrystallization is not entirely understood. Both solute drag and strain induced precipitation have been proposed as controlling processes in niobium steels. Their relative importance particularly with respect to the nucleation and growth stages of recrystallization have not been clearly established (36, 37).

Suitably sized precipitates of niobium will retard secondary growth of recrystallized austenite grains at temperatures above the recrystallization temperature. At lower temperatures, the precipitates inhibit static recrystallization so that elongated "pancaked" austenite grains are obtained prior to final cooling. The large number of sites available for ferrite or bainite nucleation in "pancaked" austenite explains the fine grain size of the transformed product [38].

Effects of Niobium on Hardenability of HSLA Steels

Niobium in solution can shift the nose of the CCT curve to longer times and can lower the $\gamma \rightarrow \alpha$ transformation temperature by as much as 100°C thereby increasing the hardenability of steel significantly [39]. It is the niobium taken into solution at the austenitizing temperature that depresses Ar_3. At slow cooling rates, the increase in hardenability will be relatively small because of solute depletion due to precipitation in the austenite. At faster cooling rates, virtually all the niobium taken into solution at the austenitizing temperature is retained and is effective in delaying the $\gamma \rightarrow \alpha$ transformation [40].

Subsequent precipitation hardening of the transformation product may be obtained by cooling or by tempering [40]. Solubility of niobium in ferrite is much less than in austenite so that fine precipitation of NbC can be obtained, giving added strength to the material [39].

Niobium in Boron Steels

In a study [11] on low carbon (0,032%C) boron HSLA steels it was found that the addition of boron to the base composition decreased the transformation temperature by about 40°C. Addition of niobium to the base material lowered the transformation temperature by 20°C and also refined the austenite structure considerably. However, the combined addition of boron and niobium resulted in a 150°C decrease in transformation temperature with a corresponding increase in strength and excellent toughness.

When boron steel is controlled rolled, borocarbide is continuously precipitated at the elongated austenite grains boundaries. This causes a depletion of segregated

boron at the grain boundaries. The $Fe_{23}(C,B)_6$ precipitates may also act as nucleation sites for ferrite formation resulting in a decreased boron hardenability effect [11]. However, in niobium-boron steel, precipitation of $Fe_{23}(C,B)_6$ is not observed and boron is homogeneously segregated to the ferrite nucleation sites [11]. In a very low carbon steel (< 0,05%C), the strain induced precipitation of NbC during rolling eliminates the carbon which is required for formation of $Fe_{23}(C,B)_6$. The synergistic effect of niobium and boron on hardenability is smaller in steels with higher carbon contents [41]. Niobium also contributes to the suppression of the precipitation of $Fe_{23}(C,B)_6$ by retarding the recrystallization of austenite during rolling. Boron atoms are trapped at lattice defects introduced by rolling in the unrecrystallization regime. By slowing down diffusion of carbon in austenite, solute niobium will also diminish the precipitation of $Fe_{23}(C,B)_6$ [11,12].

In order to obtain the synergistic effect of niobium and boron on the hardenability, the niobium content must be sufficiently large so that enough NbC will be precipitated during rolling to prevent the formation of $Fe_{23}(C,B)_6$. At the same time, sufficient niobium must remain dissolved in the austenite before the $\gamma \rightarrow \alpha$ transformation to ensure an adequate hardenability effect [12]. The optimum amount of niobium to be added depends on the chemical composition of the steel and on the processing variables.

Precipitation Kinetics of Niobium Phases

In boron steels, titanium is often added to protect boron from free nitrogen. Niobium precipitates in boron steels will therefore not be pure NbC, but mixtures of Ti, Nb, C and N. Because Ti(C,N) and Nb(C,N) have very high melting points, the volume diffusion rate of titanium and niobium is very slow inside the carbonitride precipitates, even in the austenite temperature range. Precipitates possess steep concentration gradients except for the very small nuclei (< 20 nm in diameter) [42].

The sequence in which the different carbonitrides are precipitated is determined by their solubility products. Upon cooling from the melt, TiN is usually formed first in the liquid steel. At high temperatures, TiN continues to precipitate from the austenite. As the temperature is further decreased, TiN is gradually replaced by

NbN, NbC and TiC, depending on the relative Ti, Nb, C and N contents of the material. If the titanium content is sufficiently large, TiC will precipitate before the niobium carbonitrides. The resulting precipitate distribution in a low niobium steel will include large inclusions of TiN, precipitates nucleated early (being composed of TiN coated with TiC and NbC) and smaller TiC precipitates coated with NbC, which were nucleated later during cooling of the austenite (fig. 2.1). In a higher niobium steel, large TiN precipitates will be coated by NbC and a small layer of TiC. Small precipitates nucleated later will be composed mainly of NbC with a very thin layer of TiC (fig. 2.1). Very small nuclei may be pure TiC or NbC, depending on the relative titanium and niobium contents [42].

Growth of TiN, TiC, NbC precipitates one upon the other is epitaxial in nature [43]. Microdiffraction patterns taken from precipitates containing titanium and niobium show no crystallographic changes within a given precipitate. Each precipitate is monocrystalline, with lattice parameters intermediate between those of its constituents (TiC, TiN, NbC, NbN) depending on their relative concentration [42].

2.4 Effects of Boron on Steel Properties

2.4.1 Applications of Boron Microalloyed Steels

One of the first categories of steels to which boron additions have been made are medium carbon (0,1 to 0,4%C) quenched and tempered steels used in the manufacturing of fasteners and bolts [19,27]. In these steels boron is used to impart adequate hardenability even with a reduced Cr and Mo content. Advantages of using boron addition in these steels include low hardness in the as-rolled condition (greater ease of machining and forming), the possibility of direct hardening from the forging temperature and good toughness, weldability and tempering resistance in a less costly material [19]. Boron steels also have better extrudability, machinability and show less quench cracking than boron-free steels with comparable hardenability [5].

A more recent but increasingly important aspect of the use of boron in steels is for the making of low carbon, low alloy, high strength steels (HSLA steels) [2,8,27,23]. In HSLA steels the full potential of the boron addition is achieved

because of the low carbon contents. These low carbon steels have acicular ferrite or martensite microstructures and show improved strength, toughness and weldability [2,27,33,44]. Recently, ultra low carbon bainitic steels have been developed which possess excellent mechanical properties and very good weldability due to the ultra low carbon levels and boron additions [45,46].

Boron is also used to improve the hot workability and creep resistance of stainless steels. Boron segregated to the grain boundaries seems to inhibit grain boundary cavitation during creep [6]. However, an excessive addition of boron to these materials may promote hot shortness [2].

It has been reported [47] that the addition of 0,005 to 0,010%B to steels produced by continuous slab casting diminished the occurrence of transverse cracking. The proposed explanation was that boron atoms slow down grain boundary self diffusion by pinning the vacancies.

2.4.2 Effects of Boron on Impact Toughness

Precipitation of coarse $M_{23}(C,B)_6$ due to excessive boron addition (> 30 ppm) or to inadequate heat treatment (such as isothermal holding at 700°C) is clearly detrimental to toughness [8,18]. Upper shelf energy is decreased for boron contents exceeding 30 ppm and the transition temperature is increased [48]. If the $M_{23}(C,B)_6$ precipitates are located inside the austenite grains, the fracture surface will have a cleavage morphology [8] but grain boundary borocarbides and boron nitrides may cause intergranular fracture [4,18]. However, when the boron addition is well controlled, 100% martensite or acicular ferrite microstructures are achieved. When these steels are tempered, their inherent toughness out weighs the embrittling effect of borocarbides [18,48].

2.4.3 Effects of Boron on Weldability

Amongst the different methods proposed for improving heat affected zone (HAZ) toughness under high heat input welding conditions, one of the most effective

ways is to reduce the base metal Ceq * by adding boron instead of carbon and other alloying elements to obtain the desired hardenability. Acicular ferrite or martensite microstructures with fine grains are obtained in the HAZ, giving improved toughness [8,49,50,51]. An improvement in Charpy transition temperature of HAZ of 20°C due to boron addition is reported [50].

Another approach is to use boron and titanium additions to reduce the free nitrogen content in the HAZ by forming nitrides [14,49,50]. Boron nitride precipitates also act as nucleation sites for ferrite, ensuring a fine uniform grain size in the HAZ [14]. Titanium and boron containing welding electrodes have been designed and are reported to promote more homogeneous weld metal structures with better low temperature properties [52,53].

* $Ceq = C + \frac{Mn}{6} + \frac{Ni+Cu}{15} + \frac{Cr+Mo+V}{5}$

Solubility product	Temperature (°C) 920	1200	1250	1300
$K_{AlN} = [Al][N]$	$5,6 \times 10^{-5}$	$8,4 \times 10^{-4}$	$1,2 \times 10^{-3}$	8×10^{-3}
$K_{BN} = [B][N]$	$3,4 \times 10^{-7}$	$5,7 \times 10^{-5}$	$1,2 \times 10^{-4}$	$2,3 \times 10^{-3}$
$K_{TiN} = [Ti][N]$	-	$4,2 \times 10^{-7}$	-	$1,9 \times 10^{-6}$

Table 2.1: Solubility Products for AlN, BN and TiN [29].

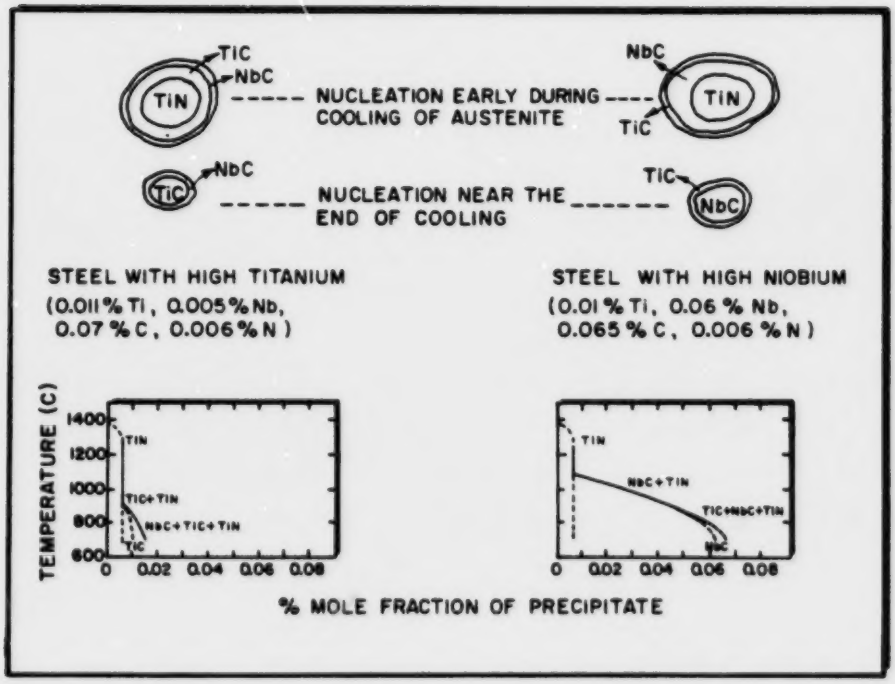

Fig. 2.1: Precipitation sequences in Ti-Nb steels [42].

CHAPTER THREE

EXPERIMENTAL PROCEDURE

3.1 Composition and Processing of Experimental HSLA Steels

3.1.1 Composition

Compositions of the experimental steels used for this study are given in Table 3.1. The carbon content was varied from 0,019% to 0,066% in order to study the influence of ultra low carbon levels on the boron hardenability effect. Manganese contents around 1,55 to 1,85% had to be used to ensure the steels had sufficient hardenability. Niobium (0,04 to 0,045%) was added to increase hardenability, to help control the austenite grain size and for moderate precipitation strengthening. Titanium and aluminum additions were made to protect the boron from free nitrogen. The nitrogen content was varied from 30 to 102 ppm to determine the maximum level of nitrogen that could be allowed while retaining sufficient boron hardenability. The effective boron content as calculated from the total boron, nitrogen and titanium contents is given for each experimental composition in Table 3.1. Other residuals (Si,S,P,O) were kept as low as possible in view of the laboratory melting and casting facilities which were used for preparing the materials. Alloying additions of molybdenum, copper, nickel and chromium were

made to some heats to establish the strength and hardenability increments to be expected from these alloying elements in ultra low carbon boron HSLA steels.

3.1.2 Processing

The experimental steels were cast and processed at the Material Technology Laboratories (CANMET, Department of Energy, Mines and Resources). Electrolytic iron was used as melting stock for the steels containing 0,02%C (alloys 0, 1 and 5). For the higher carbon steels (alloys 2, 6, 7, 8 and 9), the melting stock was Sidbec-Dosco iron to which a small amount of electrolytic iron was added to reduce the carbon content. All material was air melted and sand cast as 50 kg ingots with a section of approximately 12,7 cm x 15,2 cm.

Ingots were maintained at a temperature of 1100°C for two hours prior to rolling. This austenitizing temperature was chosen to avoid excessive growth of the austenite grains due to dissolution of boundary pinning microalloy carbonitrides at higher temperatures. Alloys 1A, 2A and 5A were rolled according to schedule #1 (Table 3.2). When ingot 7A was processed according to this schedule, the rolling mill was overloaded on pass no. 10. The rolling schedule was therefore revised to reduce the rolling loads. All the other experimental steels (0, 1B, 2B, 5B, 6A, 6B, 7A, 7B) were processed using this modified schedule (schedule # 2, table 3.2). For all experimental steels, the mill entry thickness was 12,7 cm and the final thickness was 13 mm .

Table 3.3 shows the schedules which were used for plate cooling. For most alloy compositions, plates were air cooled with a cooling rate of approximately 1,2°Cs^{-1} for 13 mm plate (alloys 0, 1A, 1C, 2A, 5A, 6A, 7A). For some alloy compositions, (1B, 2B, 5B, 6B, 7B) plates were immersed in an oil-water bath immediately after rolling producing an accelerated cooling rate of approximately 8°Cs^{-1}. These plates were removed from the bath at 550°C and were air cooled. This cooling schedule is aimed to simulate the On-Line Accelerated Cooling (OLAC) procedure used to produce steels for line pipe applications.

3.1.3 Simulation of Dilatometry Schedule on the Rolling Mill

To simulate the results of dilatometry testing on actual rolling practice, a coupon of as-rolled plate of steel 1A with an initial thickness of 13 mm was austenitized at 1100°C for 20 minutes. It was given a 25% reduction at 850°C and another 25% reduction at 815°C so that a final thickness of 8 mm was achieved. The coupon was air cooled after rolling.

3.2 Deformation Dilatometry

Deformation dilatometry was used to study the effects of processing, in particular the amount of reduction, the deformation temperature and the cooling rate on the transformation kinetics and final microstructure of the experimental steels. Deformation dilatometry experiments were carried out at the CANMET using a MMC deformation dilatometer. Cylindrical (4 mm diameter by 8 mm length) specimens were machined from the as-rolled plates in the transverse direction and or from as-cast material. The temperature vs time and dilatation vs time curves were recorded and used to construct Continuous Cooling Transformation (CCT) diagrams [54,55] at cooling rates between 100 and 0,3°C/s. Plots of fraction transformed vs temperature were also calculated using the technique described by Fisher and Geils [56] (fig. 3.1a). Deformation and cooling schedules used in the dilatometry experiments are given in Table 3.4, 3.5 and 3.6.

Because of friction between the ends of the dilatometry specimen and the platens, the distribution of strain along the length of the specimen is not homogeneous, resulting in a "barrelled" shape (fig. 3.1b). There is a corresponding variation in transformation behaviour. Therefore the microstructure and hardness of deformed dilatometry specimens were evaluated in the center of the specimens, where the deformation is highest.

3.3 Microstructural Characterization

3.3.1 Optical Microscopy

Samples were prepared for metallographic observations using conventional polishing techniques. Grinding was carried out on SiC papers (320 to 600 grit)

followed by polishing using 6 μm and 1 μm diamond paste on nylon cloth. The mounted samples were fine polished on Metron cloth (Buehler Co.) using an aqueous suspension of 0,3 μm α-alumina followed by 0,05 μm γ-alumina. Polished specimens were etched in 2% Nital (2 ml nitric acid in 98 ml ethanol) to reveal the general microstructural features. To reveal the prior austenite grains boundaries, specimens were etched in boiling saturated aqueous picric acid and ligthly repolished [57,58]. Etched specimens were examined using an Olympus optical microscope.

3.3.2 Scanning Electron Microscopy

For examination in the SEM, specimens etched with 2% Nital were coated with a layer of gold-palladium to enhance the electrical conductivity of the specimen surface. The cleaned fracture surfaces were also coated with Au-Pd prior to fractographic examination in a JEOL Type 25 S III scanning electron microscope operating at 25 KV. Analysis of inclusions was carried out using a Tracor Northern Series II X-Ray Analysis System attached to the SEM.

In order to relate the fractographic characteristics to the microstructure, an oblique sectioning technique was used. In this technique, the broken specimen is cut at an angle to the fracture surface and is mounted in lucite with the cut surface exposed. Normal polishing and 2% Nital etching are carried out, the lucite is removed and the specimen surface is cleaned and covered with gold-palladium. With this technique, it is possible to observe in the SEM both the microstructure and the fracture surface simultaneously (fig. 3.2).

3.3.3. Transmission Electron Microscopy

Thin foils were prepared by cutting 0,5 to 1 mm thick slices of material using an Isomet low speed saw. These slices were wet ground on SiC paper (240 to 600 grit) to reduce their thickness to 0,1-0,2 mm. Further thinning was carried out in a chemical bath composed of 80 ml H_2O_2, 14 ml H_2O and 6 ml HF. After thinning specimens were rinsed successively in H_2O_2, H_2O and ethanol. Disks with a diameter of 3 mm were then punched out from the 0,05 mm thick slices. Final polishing of the disks was done on a jet thinning apparatus (South Bay Technology) using an electrolyte composed of 100 g Na_2CrO_4 in 500 ml glacial

acetic acid and 30 ml distilled water at 20°C. Electropolishing was carried out with a current density of approximately 0,5A cm^{-2} until perforation of the specimen occured.

To prepare extraction replicas, polished specimens were etched in 2 to 5% Nital and coated with a layer of evaporated carbon (200-800 Å thick). The carbon films were stripped off by immersing the samples in a solution of 10% Br in ethanol. The replicas were cleaned in a solution of 50 ml ethanol, 50 ml acetone and 1 ml formic acid. After rinsing in 1:1 ethanol and acetone, they were placed on 200 mesh folding copper grids and dried.

Thin foils and extraction replicas were examined in a Philips EM 420 transmission electron microscope operating at 100 and 120 kV acceleration voltages. Selected Area Diffraction (SAD) and microprobe were used to obtain electron diffraction patterns of precipitates for identification (see Appendix A).

3.3.4 Determination of Volume Fraction of Microconstituents

The volume fraction of martensite-austenite (MA) microconstituents was evaluated by Manual Point Counting as per ASTM Standard E 562-83 (60). Transverse sections of specimens were polished, etched in 2% Nital and observed in the scanning electron microscope. An acceleration voltage of 15 kV was used and the magnification was selected so that the MA islands apeared as about one half the spacing between grid points. An array of points formed by a grid containing ten by ten lines spaced one centimeter apart was superimposed on the magnified image of the specimen. The number of points falling within the MA phase was recorded. The values were averaged over 30 fields uniformly distributed over the specimen surface. The following values were calculated from the raw data as per ASTM E 562-83:

1. Estimated volume fraction of MA microconstituent:

$$V.F._{MA} = \frac{1}{n} \sum_{i=1}^{n} \frac{P_i}{P_t}$$

where "n" is the number of fields observed (n =30)
"P_i" the number of grid points falling on MA phase
"P_t" the number of grid points (P_t=100)

2. Standard deviation estimate:

$$\hat{S} = \frac{1}{(n-1)} \sum_{i=1}^{n} \left(\frac{P_i}{P_T} - V.F._{MA}\right)$$

3. 95% confidence interval for volume fraction of MA:

$$C.I. = \frac{2\hat{S}}{\sqrt{n}}$$

4. Percentage error (statistical precision):

$$\% \text{ error} = \frac{C.I.}{V.F._{MA}} \times 100$$

A statistical precision of about 10% was aimed for and was obtained for most specimens when 3000 grid points were counted.

3.4 Determination of Mechanical Properties

3.4.1 Tensile Properties

For tensile testing of the 13 mm thick plates, small size round specimens proportional to the ASTM standard were used (fig. 3.3). Rectangular tensile test specimens were used for testing the 8 mm thick plate (fig. 3.4) of steel 1A.

Tensile tests were carried out at room temperature as per ASTM Standard E8-82 (59) with an Instron model TTD testing machine for the round specimens and a MTS series 810 testing machine for the rectangular specimens. A strain rate of 1,27 mm min^{-1} was used for all tests. A 2,54 cm extensometer was fastened directly on to the specimens to provide better measurements of the first stage of the load vs elongation curve. Percent elongation was determined from marks on the specimen surface (a 2,54 cm gage length was used) and reduction of area was calculated from gage diameter measurements taken before and after testing.

3.4.2 Impact Properties

Instrumented Charpy impact tests were carried out as per ASTM Standard E 23-81 [59] using a Satec Systems Inc. Model SI-IK3 impact machine equipped with a Dynatup Model ETI-630 data acquisition and analysis system (Effects Technology Inc.). Maximum potential energies of 406,7 J (300 ft-lbf) and 169,4 J (125 ft-lbf) were used, depending on specimen toughness. Standard (10 mm x 10 mm x 55 mm) V-notched specimens were machined from the 13 mm thick plates. Half-size (5 mm x 10 mm x 55 mm) specimens were used for the 8 mm thick plate (fig. 3.5). Specimens were machined with their long axis parallel to the rolling direction (longitudinal specimens) and others with their long axis perpendicular to the rolling direction (transverse specimens) to establish the effect of rolling texture on toughness.

The load-time and energy-time traces obtained from the instrumented impact test were analysed to obtain the following important parameters: initiation energy (E_i), propagation energy (E_p), total absorbed energy (E_t), general yield load (P_{gy}), maximum load (P_M) and the fracture load (P_F) (fig. 3.6).

3.4.3 Dynamic Fracture Toughness

To obtain approximate values of the dynamic fracture toughness of the experimental steels, precracked Charpy V-notch specimens were broken at room temperature, -40°C and -100°C. The fracture toughness was calculated using the instrumented Charpy data and a special analysis program available on the Dynatup Model ETI-630 data acquisition and analysis system. A complete discussion of the derivation of the formulas used for the fracture toughness calculations is given in reference [70]. The test specimens used were standard Charpy specimens machined in the longitudinal direction from as-rolled plate with a 2 mm V-notch in the through-thickness direction. A fatigue precrack was grown from this starter notch as per ASTM Standard E 812-81 [59] using a Manslab Fatigue Precrack Machine (Model FCM-300). The fatigue precrack was grown under a maximum

load (bending moment) of about 110 N·m (1000 in·lb). Growth of the crack was monitored so that

$$0{,}45 \leq \frac{a}{w} \leq 0{,}55$$

where "a" is the crack depth and "w" is the specimen width. The crack depth was calculated after fracture using the formula:

$$a = \frac{1}{4}\left[\frac{(a_1 + a_5)}{2} + a_2 + a_3 + a_4\right] \qquad \text{(fig. 3.7)}$$

For each test, the program calculates the specimen compliance (C_s):

$$C_s = \frac{72}{E\,B}\, f\left(\frac{a}{w}\right) + \frac{20}{E\,B}$$

where "E" is Young's modulus
"B" is the specimen thickness

$$f\left(\frac{a}{w}\right) = 1{,}8626\,(a/w)^2 - 3{,}95(a/w)^3 + 16{,}3777\,(a/w)^4 - 37{,}2277\,(a/w)^5 + 77{,}554\,(a/w)^6 - 126{,}8727\,(a/w)^7 + 172{,}5325\,(a/w)^8 - 143{,}964\,(a/w)^9 + 66{,}564\,(a/w)^{10}$$

The machine compliance (C_M) is then calculated as:

$$C_M = \frac{D_{GY}}{P_{GY}} - C_s$$

where D_{GY} is the deflection at general yield
P_{GY} is the load at general yield

The J-integral (J_d) is defined as

$$J_d = \frac{2\,E_I'}{B\,(w - a)}$$

where $$E_I' = E_M - \frac{P_M^2\,C_M}{2}$$

E_M is the energy at maximum load
P_M is the maximum load.

The equivalent energy fracture toughness (K_d^*) is given by:

$$K_d^* = \frac{1.5\ Y\ L}{B\ w^2} \cdot P_i^* \cdot a^{1/2} \qquad (MPa \cdot m^{1/2})$$

where $$P_i^* = \sqrt{\frac{2E_I}{C_s}}$$

"Y" = 1,93 - 3,07 (a/w) + 14,53 $(a/w)^2$ - 25,11 $(a/w)^3$ + 25,8 $(a/w)^4$

"L" is the support span length.

The J-integral and other values derived from it are valid only for $0,45 \leq a/w \leq 0,55$.

3.4.4 Hardness Measurements

Vickers Diamond Pyramid Hardness measurements were performed on a Leco Model V-100A Vickers Hardness tester using a 10 kg load applied for 10 seconds. Testing was conducted as per ASTM Standard E92-82 [59] on flat surfaces ground to a finish as least as good as 600 grit SiC paper. The instrument specified measuring accuracy is 0,5%.

3.5 Determination of Boron Distribution

To map the distribution of boron in the steels, high resolution autoradiography was carried out at the Research and Development Laboratories of Nippon Steel Co. (Kawasaki, Japan). In this technique [61,62], carefully polished specimens are covered with a solid detector (usually cellulose acetate film) and baked at 140°C for several hours to ensure excellent contact of the film to the specimen surface. The specimen is then exposed in a reactor to a thermal neutron flux of 1 to 4 x 10^{14} neutron cm^{-2}. Under irradiation, the isotope ^{10}B (which is present as about 19,8 at. % in natural boron) undergoes the reaction

$$^{10}B + n \rightarrow {}^4\alpha + {}^7Li$$

The fission products escape into the film causing irradiation damage along their path into the detector. The cellulose acetate film is then removed from the specimen and etched in a strong alkaline solution. The irradiation damage tracks in the detector are etched into etching pits and the pattern and density of these etch pits reveal the distribution of boron atoms in the surface layer of the specimen.

This technique is reported to have a resolution of 1 to 2 μm and a sensitivity of about 1 ppm boron [63]. The practical limit of boron detection is expected to arise from the contribution of the ^{17}O fission reaction under high neutron exposures:

$$^{17}O + n \rightarrow {}^{4}\alpha + {}^{14}C$$

Alloy No.	Heat No.	Chemical Composition (Wt %) C	Mn	Si	S	Nb	Ti	Al	Btot (ppm)	Beff (ppm)	N(ppm)	Cu	Mo	Ni	Cr	P	O (ppm)
0	2007	0.020	1.65	0.31	0.006	0.045	0.020	0.025	-	-	59	-	-	-	-	0.005	28
1 A	1811	0.019	1.85	0.41	0.0063	0.04	0.02	0.02	16	16	32	0.01	-	0.01	-	0.008	~ 80
1 B	1932D	0.015-0.018	1.75-1.80	0.25	0.0059-0.0062	0.04	0.02	0.02	15	1	65	-	-	-	-	-	-
1 C	1872	0.022	1.81	0.4	0.0056	0.05	0.03	0.025	12	< 0	102	-	-	-	-	-	-
2 A	1839	0.028	1.71	0.305	0.0066	0.04	0.03	0.03	15	15	33	0.01	-	0.01	-	0.005	22-42
2 B	1931D	0.04-0.043	1.70	0.28	0.0062-0.0065	0.04	0.02	0.03	15	15	50	-	-	-	-	-	-
5 A	1812	0.018	1.78	0.36	0.0064	0.04	0.03	0.02	37	37	34	0.01	0.001	0.01	-	0.007	~ 60
5 B	1876C	0.023	1.57-1.61	0.29	0.0062	0.04	0.02	0.025	32	13	79	-	-	-	-	-	-
6 A	1871C	0.031-	1.69-	0.275	0.0054-0.0064	0.045	0.02	0.02	20-24	20	50	0.305	0.195	-	-	-	-
6 B	1871B	0.047	1.72														
7 A	1771	0.066	1.68	0.31	0.006	0.04	0.021	0.05	23	17	68	0.36	-	0.19	-	0.006	33
7 B	1892D	0.060	1.54-1.57	0.275	0.01	0.045	0.02	0.025	10	10	50	0.375	-	0.205	-	-	-

Table 3.1: Chemical Composition of Experimental HSLA Steels.

Rolling Schedule # 1

Pass No.	Mill Setting (inches)	(cm)	Temperature (°C)
roughing			
1	4.550	11.56	1100
2	4.120	10.46	1060
3	3.720	9.45	1040
4	3.350	8.51	1020
5	3.010	7.65	1000
finishing			
6	2.690	6.83	900
7	2.400	6.10	885
8	2.110	5.36	870
9	1.830	4.65	855
10	1.560	3.96	840
11	1.310	3.33	825
12	1.080	2.74	815
13	0.870	2.21	800
14	0.665	1.69	785
15	0.500	1.27	770

Rolling Schedule # 2 (revised schedule)

Pass No.	Mill Setting (Inches)	(cm)	Temperature (°C)
roughing			
1	4.550	11.56	1100
2	4.120	10.46	1060
3	3.720	9.45	1040
4	3.350	8.51	1020
5	3.010	7.65	1000
finishing			
6	2.720	6.91	900
7	2.450	6.22	890
8	2.190	5.56	875
9	1.940	4.93	865
10	1.700	4.32	850
11	1.470	3.73	840
12	1.250	3.18	825
13	1.040	2.64	815
14	0.840	2.13	800
15	0.650	1.65	785
16	0.500	1.27	770

Table 3.2: Rolling Schedules Used for Experimental HSLA Steels.

Alloy No.	Heat No.	Cooling Start Temperature (°C)	Cooling Finish Temperature (°C)	Average Cooling Rate (°Cs -1)
0	2007	760	-	Air cool 1,2
1 A	1811	760	-	Air cool 1,2
1 B	1932D	760	550	OLAC ~ 8
1 C	1872	760	-	Air Cool 1,2
2 A	1839	760	-	Air cool 1,2
2 B	1931D	760	550	OLAC ~ 8
5 A	1812	760	-	Air cool 1,2
5 B	1876C	760	550	OLAC ~ 8
6 A	1871C	760	-	Air cool 1,2
6 B	1871B	760	550	OLAC ~ 8
7 A	1771	760	-	Air cool 1,2
7 B	1892D	760	550	OLAC ~ 8

Table 3.3: Plate Cooling Schedules.

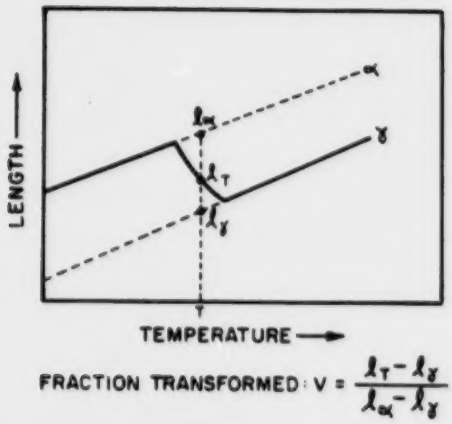

Fig. 3.1a) Schematic of a length-temperature curve obtained from a dilatometer illustrating calculation of the fraction transformed (56).

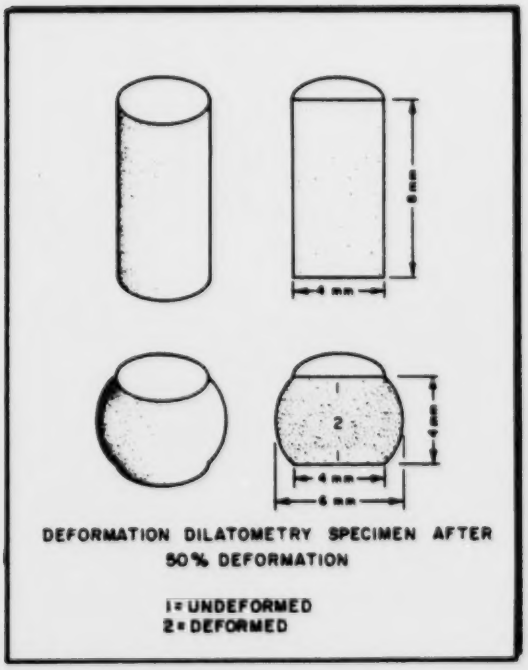

Fig. 3.1b) Diagram illustrating the non-homogeneous deformation of dilatometry specimen.

Specimens were processed according to the following schedule:

Heat to 1100°C in 2 min
Hold 15 min at 1100°C
Cool in about 5 s to 825°C
Deform to 50% original length at 825°C
Hold 10 s at 825°C
Cool with the following cooling rates:

Specimen No.	Alloy No.	Heat No.	T (800-500°C) cooling rate
1-3	1 A	1811	3
1-10	1 A	1811	16.2
1-30	1 A	1811	29.25
1-100	1 A	1811	97.5
1-300	1 A	1811	293
1-1000	1 A	1811	973
5-3	5 A	1812	3
5-10	5 A	1812	16.2
5-30	5 A	1812	29.25
5-100	5 A	1812	97.5
5-300	5 A	1812	295
5-1000	5 A	1812	974
7-3	7 A	1771	1.5
7-10	7 A	1771	13.8
7-30	7 A	1771	29.5
7-100	7 A	1771	97
7-300	7 A	1771	292
7-1000	7 A	1771	973

Note: All the specimens were machined from as-rolled plates.

Table 3.4: Dilatometry Specimens Used to Construct the CCT Diagrams.

Specimen No.	Alloy No.	Heat No.	15 min at austenitizing temperature (°C)	Cooling time from austenitizing temperature to deformation temperature (s)	% First deformation	First deformation temperature (°C)	Holding time at first deformation temperature (s)	% Second deformation	Second deformation temperature (°C)	Holding time at second deformation temperature (s)	Cooling Rate t (800-500°C) (s)
1-300	1A	1811	1100	~ 5	50	825	10	-	-	-	300
1A	1A	1811	1100	~ 5	25	1050	15	25	825	10	300
1C	1A	1811	1100	~ 5	25	1050	15	25	1050	10	300
1D	1A	1811	1100	~ 5	25	1050	15	25	825	150	300
1G	1A	1811	1100	~ 5	25	825	15	25	825	10	300
1L	1A	1811	1175	~ 5	25	1050	15	25	825	10	300
1B-300	1B	1932	1100	~ 5	50	825	10	-	-	-	300

Note: All specimens were machined from as-rolled plates except specimen 1B-300. Specimen 1B-300 was machined from the as-cast ingot of alloy 1B.

Table 3.5: Dilatometer Trials to Investigate the Effects of Deformation Schedule on Transformation Kinetics.

Specimens were processed according to the following schedule:

Heat to 1100°C in 2 min
Hold 15 min at 1100°C
Cool in 5 s to 825°C
Deform to 50% of original length at 825°C
Hold 10 s at 825°C
Cool such that t (800 -500°C) = 300 s

Specimen No.	Alloy No.	Heat No.
0-300	0	2007
1-300	1 A	1811
1C-300	1 C	1872

Note: All specimens machined from as-rolled plate.

Table 3.6: Dilatometer Specimens to Evaluate the Influence of Boron and Nitrogen Contents on the Transformation Kinetics.

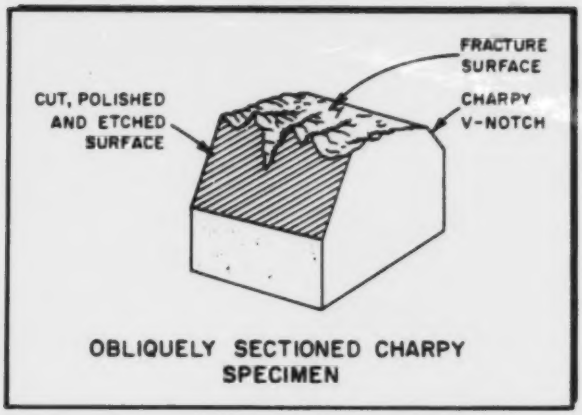

Fig. 3.2: Obliquely sectionned Charpy specimen.

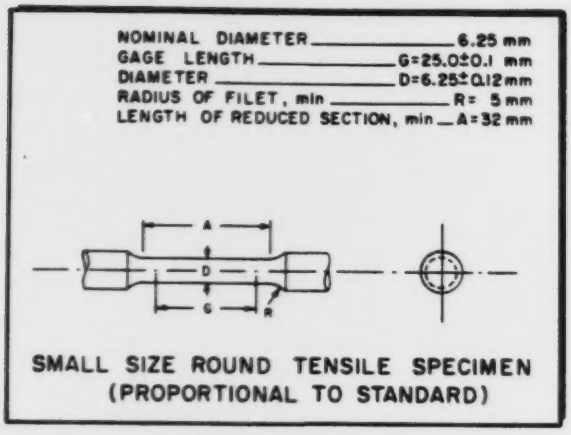

Fig. 3.3: Small size round tensile specimen used to test 13 mm thick plates.

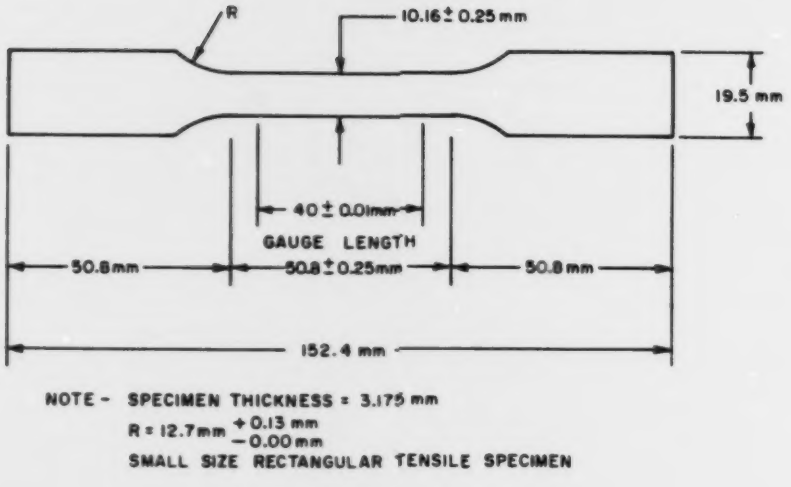

NOTE - SPECIMEN THICKNESS = 3.175 mm
R = 12.7mm $^{+0.13\ mm}_{-0.00\ mm}$
SMALL SIZE RECTANGULAR TENSILE SPECIMEN

Fig. 3.4: Rectangular tensile specimen used to test 8 mm thick plate.

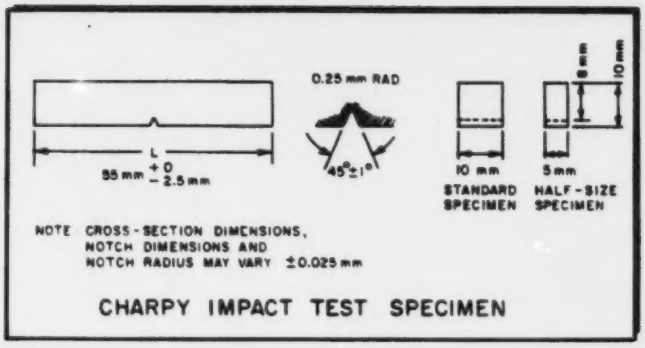

Fig. 3.5: Specimens used for Instrumented Charpy Impact Testing.

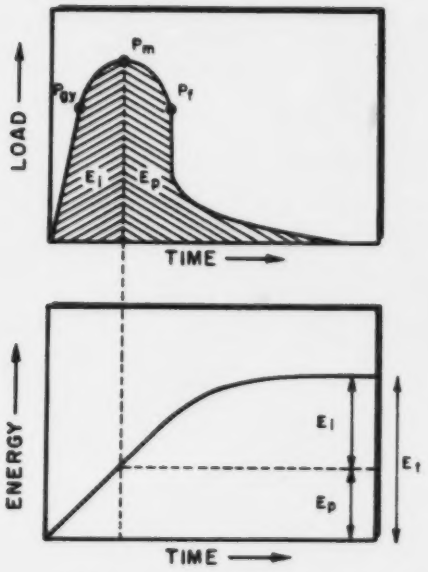

Fig. 3.6: Idealized Load-time and Energy-time traces from instrumented impact test.

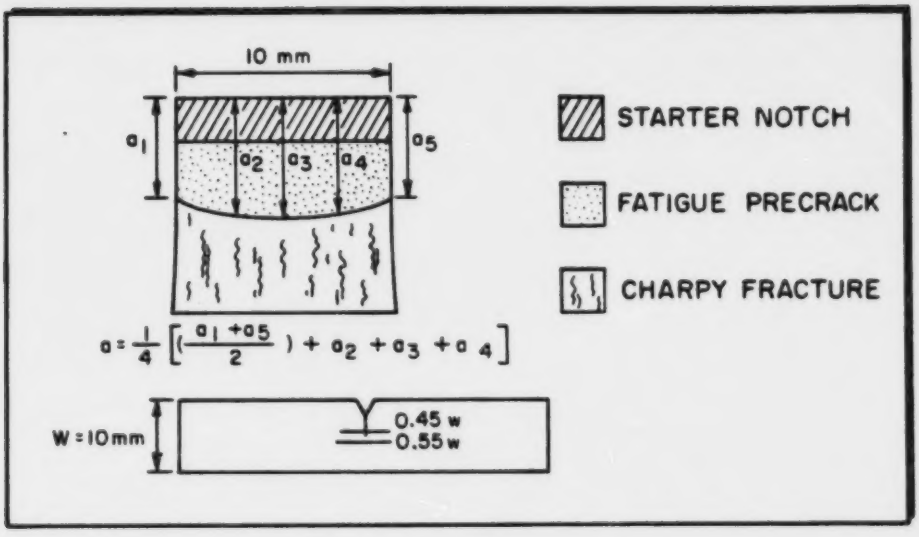

Fig. 3.7: Calculation of crack depth of precracked Charpy V-notch specimen.

CHAPTER FOUR

RESULTS AND DISCUSSION

4.1 As-rolled and Air Cooled Experimental Boron HSLA Steels

Composition of the as-rolled and air cooled experimental boron HSLA steels is given in Table 3.1 (Alloys 0, 1A, 2A, 5A and 7A). The rolling schedules and cooling procedures used to prepare the steels are listed in Tables 3.2 and 3.3.

4.1.1 Microstructure

The microstructure of alloy 1A in the as-rolled and air cooled state is composed of a mixture of fine polygonal ferrite grains and acicular ferrite. Small martensite-austenite (MA) islands are also found (fig. 4.1a). Acicular ferrite can be defined as a highly substructured non-equiaxed ferrite. It forms on continuous cooling by a mixed diffusion and shear mode of transformation. Transformation begins at a temperature slightly higher than the upper bainite transformation [64,65,66]. Acicular ferrite is distinguished from bainite by its low carbon content which results in only a small amount of carbide being present in the acicular ferrite microstructure. Also, the term bainite is used to describe such a wide range of structures that it is somewhat indefinite [64] so that acicular ferrite is preferred to describe this type of microstructure. Due to the low finish rolling temperature and heavy reductions used in rolling

alloy 1A, the austenite grains are very elongated and the final microstructure has a rather banded appearance (fig. 4.1a)
Microstructure of alloy 2A is composed of bands of fine grained ferrite and acicular ferrite interspersed with bands of larger grained ferrite (fig. 4.1b). The fine MA islands are found preferentially in the acicular ferrite regions (fig. 4.2a). Some bainite and degenerate pearlite islands are also present.

Alloy 5A has a very similar microstructure to that of alloy 1A (fig. 4.1c). In both steels, the MA microconstituents are formed preferentially along grain boundaries and sub boundaries (fig. 4.2b).

Alloy 7A has a microstructure composed of polygonal ferrite grains. The ferrite grain size follows a bimodal distribution with some very fine grains (< 5 μm) while the other grains are much larger (~ 20 μm) (fig. 4.1d). A small amount of acicular ferrite is also present as well as islands of high carbon constituent. This high carbon constituent is composed of MA, bainite and pearlite. The pearlite is often degenerated and formed in connection with MA islands (fig. 4.2c). The increased amount of high carbon constituent in Alloy 7A compared to alloys 1A, 2A and 5A is explained by the higher carbon content of Alloy 7A (see Table 3.1).

Thin foils of alloys 1A, 5A and 7A were examined in the transmission electron microscope. Micrographs of alloys 1A and 5A show the fine grained acicular ferrite with high dislocation density and small MA islands found in these steels (fig. 4.3a and 4.3b). In alloy 7A, the ferrite grains have a lower dislocation density and some precipitates can be seen (fig. 4.3c). Cementite lamellæ can be observed in a large degenerate pearlite island in alloy 7A (fig.4.3d). Figure 4.3e shows a higher magnification view of a MA island. The presence of fine twins in the martensite is an indication of alloy and carbon enrichment in MA martensite. It is well known that twins are found mainly in higher Ceq martensite [67].

Since all of the four alloys investigated are microalloyed with titanium and niobium, numerous titanium and niobium containing precipitates were found on the carbon extraction replicas prepared from the as-rolled and air cooled alloys (fig. 4.4a and 4.4b). Analysis of selected area diffraction (SAD)

patterns taken from these precipitates showed them to be TiN, TiC and NbC. However it is known [42,43] that titanium and niobium are mutually soluble in this type of precipitate. Because of the similar interplanar spacings of TiN, TiC and NbC (Table 4.1) it is difficult to distinguish by SAD between pure TiN, TiC or NbC precipitates containing both Ti and Nb. These mixed precipitates are monocrystalline with interplanar spacings intermediate between the pure precipitates, depending on the volume fraction of TiN, TiC and/or NbC in the precipitate.

Replicas were therefore examined in a Philips EM420 transmission electron microscope equipped with Energy Dispersive X-Ray Analysis. It was found that most precipitates larger in diameter than 20 nm contained both titanium and niobium in varying proportions. Rounded precipitates tended to be more Nb-rich and therefore had lattice parameters closer to those of NbC (fig.4.4b). Square precipitates were often titanium rich, especially the large square precipitates (fig. 4.4a). However, any quantitative analysis of these precipitates would have required a quantity of work outside the scope of this project in order to attain some statistical significance. No attempt was therefore made to study the variation in precipitate composition with precipitate size, morphology or with alloy composition (Ti, Nb, C, N) in these steels. It is noted that these precipitates were also identified on thin foils of the experimental boron steels (fig. 4.3c and 4.4c).

Microstructure of alloy 0 in the as-rolled and air cooled state is shown in fig.4.5a and 4.5b. Alloy 0 had a similar composition to that of alloys 1A and 5A (see Table 3.1) except that it contains no boron. Microstructure of alloy 0 was composed of fine polygonal ferrite with pearlite islands (fig. 4.5a). The volume fraction of pearlite was small because of the extra low carbon content of the steel but the pearlite lamellæ are not degenerated (fig.4.5b).

4.1.2 Boron Distribution in As-rolled and Air Cooled Steels

The boron distribution in alloys 1A, 2A, 5A and 7A in the as-rolled and air cooled state was determined using boron autoradiography. The results show that there is some segregation of boron in planes parallel to the rolling direction (fig. 4.6a, 4.6b, 4.6c. and 4.6d) but no definite segregation to the austenite grain boundaries can be observed (compare fig. 4.6a with 4.6e and fig. 4.6c with 4.6f). This is expected in heavily controlled rolled steels because in this case boron does not segregate to the austenite grain boundaries only but also to deformation induced defects such as deformation bands and twin boundaries located inside the austenite grains [11,12]. This segregation of boron to all types of ferrite nucleation sites gives an almost uniform appearance to the boron distribution. If a sufficient amount of boron is free to segregate however a very strong hardenability effect can be obtained in this manner [11,12]. It must be noted that in these low carbon steels, hardenability refers to the ability to suppress polygonal ferrite formation and obtain a microstructure composed of acicular ferrite (and not necessarily martensite)

In these experimental steels, boron is also present as rather large precipitates (fig.4.6). In the case of alloys 1A and 2A, the boron precipitates are arranged in stringers (fig.4.6a and 4.6b). Analysis by EDAX (in the SEM) of the inclusions present in these steels revealed them to be composed mainly of manganese, aluminum, titanium and sulfur in variable proportions (fig.4.7). Complex oxides such as galaxite ($MnO{\cdot}Al_2O_3$) which contain Al_2O_3 and MnO, and alsoTiN and MnS are known to form as primary inclusions in steels [68]. It has been reported that MnS and Al_2O_3 inclusions may act as nucleation sites for BN and $M_{23}(C,B)_6$ precipitation during controlled rolling [15] which would explain the boron distribution observed in these steels. With the amount of boron available for segregation to the ferrite nucleation sites being reduced by its precipitation on the inclusions, only partial effectiveness of the element can be expected. It is worthwhile mentionning that sulfur and nitrogen levels in alloys 1A, 2A, 5A and 7A are higher than those reported for controlled rolled HSLA steels where full effectiveness of boron was obtained [46].

4.1.3 Mechanical Properties of the As-rolled and Air Cooled Steels

Mechanical properties of the experimental boron steels in the as-rolled and air cooled state are listed in Table 4.2. Although the strength levels achieved in these steels are moderate, their toughness is excellent with transition temperatures (55 J criteria) less than -90°C for all five alloys.

The best combination of strength, ductility and toughness was achieved for alloy 5A, which contains the largest boron addition (0,0037%). Lower strength levels (in particular yield strength) were obtained for the higher carbon alloys 2A and 7A. These two alloys contained lesser amounts of acicular ferrite and more large grained polygonal ferrite than steels 1A and 5A. It can be concluded from these observations that a stronger boron effect was obtained in alloys 1A and 5A than in alloys 2A and 7A. The effect on hardenability was strongest in the alloy containing the highest boron addition (alloy 5A). Higher strength levels have been achieved by other investigators (11,12,44,45,46) using steel compositions very similar to those studied here. It can then be surmised that the full boron hardenability effect was not obtained in the experimental steels (at least not in the present state: as-rolled and air cooled). This may be explained by the fact that some of the boron was not free to segregate to the austenite boundaries and other ferrite nucleation sites because it was already precipitated on the inclusion stringers present in the alloys. As discussed earlier, the content of residual elements (S,N) in these steels is greater than those encountered in boron steels where full hardenability effect of boron was obtained. This would explain also why the best results were obtained with the alloy having the largest boron addition (alloy 5A).

Comparison of the strength achieved in alloy 1A (base composition + boron) with the strength of alloy O (base composition) indicates the extent to which boron has helped improve the mechanical properties. The strength increment is moderate (17 MPa for the yield strength and 27 MPa for the tensile strength) but a larger increase in strength could be attained in a steel with full boron effectiveness as indicated by the strength levels achieved in alloy 5A. Ductility of alloy O is high, due to its low carbon and alloying content and consequently it has very good toughness (fig.4.8a). However, the boron

additions bring about only a small deterioration in ductility and toughness over the base composition.
Macrofractographs of Charpy specimens of the experimental steels show that all fracture surfaces are essentially ductile (fig.4.8b). At lower test temperature, the number of splits increases and the amount of deformation decreases. The steels with higher carbon contents (alloys 2A and 7A) have slightly lower impact resistance. This may be due to their higher volume fraction of brittle, high carbon microconstituents (MA and degenerate pearlite). On the other hand, the impact energy of the alloys with the higher strength levels (alloys 1A and 5A) decreases more abruptly with temperature (fig.4.8a). This is due to the greater proportion of high dislocation density acicular ferrite in these alloys.

Fracture surfaces of charpy specimens broken at -100°C were composed mainly of dimples (fig.4.9a) with some quasi cleavage being present at the center of specimens of alloys 1A, 5A and 7A (fig.4.9b). Alloy 5A showed a greater proportion of quasi cleavage and more shallow splits, in accordance with its lower impact energy at -100°C. Of Charpy specimens of alloy 2A tear ridges were observed on the walls of the many splits present on the fracture surface (fig.4.10a and 4.10b). Formation of these splits seems to have required a large amount of deformation and energy as evidenced by the tearing observed. Large dimples at the root of the shallow splits (fig.4.10c) showed no evidence of inclusions.

Alloys 2A and 7A presented the greatest number of splits on their fracture surfaces (fig.4.8). These two alloys also had a greater amount of banding in their microstructure. Bands of smaller ferrite gains and high carbon microconstituent are alternated with bands of larger polygonal ferrite grains (fig.4.1b and 4.1d). This non homogeneity of the ferrite grain size and microstructure as well as the presence of inclusion stringers are responsible for the large number of splits found on the fracture surface of Charpy specimens of the experimental steels [79].

4.2. Influence of Cooling Rate on the Transformation Behaviour of the Experimental Boron Steels

To investigate the influence of the cooling rate on the transformation behaviour of the experimental boron steels, continuous cooling transformation (CCT) diagrams were constructed using deformation dilatometry data obtained for alloys 1A, 5A, and 7A. The deformation and cooling schedules used for the dilatometry testing are given in Table 3.4.

4.2.1 CCT Diagram and Typical Microstructures for Alloy 1A

The CCT diagram obtained for alloy 1A is shown on fig.4.11. This diagram shows that boron is effective in retarding the $\gamma \rightarrow \alpha$ transformation in alloy 1A even for cooling rates slower than air cooling (air cooling of 13 mm plate corresponds appproximately to t (800-500°C) = 300 s or about 1°C s^{-1}). Microstructure of dilatometry specimens 1-10 to 1-1000 is composed of acicular ferrite with islands of MA microconstituent (fig.4.12b, 4.12c and 4.12d). At the slower cooling rates (specimens 1-300 and 1-1000), some bainite and degenerate pearlite islands are also found (fig.4.13a and 4.13b). With the fastest cooling rate (specimen 1-3) a mixture of highly dislocated lath acicular ferrite and extra low carbon martensite with fine MA islands along the lath boundaries is obtained (fig. 4.12a, 4.13c and 4.13d).

As the cooling rate decreases, the volume fraction and size of the MA constituents increase (fig. 4.14). For the slowest cooling rate (specimen 1-1000), the volume fraction of MA is smaller because some MA islands have been replaced by other high carbon microconstituents such as bainite and degenerate pearlite islands. There is no strong correlation between the volume fraciton of MA and the hardness of dilatometry specimens. The hardness decreases with a decrease in the cooling rate but there is no further change in hardness for cooling rates slower than t (800-500°C) = 30 s. The higher hardness values measured for specimens 1-3 and 1-10 are related to the increased volume fraction of high dislocation density acicular ferrite and extra low carbon martensite present in these specimens. The cooling rate independence of the hardness for cooling rates greater than t (800-500°C) = 30 s is due to the persistence of the boron hardenability

effect even at these slow cooling rates so that acicular ferrite microstructures are obtained.

Boron autoradiography performed on specimen 1-30 showed that boron is segregated to the austenite grain boundaries (fig.4.21a and 4.21b). This is to be expected from the observed hardenability effect. It is not possible to distinguish on the autoradiograph whether boron is in solution at the grain boundaries or in the form of precipitates but it is clear that sufficient boron is there to bring about a full boron effect on the hardenability.

4.2.2 CCT Diagram and Typical Microstructures for Alloy 5A

The CCT diagram obtained for alloy 5A is shown on fig.4.15. The transformation kinetics and typical microstructures obtained for alloy 5A with cooling rates slower than t (800-500°C) = 300 s (specimens 5-300 and 5-1000) are very similar to those obtained for alloy 1A (specimens 1-300 and 1-1000). For both alloys, the AFs temperature is about 700°C and the microstructure is acicular ferrite interspersed with islands of MA microconstituent (fig.4.12c, 4.12d and 4.16c, 4.16d). This indicates that when boron is fully effective, the addition of 37 ppm of boron (as in alloy 5A) instead of 16ppm of boron (as in alloy 1A) has little additionnal effect on the transformation behaviour and resulting microstructures when cooling rates slower than 1°C s^{-1} (air cooling of a 13 mm thick plate) are used. At these slower cooling rates, other alloying elements such as Mn and Si do not have a very strong effect on hardenability.

For cooling rates faster than air cooling (specimens 1-3 to 1-100), alloy 1A has lower AFs temperatures than alloy 5A (compare fig. 4.11 and 4.15). Specimens 1-3 shows a martensitic transformation which was not observed for specimen 5-3. Microstructure of specimen 1-3 is a mixture of lath acicular ferrite and extra low carbon martensite (fig.4.12d and 4.13c) whereas the microstructure of specimen 5-3 is completely acicular ferritic with no martensite (fig.4.16d and 4.17a). The thin foil of specimen 5-3 shows a fine grained, highly dislocated acicular ferrite microstructure without laths (fig.4.17b).

This can be explained by the fact that at the faster cooling rates such as t (800-500°C) = 3s (which is 100°C s^{-1}), alloying elements such as Mn and Si have a stronger influence on hardenability. Since alloy 5A contains less Mn and Si than alloy 1A (see table 3.1), it has lower hardenability than alloy 1A when these quench rates are used.

Carbon replicas of dilatometry specimens of alloys 1A and 5A revealed the presence of numerous titanium and niobium containing precipitates. Identification of these precipitates by SAD showed them to be TiN, TiC and NbC (fig. 4.12c and 4.17d). Some replicas were examined in a Philips EM 420 transmission electron microscope equipped with Energy Dispersive X-Ray Analysis. It was found that very small (20nm) square precipitates were mostly Ti(C,N). Rounded precipitates 30 to 50 nm in diameter tended to be niobium rich but most of the larger precipitates contained both niobium and titanium in variable proportions. Qualitatively it appeared that the niobium content is higher in precipitates extracted from dilatometry specimens subjected to a slow cooling rate (such as specimen 5-1000). This can be explained by the longer time available for NbC precipitation when the specimen is cooled slowly. However no quantitative measurements were made to support these observations as the amount of work and time required to achieve statistical significance would have exceeded the scope of this study.

Boron autoradiography of specimen 5-30 shows a strong boron segregation to the austenite grain boundaries (fig. 4.21c and 4.21d). There is some evidence of boron precipitation on some boundaries. Because of their lack of stability and poor crystallinity, boron precipitates are difficult to identify on replicas and it has not been possible, with the techniques used in this study, to confirm the presence of boron precipitates in specimen 5-30.

4.2.3 CCT Diagram and Typical Microstructures of Alloy 7A

Alloy 7A has higher carbon and nitrogen contents than alloys 1A and 5A but it contains less manganese (Table 3.1). Because of its higher nitrogen content, some of the boron is not effective in alloy 7A as calculated using the formula $B_{eff} = B_{tot} - [N - 0{,}002 - Ti/5]$ [5,31]. All the boron was calculated to be effective for alloys 1A and 5A. However, B_{eff} = 17 ppm for alloy 7A which

is within the range given for optimum boron content in the literature [4,11,18,22]. Acicular ferrite microstructures are obtained in alloy 7A for cooling rates greater than t(800 - 500°C) = 300s (fig.4.19c). With slower cooling rates, some polygonal ferrite is formed and MA islands are replaced by degenerate pearlite islands (fig.4.19d and 4.20c). Extra fine grained acicular ferrite with numerous small MA islands is found in specimen 7-30 (fig.4.19b and 4.20b). Specimen 7-3 has a completely martensitic microstructure (fig. 4.19a) as expected from the CCT diagram (fig. 4.18). Figure 4.20a shows the fine grained low carbon martensite with small MA islands between the laths. Alloy 7A has higher hardenability than alloys 1A and 5A at the faster cooling rates because of its higher carbon content and also because it contains 0.36% copper.

The boron autoradiograph of specimen 7-30 shows some segregation of boron to the austenite grain boundaries (fig.4.21e and 4.21f) but also a fairly large amount of boron precipitates inside the austenite grains. These may be BN and/or $Fe_{23}(C,B)_6$ precipitates due to the higher carbon and nitrogen contents in alloy 7A.

Figure 4.22 shows the variation in Vickers hardness of alloys 1A, 5A and 7A as a function of the cooling rate. Alloy 5A has slightly lower hardness values than alloy 1A because of its lower hardenability. As described previously, the lower hardenability of alloy 5A at fast cooling rates is due to its lower manganese content, compared to alloy 1A. At slow cooling rates , the lower hardness of alloy 5A may be the result of increased amount of ferrite grains resulting from nucleation on the boron precipitates at the grain boundaries. Because of its larger boron content (0,0037%), alloy 5A is more likely than alloy 1A (which contains 0,0016% boron) to have boron precipitation on the austenite grain boundaries of specimens cooled at slow cooling rates (compare fig. 4.21a and 4.21c). This hypothesis has not been verified.

The highest hardness values were attained in alloy 7A for cooling rates faster than t (800-500°C) = 100s (fig. 4.22). This is due to the higher carbon and copper contents which lower the transformation temperature and impart solid solution strengthening to this alloy. However transformation behaviour of alloy 7A does not show the cooling rate independence observed for alloys 1A

and 5A. As a result, microstructures of alloy 7A for slow cooling rates are composed of polygonal ferrite and acicular ferrite and the specimens have lower hardness than for specimens of alloys 1A and 5A with similar cooling rates. Cooling rate independence of the transformation behaviour is therefore associated with hardenability obtained by boron additions, not by higher carbon or alloy contents. Carbon and alloy additions reduce the range of cooling rates over which boron is effective.

4.2.4 Fraction Transformed vs Temperature Plots for Alloys 1A, 5A and 7A

Figures 4.23, 4.24 and 4.25 show the fraction transformed vs temperature plots obtained over a range of cooling rates for alloys 1A, 5A and 7A. For all three alloys, the change from slow to fast cooling rates resulted in a displacement of the transformation curve to the left, i.e. to the lower temperatures. Higher transformation temperatures correspond to more polygonal ferrite type transformation products whereas low transformation temperatures result in bainitic type transformation products such as acicular ferrite. This effect is more obvious in alloy 7A. Specimen 7-3 has a final microstructure composed of low carbon martensite and its transformation is 50% complete at approximately 300°C. Transformation of specimen 7-1000 is 50% complete at about 670°C and its microstructure is a mixture of polygonal ferrite, acicular ferrite and degenerate pearlite islands.

Fraction transformed vs temperature plots for specimens 1-300, 5-300 and 7-300 (cooled at a cooling rate corresponding to air cooling of a 13 mm thick plate) are shown in figure 4.26. For all three alloys, most of the transformation takes place below the AFs temperature (about 650°C) which indicates that very little polygonal ferrite is formed at this cooling rate. If the temperature at which 50% of the transformation is complete is taken as a criteria to evaluate the hardenability of the specimens, then the alloys can be listed in order of increasing hardenability as 7A, 1A, and 5A (for a cooling rate of t (800-500°C) = 300s). From this comparison it can be concluded that for 13 mm thick, air cooled material, a boron addition of 16 ppm is preferable over a 37 ppm addition when the boron is fully effective. The results also indicate that an additional hardenability increment can be gained

by adding more carbon and copper to the alloy. However, it is preferable to obtain the required hardenability by boron additions than with added carbon and copper because boron imparts a greater cooling rate independence to the transformation behaviour. This is a beneficial effect if thicker plates are to be made of the material.

4.3 Influence of Processing Parameters on the Transformation Behaviour of the Experimental Boron HSLA Steels

4.3.1. Comparison of As-rolled and Air Cooled Steels with the CCT Diagram Specimens

When the microstructure and hardness of alloys 1A, 5A and 7A in the as-rolled and air cooled state are compared with those of the dilatometry specimens with comparable cooling rates (specimens 1-300, 5-300 and 7-300), it is apparent that a greater boron hardenability effect is obtained during the dilatometer experiments than for the as-rolled and air cooled material (Table 4.3).

For example, microstructure of alloy 1A in the as-rolled and air cooled condition is composed of acicular ferrite and polygonal ferrite whereas specimen 1-300 has completely acicular ferrite microstructure. Correspondingly, hardness of alloy in the as-rolled and air cooled condition is less than that of specimen 1-300. Similar observations can be made for alloys 5A and 7A. The as-rolled and air cooled materials have volume fractions of MA comparable to those of the dilatometry specimens: alloy 1A has 9,4% MA whereas specimen 1-300 contains 12,7%. As observed previously, the hardness of these materials is not related to their volume fraction of MA but to the amount of acicular ferrite present.

In the dilatometry specimens, boron is well segregated to the austenite boundaries and few large boron precipitates are observed (fig. 4.21a, 4.21c and 4.21e). In the as-rolled material, boron segregation is more diffuse and there is strong evidence of boron precipitation on inclusion stringers (fig. 4.6a, 4.6c, 4.6d). During dilatometry testing, the austenite is given a smaller percentage of deformation than during controlled rolling of the plates.

Consequently, it is expected that the dilatometry specimens will show a more intense grain boundary segregation than the as-rolled material because they will have fewer deformation induced defects inside the grains for the boron to segregate to. Theoretically, sufficient boron has been added to alloys 1A, 5A and 7A to insure that enough free boron will segregate to the ferrite nucleation sites even in heavily deformed material. However it appears that there is a lesser amount of boron free to segregate in the as-rolled material than in the dilatometer specimens.

These differences in boron hardenability effect can be explained in two different ways. In the first hypothesis, it is assumed that a similar boron distribution is found in the as-rolled material and in the dilatometry specimens before processing. Any difference in boron segregation is therefore caused by the differences between the processing schedule used for dilatometry testing and the rolling schedule used to make the as-rolled plates.

In the second hypothesis, the difference in boron hardenability effect is due to the difference in boron distribution existing before the austenite is subjected to deformation. For example, the austenitizing practices used in rolling of the plates and dilatometry testing are different. Also the starting material is the as-cast ingot in one case while it is the as-rolled plate for the other. These hypotheses will be examined in greater detail in the following sections.

4.3.2 Effects of Dilatometer Processing Schedule on the Transformation Behavior.

Effect of Deformation Schedule

During the dilatometer experiments, the austenite was deformed to 50% of its original length in one step and at a temperature below the recrystallization stop temperature (825°C). The rolling schedule used for rolling the experimental boron steels involved 15 to 16 passes with some passes above the recrystallization stop temperature and some below (Table 3.2). One of the most important differences between the dilatometer test and the actual rolling of plates is therefore the deformation schedule itself. It is possible that recrystallization during rolling has caused a dilution of the boron

concentration at the austenite boundaries by moving the boundaries away from the boron atmosphere and by retarding further boron segregation during rolling. In order to verify this hypothesis, dilatometry specimens of alloy 1A were subjected to various deformation schedules, some involving recrystallization and others having no recrystallization (see Table 3.5, specimens 1-300, 1A, 1C and 1G).
Fraction transformed vs temperature plots for specimens 1-300, 1A, 1C, and 1G are shown on fig. 4.27. The transformation behaviour of the specimens is very similar: the temperature for 50% transformation is in the range of 615-630°C for all of them (Table 4.4). A lower 50% transformation temperature indicates a stronger boron effect because it means an increase in the volume fraction of low transformation temperature constituents (such as acicular ferrite) as opposed to high transformation temperature constituents (such as polygonal ferrite).

The effectiveness of the boron addition seems to increase somewhat if deformation is applied in one step (specimen 1-300) instead of two steps (specimen 1G) at the same deformation temperature. The highest hardenability is obtained when deformation is carried out in two steps: one above and the other below the recrystallization stop temperature (specimen 1A). However, these effects are small (probably inside the error margin for dilatometer results), indicating that the boron effectiveness is not significantly affected by the deformation schedule.

All four specimens (1-300, 1A, 1C and 1G) have microstructure composed of acicular ferrite interspersed with MA island (fig. 4.12c, 4.28a, 4.28b and 4.28c) as anticipated from the transformation temperature range. Elongated austenite boundaries are visible in specimens 1A, 1G, and 1-300 indicating that the austenite was deformed in the non recrystallization regime. In specimen 1C (fig. 4.28c), recrystallization of the austenite has occurred after both deformation steps at 1050°C therefore, the austenite grain boundaries have an equiaxed shape. Some large bainite islands are also present in specimen 1C (fig. 4.28d). Specimen 1C has lower hardness than the other specimens (Table 4.4) because it was allowed to cool at a rate of about 1°C s^{-1} between 1050°C and 800°C whereas a faster cooling rate of 60°C s^{-1} (t (1100-850°C) ~ 5s) was used for the other specimens (see Table 3.5). This may have resulted in lower

NbC precipitation strengthening in specimen 1-C. However this appears to have had no significant effect on the boron segregation behaviour as evidenced by the transformation temperature. Figures 4.29a and 4.29b show boron autoradiographs taken from dilatometry specimen 1A. As discussed in part 3.2 of the experimental procedure, which dealt with deformation dilatometry, the deformation of dilatometry specimens is not homogeneous (fig. 3.1b). In fig. 4.29b, the elongated austenite boundaries of the middle part of the specimen (which is subjected to the deformation) are outlined by segregated boron. This correlates with the strong boron hardenability effect observed for specimen 1A. In fig. 4.29a, the austenite grains are undeformed because this region of the specimen is not subjected to deformation during the test. The boron segregation at the austenite grain boundaries is more intense in the undeformed part of the specimen than in the deformed part. In the deformed part of the specimen, boron segregates to deformation induced defects such as deformation bands and twin boundaries inside the austenite grains [10,11,12], hence there is less boron available for grain boundary segregation.

Effect of Holding Time Between Deformation Steps

During the dilatometer tests, the holding time between deformation steps and before final cooling is very short: 10 to 15 seconds (see Table 3.5). There is little time for NbC precipitation during processing. In the as-rolled material, the longer cooling time between passes and holding time prior to final cooling may have permitted a more extensive NbC precipitation to occur. A depletion in soluble niobium may then have been a cause of the weaker hardenability effect observed in the as-rolled steels. To investigate this possibility a dilatometer test was performed using a longer holding time of 150 seconds before cooling (specimen 1D, Table 3.5). The transformation behaviour of specimen 1D is compared with that of specimen 1A on fig. 4.30. The temperature for 50% transformation is some 20°C higher for specimen 1D than for specimen 1A indicating that there is some loss in hardenability associated with the longer holding time. Specimen 1G which was deformed 25% twice at 825°C, had the highest transformation temperatures (see fig. 4.27) of the other deformation schedules investigated. It is possible that during the two deformation steps at 825°C, a more extensive NbC precipitation occured in this specimen, thereby decreasing its hardenability.

However, both specimen 1D (fig. 4.31) and specimen 1G (fig. 4.28b) have fully acicular ferritic microstructures. Therefore, it can be concluded that the amount of niobium in solution is not the critical parameter controlling the hardenability of the experimental boron steels.

4.3.3. Effect of the Boron Distribution Prior to Processing on the Transformation Behaviour

Nature of the Starting Material

The starting material for the as-rolled plate is the as-cast ingot whereas the dilatometry specimens used to construct the CCT diagrams were machined from as-rolled plate. In order to verify whether the difference in boron distribution prior to processing due to the difference in starting materials would persist until transformation, specimen 1B-300 was machined from as-cast material (alloy 1B) and was subjected to the same processing schedule as specimen 1-300 (see Table 3.5). Fraction transformed vs temperature plots for specimens 1-300 and 1B-300 are shown on fig. 4.32. Specimen 1-300 has a temperature for 50% transformation which is some 25°C lower than specimen 1B-300 (Table 4.5). The transformation start temperature for specimen 1C-300 is also significantly higher than for 1-300. Microstructure of specimen 1-300 is acicular ferrite with fine MA islands (fig. 4.12c) whereas specimen 1B-300 has a microstructure composed of fine grained polygonal ferrite with a small volume fraction of acicular ferrite and MA islands (fig. 4.33). Correspondingly, specimen 1-300 has higher hardness (218 VHN_{10}) than specimen 1B-300 (188 VHN_{10}). It is obvious from these observations that specimen 1-300 has higher hardenability than specimen 1B-300 and that there must be a greater amount of boron segregation to the ferrite nucleation sites in specimen 1-300 than in specimen 1B-300.

Inclusions in dilatometry specimen 1B-300 (machined from as-cast alloy 1B) were analysed using EDAX (fig 4.34). Typically, inclusions were grouped as in fig. 4.34a. They were composed of variable proportions of aluminum, manganese, titanium and sulfur. Some were Al-rich (fig. 4.34b) while others showed higher proportions of manganese and sulfur (fig. 4.34c). Many inclusions were composed of more than one phase (fig. 4.34d), the different

parts of the inclusions having variable proportions of aluminum and manganese.

In dilatometry specimen 1-300 (machined from as-rolled plate of alloy 1A), the inclusions were smaller and more evenly dispersed. No large clusters of inclusions (as in specimen 1B-300, fig. 4.34a) were found. The individual inclusions had a composition varying between a very strong aluminum enrichment (fig. 4.35a) and a mixture of aluminum, manganese, titanium and sulfur (fig. 4.35b). The inclusions in specimen 1B-300 are very similar to those in specimen 1-300 with respect to composition. The difference between the two specimens resides in the size and distribution of those inclusions. The iron (Fe) peaks in the EDAX spectra of fig. 4.34 and 4.35 probably originate from the matrix surrounding the inclusions. Because of the relatively large area analysed by the SEM it is difficult to avoid picking up X-rays from the matrix, especially with the smaller narrow inclusions. Fig. 4.35c shows the spectrum obtained from the matrix of specimen 1-300.

Specimen 1B-300, which was machined from the as-cast ingot, had more inclusions in large groups and contained some mixed inclusions. This specimen therefore had more sites for $M_{23}(C,B)_6$ and/or BN precipitation as it is known that Al_2O_3 and MnS type inclusions are nucleation sites for boron precipitation. Boron precipitation on the inclusions would leave entire areas with less free boron to segregate to the ferrite nucleation sites and lower the hardenability.

Specimen 1-300, on the other hand, was machined from as-rolled plate. In the as-rolled plate, the groups of inclusions and the mixed inclusions present in the as-cast ingot have been broken down into stringers by the substantial reductions introduced by rolling. This material is subjected to further reduction during the dilatometer test and the stringers are broken down into well dispersed individual inclusions as observed in specimen 1-300. This process also helps to dissolve any boron precipitates inherited from the as-cast ingot. Specimen 1-300 therefore contained less precipitation sites for $M_{23}(C,B)_6$ and BN. With more boron being free to segregate to the ferrite nucleation sites, this specimen had satisfactory boron hardenability and 100% acicular ferrite microstructure was obtained upon cooling.

It is concluded that the most important factor contributing to the difference in transformation behaviour between the as-rolled and air-cooled material and dilatometry specimens is the difference between the starting materials used in both cases. It would appear therefore that a simple way of restoring full boron effectiveness to the as-rolled material would be to subject it to further deformation, as in the dilatometry testing.

Effect of Austenitizing Practice

The dilatometry specimens used to construct the CCT diagrams were austenitized for 15 minutes at 1100°C whereas the ingots were soaked for two hours at 1100°C prior to rolling. It is not feasible to maintain specimens at 1100°C for two hours inside the dilatometer. However, specimens austenitized at 1175°C for 15 minutes should be subjected to a greater homogenization effect than when austenitized at 1100°C for 15 minutes. Dilatometry specimen 1L was therefore austenitized 15 minutes at 1175°C and subjected to the same processing schedule as specimen 1A to find out whether the difference in austenitizing practice might have contributed to the difference in hardenability between dilatometry specimens and as-rolled material. Figure 4.36a shows the resulting fraction transformed vs temperature plots. No significant difference in transformation behaviour is observed between specimens 1A and 1L. The microstructure for specimen 1L is very similar to that of specimen 1A, being composed of acicular ferrite with small MA islands (fig. 4.36b). Despite the higher austenitizing temperature used for specimen 1L, there is no large difference between the austenite grain size of specimens 1A and 1L (Compare fig. 4.28a and 4.36b). The titanium and niobium carbonitrides present in these steels exert adequate control over austenite grain growth during austenitizing. It is therefore concluded that the difference in austenitizing practice is not a significant factor in explaining the difference in transformation behaviour between dilatometry specimens and as-rolled material.

4.3.4 Simulation of the Dilatometer Testing on the Rolling Mill

Among the processing parameters investigated in the preceding sections (deformation schedule, holding time between deformation steps, nature of the starting material and austenitizing practice), the nature of the starting material (as-cast vs as-rolled) is the only difference between dilatometer testing and rolling of the plates that seems to have a significant effect on the transformation behaviour. To corroborate these observations, a coupon of as-rolled and air-cooled material (alloy 1A) was subjected to a rolling schedule duplicating that used for the dilatometry specimens. The 13 mm thick plate was austenitized for 20 minutes at 1100°C, given 25% reduction at 825°C followed by a second 25% reduction at 815°C. The resulting 8 mm thick plate was air-cooled. Microstructure of 8 mm thick plate is completely acicular ferritic with small MA islands (fig. 4.37a and 4.37b). This microstructure is very similar to the microstructures obtained in dilatometry specimens with comparable cooling rates (specimens 1-30, fig 4.12b and 1-100, fig 4.37d). The austenite grain size of the 8 mm plate is also similar to that of dilatometry specimen 1-30 (Compare fig. 4.37c with fig. 4.21b).

In table 4.6, mechanical properties of 8 mm thick alloy 1A are compared to those of 13 mm thick material. The yield and tensile strengths are increased by the dilatometer testing simulation schedule. However, the toughness of the 8 mm thick plate of alloy 1A is decreased compared to the 13 mm thick plate. The 8 mm thick plate was tested using half size Charpy specimens while full size specimens were used for the 13 mm thick plates. Normally, smaller size specimens have lower transition temperatures than larger specimens of the same material. Therefore, the toughness values of the 8 mm and 13 mm thick plates cannot be directly compared. The fracture surfaces of the half size Charpy specimens broken at -100°C show quasi cleavage with some secondary cracking but no intergranular facets. (fig. 4.38). Specimens broken at -70°C have mixed fracture morphologies composed of quasi cleavage with small dimples whereas only dimples are found on the fracture surfaces of specimens tested at room temperature (fig. 4.38). Comparison of these fracture characteristics with the morphologies found in Charpy specimens of 13 mm thick alloy 1A tested at the same temperatures (fig. 4.8 and 4.9) indicates that although the dilatometer simulation schedule did decrease the low temperature

toughness of alloy 1A, adequate impact resistance is still retained. The lower toughness of 8 mm thick alloy 1A may be due to the higher yield strength achieved in this material.

It is concluded that the difference in hardenability between the as-rolled and air-cooled plates and the dilatometry specimens is due to the difference in starting material (as-cast vs as-rolled) between the two processes. Therefore when a coupon of as-rolled alloy 1A was subjected to a schedule duplicating the dilatometer testing schedule, the resulting material had a microstructure very similar to that of dilatometry specimens. The mechanical properties of the alloy were modified in a way consistent with an improvement in hardenability. The increased volume fraction of acicular ferrite in the 8 mm thick material (compared to the 12,7 mm thick plate) resulted in improved strength with slightly reduced toughness. The boron hardenability effect can therefore be improved in alloy 1A by the simple means of reaustenitization at 1100°C followed by 50% deformation at 825°C and air cooling.

4.3.5 Microstructure of the Experimental Boron Steels in the As-cast and Annealed States

It was seen in the previous sections that the austenitizing and rolling schedules used to process the as-cast ingots were insufficient to achieve full boron hardenability in the experimental steels. An optimum boron effect on hardenability was only observed when the as-rolled material was subjected to further austenitizing and processing. The microstructure of some as-cast ingots was therefore examined to determine why it was not possible to achieve a homogeneous boron distribution prior to processing.

Microstructure of as-cast alloy 1B is shown in fig. 4.39. It is composed of large polygonal ferrite grains with pearlite islands. Austenite grain boundaries are outlined by precipitates (fig. 4.39a). Etching the specimen with boiling saturated aqueous picric acid revealed the presence of precipitates on the ferrite grain boundaries as well (fig. 4.39b). To identify these precipitates, carbon replicas were taken from an etched sample of alloy 1B and observed in the transmission electron microscope (fig. 4.41d). Figure 4.41a shows a row of dendritic precipitates. Analysis of SAD patterns taken

from these precipitates revealed them to be (Ti, Nb)C (fig. 4.41b). Needle-like precipitates (fig 4.41c) are composed of NbC. Such dendritic (Ti,Nb)(C,N) precipitates have been reported [76] in HSLA steels with similar niobium and titanium contents. The core of the dendrites is found to be Ti and N rich whereas the arms contain a greater proportion of Nb and C.

Because of its higher carbon and boron content (see Table 3.1), alloy 5B has higher hardenability than alloy 1B. Microstructure of as-cast alloy 5B is therefore more acicular than that of alloy 1B (compare fig. 4.40a and 4.39a). The ferrite grain size of as-cast alloy 5B is very non homogeneous (fig 4.40b) with some huge grains being present. As in alloy 1B, some austenite grain boundaries are outlined by precipitates (fig. 4.40b).

Figures 4.39c and 4.40c show boron autoradiographs of as-cast alloys 1B and 5B. In both materials, the austenite grain boundaries are outlined by segregated boron atoms but there is no boron on the actual boundaries. This is more obvious in alloy 5B because the boron content of this alloy is higher. These features can be explained by the fact that the boron segregation has taken place after the boundaries were decorated by the (Ti,Nb)(C,N) precipitates described above. It is reported in the literature that the (Ti,Nb)(C,N) dendrites are formed at high temperatures [76]. It is not sure whether the coarse particles visible on the autoradiographs are in effect due to boron, but they could have been caused by boron precipitates nucleated on large inclusions. Figure 4.42 shows this type of inclusion in alloy 1B.

4.4 Influence of Effective Boron Content on the Transformation Behaviour of the Experimental Boron Steels

Dilatometry experiments were performed in order to quantify the effects of boron and nitrogen contents on the transformation behaviour of experimental boron steels. The carbon, nitrogen, titanium and boron contents of the dilatometry specimens are given in Table 4.7 and the processing schedule used is given in Table 3.6.

The fraction transformed vs temperature plots obtained for these three specimens are shown on fig. 4.43. Specimen 0-300 (containing no boron)

begins to transform at 785°C and transformation is 90% complete at 635°C. Microstructure of specimen 0-300 is therefore polygonal ferrite with a small amount of pearlite (fig. 4.44a). Specimen 1-300 illustrates the strong effect of boron in suppressing the $\gamma \rightarrow \alpha$ transformation. Transformation of specimen 1-300 (containing 0,0016% effective boron) begins at 685°C and is less than 20% complete at 635°C. Correspondingly, microstructure of specimen 1-300 is acicular ferrite interspersed with MA islands (fig. 4.12c). The boron addition has resulted in a much lower transformation temperature range and an acicular ferrite microstructure.

It is well known that in order for boron to be fully effective as a hardenability promoter, the formation of boron nitride must be prevented. This can be achieved either by controlling the nitrogen content during steel-making so that there is very little free nitrogen in the steel or by adding strong nitride forming elements such as titanium and aluminum [4,5]. As mentioned previously, the effective boron content of the alloy can be described using the relationship developed by Kapadia and coworkers [5,31]:

$$B_{eff} = B_{tot} - [N - 0{,}002 - Ti/5]$$

Using this formula, the effective boron content of alloy 1A is equal to the total boron content, i.e. 0,0016% boron. This means that the titanium addition in alloy 1A is sufficient to eliminate all the free nitrogen so that all the boron is effective. In alloy 1C however, there is not enough titanium to trap all the nitrogen because of the large nitrogen content (102 ppm). Therefore the formula predicts that no effective boron is left in the alloy. The transformation behaviour of specimen 1C–300 seems to indicate that some boron is effective despite the high nitrogen content. Transformation of specimen 1C-300 begins around 740°C and proceeds at temperatures significantly lower than for specimen 0-300 (see fig. 4.43). Microstructure of specimen 1C-300 is apolygonal ferrite with some small MA island (fig. 4.44b and 4.44c) whereas specimen 0-300 is polygonal ferrite with pearlite islands (fig. 4.44a).

Two possible explanations can be put forward to explain the higher hardenability of specimen 1C-300 compared to specimen 0-300. The first

explanation is that specimen 1C-300 still benefits from a small boron effect because aluminum and other microalloying elements such as niobium are present in sufficient amounts to compensate for the excess nitrogen not tied up with titanium. This implies that in the formula used to calculate the effective boron content, the term 0,002 (which corresponds to nitrogen normally tied up with aluminum, silicon and vanadium [19]) underestimates the effect of these elements. However, boron autoradiographs of specimen 1C-300 show intense boron precipitation at the austenite boundaries and inside the austenite grains (fig. 4.44d). Such pronounced boron precipitation was not observed in dilatometry specimens of alloy 1A (fig. 4.21a). Since alloys 1A and 1C have very similar carbon contents (see Table 4.7), these precipitates cannot be $M_{23}(C,B)_6$. In view of the high nitrogen content of alloy 1C, the precipitates are most probably BN. It is then possible that the very fine apolygonal ferrite obtained in specimen 1C-300 is not due to a small boron hardenability effect but to enhanced ferrite nucleation on the numerous BN precipitates. By acting as nucleation sites for the ferrite, the BN precipitates promote a high ferrite nucleation rate which would explain the extra fine grain size obtained in the final microstructure. Such an enhanced ferrite nucleation rate due to the presence of BN precipitates has been observed by other workers [14,52,53].

4.5 As-Rolled and Accelerated Cooled Experimental Boron Steels

4.5.1 Review of Accelerated Cooling

Kozasu [71] defines accelerated cooling as "the cooling of wide and heavy plate after hot rolling at such intermediate cooling rate that the processed plates can be used in the as-rolled state without tempering". The rolled plates are accelerated cooled through the transformation temperature range (typically 800 to 500°C) and air cooled to room temperature. The optimum cooling rate is influenced by the chemical composition of the steel. It is generally chosen around 10°C/s but faster cooling rates can be used with lean steels. However, the formation of a large volume fraction of martensite is to be avoided.
The effect of accelerated cooling is to suppress or retard polygonal ferrite and pearlite formation, producing a completely bainitic or acicular ferritic structure [72]. The ferrite grain size is refined and the ferrite itself is strengthened due to supersaturation of carbon, transformation induced

dislocations and an increased volume fraction of fine carbides in microalloyed steels [73]. Accelerated cooled steels have a more uniform microstructure because the temperature range over which most of the transformation occurs is narrowed [72].

Accelerated cooling reduces the ferrite grain size by lowering the $\gamma \rightarrow \alpha$ transformation temperature which in turn increases the ferrite nucleation rate and decreases the ferrite growth rate [71]. An increase in cooling rate increases the supercooling with a corresponding increase in ferrite nucleation rate. This results in finer ferrite grain sizes. Another important effect of accelerated cooling is that a larger volume fraction of ferrite grains is forced to form at much lower temperatures because of the increased cooling rate [74]. These ferrite grains will be smaller because they have less time to grow during cooling of the steel. The extent of ferrite grain refinement is limited in the case of transformation from equiaxed austenite due to the fact that only preferential sites on the austenite grain boundaries are able to nucleate ferrite. Some degree of controlled rolling is therefore required to condition the austenite prior to cooling. Deformation below the austenite recrystallization temperature given controlled rolling increases the number of heterogeneities in the austenite which serve as ferrite nucleation sites: increased austenite grain boundary area, deformation bands (deformed annealing twins), second phase particles and subgrain boundaries [71].

Among the advantages of accelerated cooling, the most important is surely an improvement in strength without deterioration in the fracture appearance transition temperature due to the smaller grain size.[71]. Alternatively, a reduced chemical composition or carbon equivalent can be used to obtain a specified strength, resulting in greater ease of fabrication. By allowing the use of lower hardenability steels, accelerated cooling improves weldability. The ductility and shelf energy of accelerated cooled steels is improved because they show less microstructural banding. This also results in a decrease in the extent of separations found in accelerated cooled controlled rolled steels [71].

4.5.2 Microstructure

The use of accelerated cooling instead of air cooling after the final pass was investigated. It was hoped that the faster cooling rate would produce a fully acicular ferrite microstructure and improve the strength levels of the as-rolled steels without having to resort of composition modification. Steels 1B, 2B, 5B and 7B (see Table 3.1 for their composition) were processed according to the schedule given in Table 3.2 (schedule #2: revised schedule) and immersed in an oil-water bath immediately after rolling to produce an accelerated cooling rate of about 8°C s^{-1}.

Microstructure of accelerated cooled steels 1B, 2B, 5B and 7B was composed of fine grained acicular ferrite interspersed with martensite-austenite microconstituents (fig. 4.45). Alloy 5B has a slightly larger ferrite grains size than the other three steels (compare fig. 4.45c with fig 4.45a, 4.45b and 4.45d) and its microstructure also contains fine polygonal ferrite grains (fig. 4.46c). In alloys 1B and 2B, MA islands decorate the acicular ferrite grains boundaries and sub boundaries (fig. 4.46a) whereas in alloy 7B, the MA islands are more equiaxed and uniformly dispersed throughout the microstructure (fig. 4.46d). Some bainite islands are also present in steel 7B (fig. 4.46d).

Figure 4.46b shows a large acicular ferrite grain with accented etching relief. It is unclear whether this "raised" ferrite is a distinct phase. It is found in acicular ferrite steels and seems to be associated with areas of high dislocation density. Volume fraction of "raised" ferrite varies with steel composition and processing but it is difficult to determine quantitatively because the raised ferrite islands can be identified only on high magnification SEM micrographs.

Comparing the microstructures of the as-rolled and accelerated cooled alloys 1B, 2B, 5B and 7B (fig. 4.45) with those of the corresponding air cooled alloys 1A, 2A, 5A and 7A (fig 4.1) it is apparent that the accelerated cooled alloys have less microstructural banding than the air cooled alloys. For instance, alloy 7A (fig 4.1d) has bands of smaller and larger polygonal ferrite grains with bands of high carbon microconstituents (MA, bainite and degenerate pearlite) interspersed between. On the other hand alloy 7B has a

microstructure composed of acicular ferrite grains with a relatively uniform grain size (fig. 4.45d) and the MA islands are dispersed throughout the ferrite matrix.

Figures 4.47a and 4.47c show the fine acicular ferrite grains and subgrains with high dislocation density found in TEM micrographs of alloys 1B and 2B. Steel 5B (fig. 4.49d) has larger ferrite grains with a lower density of dislocations. Fine precipitates could be seen on the thin foils of the accelerated cooled steels (fig. 4.47b). SAD and EDS analysis of these precipitates on thin foils and replicas revealed them to be (Ti, Nb)(C,N) similar to those found in the as-rolled and air cooled alloys (see part 4.11). No attempt was made to determine the effects of accelerated cooling on the precipitation kinetics of the (Ti,N)(C,N).

4.5.3 Mechanical Properties

Mechanical properties of the accelerated cooled alloys 1B, 2B, 5B and 7B are given in Table 4.8 as well as those of air cooled alloys 1A, 2A, 5A and 7A. Comparing the properties of the lower carbon steels 1A and 1B and steels 5A and 5B, it appears that no significant increase in strength results from the use of accelerated cooling instead of air cooling. Ultimate tensile strength, hardness and volume fraction of MA of the accelerated cooled alloys 1B and 5B are smaller than those of the air cooled alloys 1A and 5A (Table 4.8). In the higher carbon alloys 2A and 2B and 7A and 7B however, the use of accelerated cooling results in a significant increase in both yield and tensile strengths with little change in ductility. Hardness of accelerated cooled alloys 2B and 7B is higher than that of air cooled alloys 2A and 7A as is their volume fraction of MA. The strength increment for the accelerated cooled alloys is a consequence of the higher amount of acicular ferrite and MA compared with the air cooled alloys. The greater effectiveness of accelerated cooling in the case of alloys 2B and 7B is due to their higher carbon content (see Table 4.9).

The strength increments obtained by accelerated cooling alloys 2B and 7B instead of air cooling as for alloys 2A and 7A are relatively small (see Table 4.8). Alloy 2B has a 52 MPa increase in yield strength and an increase of

9 VHN_{10} in hardness compared to alloy 2A whereas the yield strength of alloy 7B in 84 MPa greater and its hardness is 22 VHN_{10} greater than those of alloy 7A. The increases in tensile strength are smaller: 28 MPa for alloy 2B compared to alloy 2A and 23 MPa for alloy 7B compared to alloy 7A. The rather small effect of accelerated cooling on the mechanical properties of the experimental alloys may be explained by the relative cooling rate independence of the transformation behaviour in boron steels (see part 4.2.1). The difference in cooling rate between air cooling ($1°Cs^{-1}$) and accelerated cooling ($8°Cs^{-1}$) of 13 mm thick plates is too small to have a strong effect on the microstructure and strength of these alloys.

Table 4.10 shows the yield behaviour of some of the experimental boron steels when subjected to a tensile test. The presence of discontinuous yielding in some of the steels (alloys 1B, 5B and 7B) can be related to the higher nitrogen contents and lower volume fractions of acicular ferrite and martensite-austenite microconstituents found in those steels. Free nitrogen is known to cause discontinuous yielding in steels because the nitrogen atoms pin down dislocations, thereby reducing the mobile dislocations available for plastic deformation. In boron HSLA steels, a high free nitrogen content also reduces boron effectiveness and results in a steel containing less acicular ferrite and more polygonal ferrite. Acicular ferrrite steels have smooth flow curves when strained in tension [65, 66] because the acicular ferrite structure provides a large supply of mobile dislocations. Acicular ferrite steels also usually contain martentiste-austenite microconstituents. Formation of these MA islands causes significant elastic and plastic strains in the surrounding ferrite due to the high transformation stresses involved [75]. The combination of these two effects results in continuous yielding and a high rate of work hardening for acicular ferrite steels.

Alloys 1B, 5B and 7B have higher nitrogen contents and/or lower volume fractions of acicular ferrite and MA than alloys 1A (8 mm plate), 2B, 6A and 6B. For example, alloy 2B contains 50 ppm of nitrogen and has a completely acicular ferritic microstructure with 13,1% MA constituents. Figure 4.48a shows the continuous yielding behaviour obtained for this material. On the other hand, alloy 5B, which contains 79 ppm of nitrogen, has a microstructure composed of polygonal ferrite, acicular ferrite and only 5,9% MA

constituents. Consequently the tensile test results for alloy 5B show the presence of a yield point (fig. 4.48b).

The conditions required for boron to be effective in improving the hardenability of low carbon HSLA steels also result in continuous yielding behaviour because of the low nitrogen content required and of the highly dislocated acicular ferrite microstructure that is obtained. These steels would therefore be of interest for pipe forming and other applications where excellent formability and work hardening rates are required.

Toughness of accelerated cooled alloys 1B, 2B, 5B and 7B is excellent, with 55 J transition temperatures below -100°C. Alloys 1B and 5B have better toughness than the corresponding air cooled alloys 1A and 5A (fig. 4.49a and 4.49c). This is due to the more uniform microstructure of the accelerated cooled materials. The acicular ferrite grains are more uniform in size and there is less banding of fine grains than in the air cooled alloys (compare fig. 4.1a, alloy 1A with fig. 4.45a, alloy 1B and fig. 4.1c, alloy 5A with fig. 4.45c, alloy 5B). Despite their higher strength and toughness, alloys 2B and 7B also have better low temperature toughness than air cooled alloys 2A and 7A (fig. 4.49b and 4.49d). The beneficial effects of smaller and more uniform acicular ferrite grains overide the potential detrimental effects on toughness of the higher volume fraction of MA found in the accelerated cooled alloys. Furthermore alloys 2B and 7B contain much less bainite and degenerate pearlite islands than air cooled alloys 2A and 7A. This reduction in volume fraction of brittle microconstituents also helps improve the toughness of alloys 2B and 7B compared to alloys 2A and 7A.

Because of the low temperature reductions used in rolling these steels (the last pass was done at 770°C), there is considerable elongation of the austenite grains in the rolling direction. Microstructures of alloys 1B, 2B, 5B and 7B therefore show a significant anisotropy (see fig. 4.47). It was expected that the toughness of these alloys would be dependent upon the Charpy specimen orientation in relation to the rolling direction. Figure 4.50 shows the effect of specimen orientation on the impact toughness of accelerated cooled steels 1B, 2B, 5B and 7B. The energy values are lower in the transverse direction than in the longitudinal direction for all four alloys. Furthermore, no inclusion

shape control practice was employed during the making of the experimental boron HSLA steels. Any MnS inclusions present will be elongated in the longitudinal direction, which will enhance the anisotropy of the toughness properties in these steels [79].

4.6 Experimental Cu-Mo-B HSLA Steels

It is well known that alloying elements such as molybdenum, copper and niobium increase the hardenability of HSLA steels. It is also reported that synergistic effects on hardenability exist between elements such as Cu and B [33,34] and Mo and B [4,24]. To establish whether the addition of molybdenum and copper to the experimental boron steels would impart sufficient hardenability to attain the desired properties, alloy 6 was prepared. Part of the rolled material was air-cooled (steel 6A) and the remainder was accelerated cooled (steel 6B). The composition of Cu-Mo-B alloy 6 is given in table 3.1.

4.6.1 Microstructure

Microstructure of steel 6A is composed of acicular ferrite grains interspersed with MA islands (fig. 4.51a). The microstructure of steel 6B (fig. 4.52a) is very similar to that of steel 6A, except that the MA microconstituents are more elongated and many of them are located on the austenite grains boundaries (fig. 4.52b). Transmission electron micrographs of the two steels show that steel 6B has a higher dislocation density (fig. 4.52c) than steel 6A. However, steel 6A appears to have a greater amount of small (Ti, Nb) (C,N) precipitates (fig. 4.51b) than steel 6B.

Figure 4.53a shows a boron autoradiograph of steel 6B. Because of rolling at low temperature and subsequent accelerated cooling, there is no marked segregation of boron to the austenite grains boundaries. As with the other experimental boron steels (see fig. 4.6), boron has segregated to the deformation induced defects inside the austenite grains, resulting in an almost uniform distribution. Since boron has segregated to all ferrite nucleation sites (austenite grain boundaries and deformation induced defects), it can be concluded that boron is effective in enhancing the hardenability of alloy 6.

4.6.2 Mechanical Properties

The mechanical properties of steels 6A and 6B (table 4.11) show that some improvement in strength is gained by accelerated cooling alloy 6. However the strength increment is not as large as could be expected in view of the alloyng elements used. It is suggested that the difference in cooling rate between air cooling (approximately 1°C s^{-1} for 13 mm thick plate) and accelerated cooling (8°C s^{-1}) is not sufficient to produce a major difference in the transformation behaviour of this alloy. The hardenability of alloy 6 is such that a completely acicular ferrite microstructure is obtained when air cooling is employed. Using a cooling rate of 8°C s^{-1} only results in acicular ferrite with slightly higher dislocation density and therefore slightly higher strength. Also accelerated cooling can decrease the amount of carbonitride precipitation because with the faster cooling rate, there is less time for precipitation. This would reduce the strength increment to be gained by accelerated cooling alloy 6.

Both steel 6A and steel 6B have good toughness, with 55 J transition temperatures inferior to -60°C (fig. 4.54). Figure 4.55a shows the mixture of quasi-cleavage and dimples found on a Charpy specimen of steel 6B broken at -70°C. Although there is a large quantity of secondary cracking on this specimen, it can be seen on the oblique section (fig. 4.55b) that these secondary cracks are not due to the presence of the elongated MAs and follow a completely transgranular path. The presence of numerous secondary cracks and of quasi-cleavage on this specimen may be due to the higher dislocation density in steel 6B compared to steel 6A. Consequently, a Charpy specimen of steel 6A broken at -70°C shows much less quasi-cleavage and few secondary cracks (fig. 4.55c). An oblique section of this Charpy specimen is shown on fig. 4.55d. It can be seen that the microstructure at the root of the split is well deformed, demonstrating the intrinsic ductility of steel 6A. Steel 6A has somewhat better toughness thant steel 6B, in accordance with the strength values. Like the other accelerated cooled alloys (1B, 2B, 5B and 7B), transverse specimens of steels 6A and 6B absorb less energy than longitudinal specimens (fig 4.54) due to the anisotropy of the microstructure of these materials.

4.6.3 Comparison of Cu-Mo-B Steels With Other Experimental Boron Alloys

When steels 6A and 6B are compared to the other experimental boron steels examined in this work, it is apparent that the strength and hardness of the Cu-Mo-B composition (see Table 4.1) exceed those of all the other alloys whether air cooled (Table 4.2) or accelerated cooled (table 4.8). It is concluded that copper and molybdenum additions can be used to increase the hardenability and improve the strength levels of the extra low carbon boron containing compositions. However, these additions do result in a slight decrease in low temperature toughness. Nevertheless, all experimental boron alloys including the Cu-Mo-B steels have satisfactory toughness. This is obvious when the load vs time traces of instrumented Charpy tests performed on alloy 1B and 6B are compared (fig 4.56a and 4.56b). In alloy 6B, significant plastic deformation is required before fracture initiation (Charpy specimen tested at -40°C, fig. 4.56a). In the case of alloy 1B, which had the highest low temperature toughness of all the experimental boron alloys, considerable plastic deformation occurs before fracture initiation, even at a test temperature of -100°C (fig. 4.56b). Table 4.12 lists the fracture initiation and propagation energies for some of the experimental boron alloys. For these, as well as for the other experimental steels, the fracture initiation energy remains a significant part of the total absorbed energy down to a test temperature of -70°C. This is an indication of the excellent crack initiation resistance of these boron containing steels.

To further investigate the effects of boron on the toughness of HSLA steels, the equivalent energy fracture toughness Kd* of alloys 1B and 6A was measured using precracked Charpy specimens (see section 3.4.3). According to the Charpy impact test results, alloy 1B has very good toughness (fig 4.49a) whereas the toughness of alloy 6A is not quite as good (fig. 4.54). Figure 4.57 shows the precracked Charpy test results for alloys 1B and 6A. The fracture toughness of both alloys is rather similar, especially at low test temperature. When tested at -100°C, alloy 1B has an equivalent energy fracture toughness value of about 100 $MPa.m^{-1}$ whereas the fracture toughness of alloy 6A varies between 67 and 86 $MPa.m^{-1}$. These variations are related to splittings occurring in some specimens during the impact test.

The results indicate that for both alloys, the transition from ductile to brittle behaviour occurs at a low temperature and that adequate fracture toughness is maintained down to test temperatures of -100°C.

4.6.4 Effects of Heat Treatment on Experimental Boron HSLA Steels

To investigate the effects of heat treatment on the experimental boron HSLA steels, coupons of alloys 2B and 6B were reaustenitized for one hour at 950°C and water quenched. The coupons were then tempered at 600°C for one hour and water cooled. Heat treatments were carried out in neutral salt baths. Table 4.13 shows the hardness of the resulting materials. Both alloys are harder in the quenched and tempered state than in the as-rolled state. This is due to the good hardenability of alloys 2B and 6B. When the coupons are subjected to fast cooling after austenitization (water quenching), lath acicular ferrite microstructures are produced (fig. 4.58a and 4.58c). The higher hardenability of alloys 2B and 6B is caused by the higher additions of carbon, boron, molybdenum and copper that were made to these alloys (see Table 3.1). Even after tempering, the lath acicular ferrite retains a sufficient dislocation density and has good hardness.

Quenched and tempered alloy 6B is harder than quenched and tempered alloy 2B because alloy 6B contains more copper and molybdenum and therefore has higher hardenability than alloy 2B. Copper also provides solid solution strengthening of the matrix, resulting in an additionnal strength increment for alloy 6B [78]. The amount of copper added to alloy 6B (0,305%) is probably not sufficient to provide significant precipitation strengthening.

In comparison with the as-rolled materials, there are very few MA islands in the quenched and tempered alloys (fig. 4.58b). Figure 4.59 compares the impact properties of quenched and tempered alloys 2B and 6B with those of the as-rolled materials. For alloy 6B, the quenched and tempered material has better low temperature toughness than the as-rolled material. This may be due to the large volume fraction of elongated MA islands in as-rolled alloy 6B. In comparison quenched and tempered alloy 6B has very few of the brittle MA microconstituents. In the case of alloy 2B, the as-rolled material has better

toughness than the heat treated material although the decrease in toughness is not very large. (fig 4.59). These results show that for Cu-Mo-B alloy 6B, there is a significant advantage in heat treating the as-rolled material. Both strength (as hardness) and toughness are enhanced by the reaustenitization plus tempering treatment. For alloy 2B however, there is little to be gained by subjecting the as-rolled plate to heat treatment. The quench and temper treatment used in this study resulted in an increase in hardness for alloy 2B, but this was offset by a concurrent decrease in toughness. It can be concluded that using Cu-Mo-B compositions and appropriate heat treatment, higher strength and good toughness can be obtained with low carbon, low alloy steels. However, further research is required to define the composition and heat treatment which will provide the optimum mechanical properties, weldability and economical fabrication.

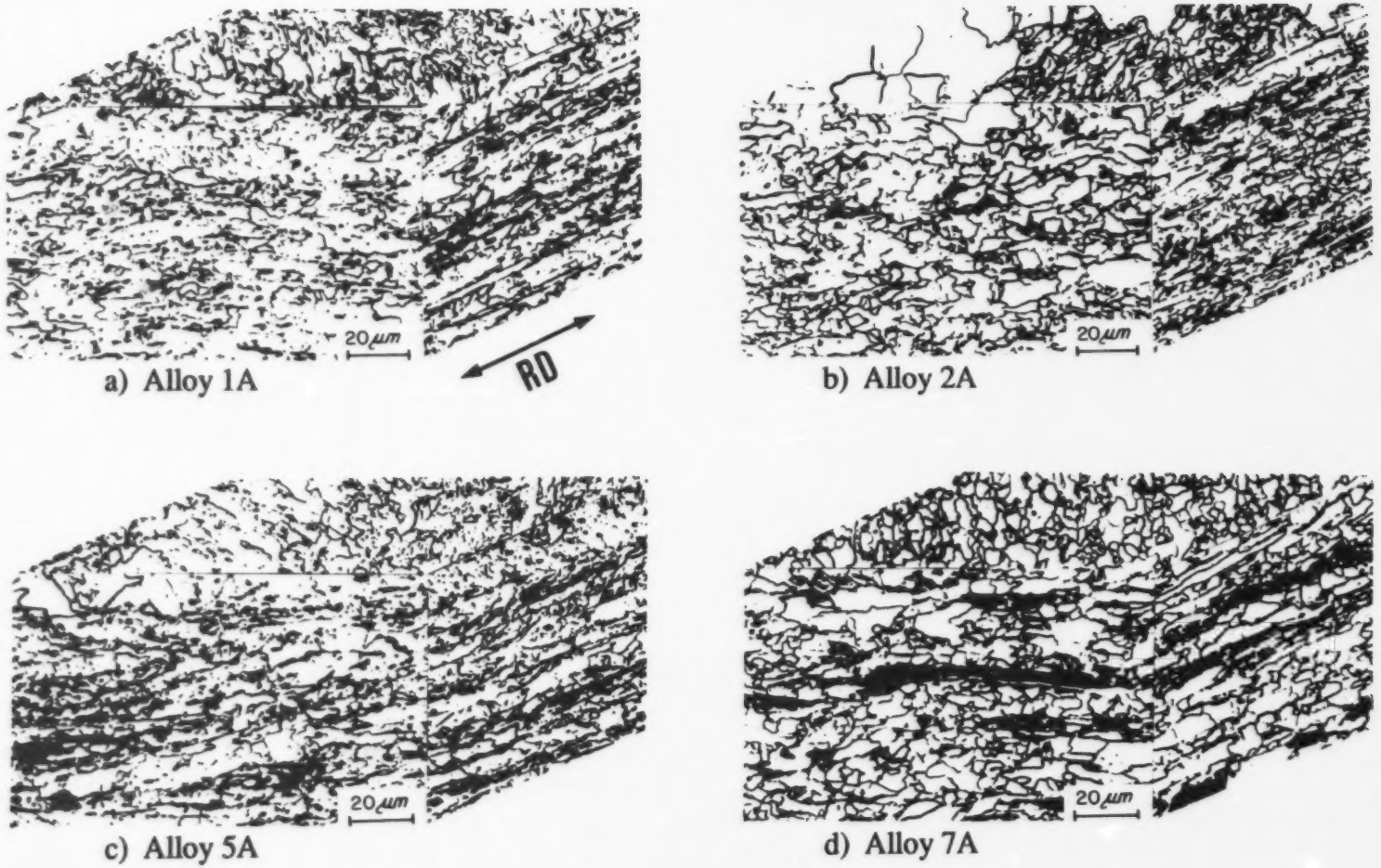

Fig. 4.1 Microstructure of as-rolled and air-cooled alloys.

a) Alloy 2A (surface section)

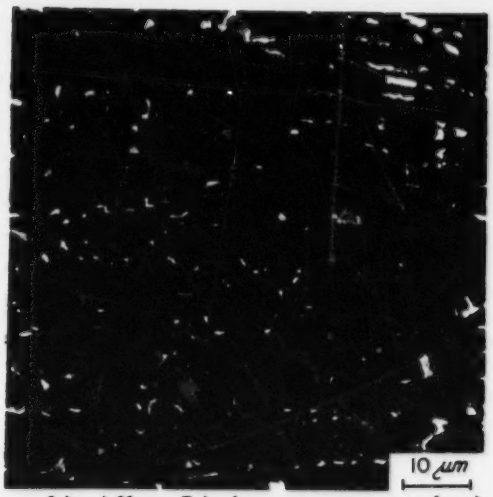

b) Alloy 5A (transverse section)

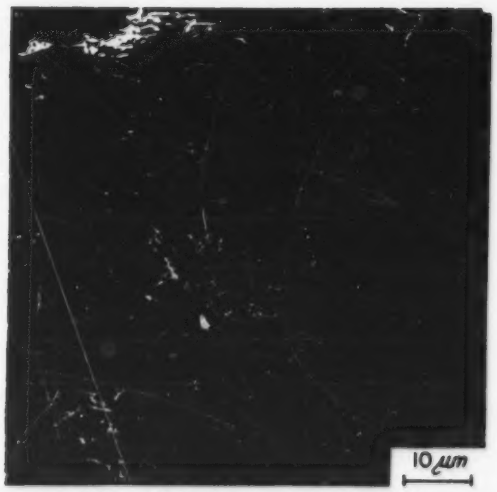

c) Alloy 7A (transverse section)

Fig. 4.2: Microstructural features of as-rolled and air cooled alloys.

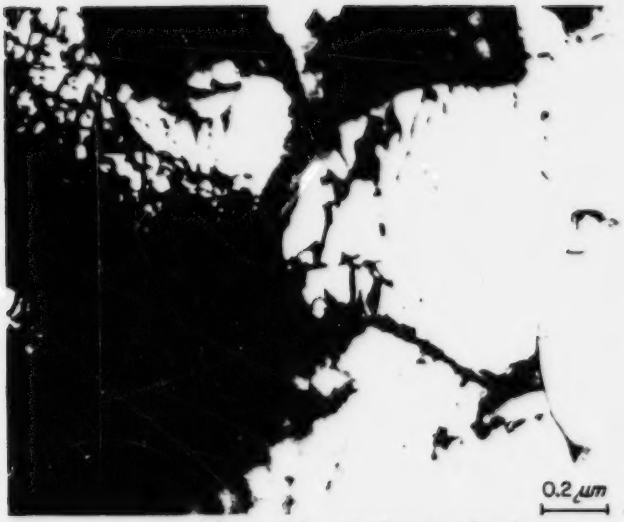

a) Alloy 1A: Acicular ferrite

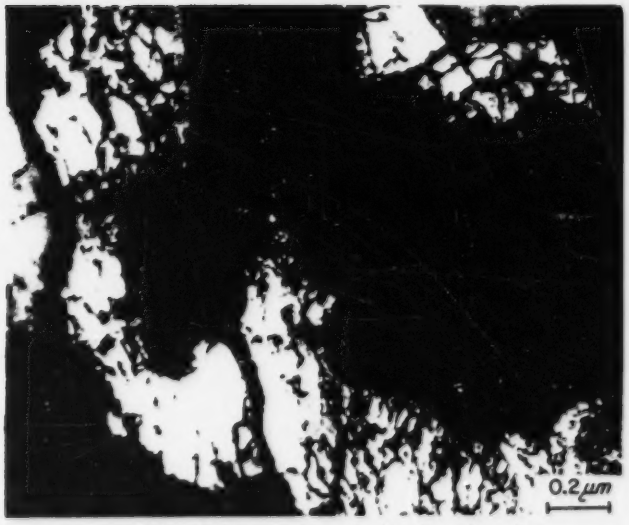

b) Alloy 5A: Acicular ferrite

Fig. 4.3: Transmission electron micrographs of as-rolled and air cooled alloys. (Thin foils of transverse sections)

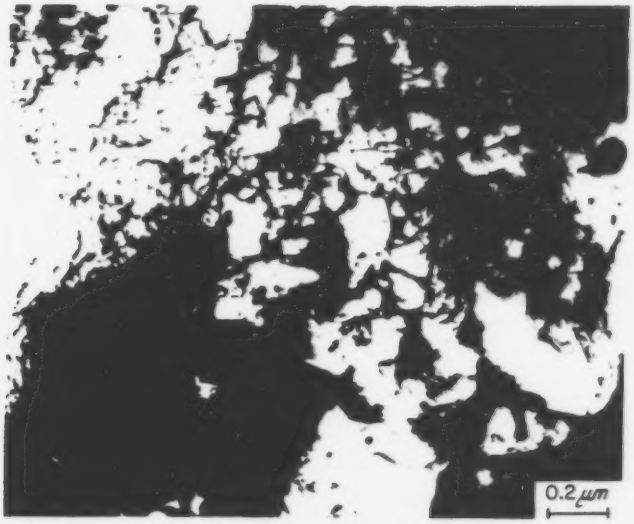

c) Alloy 7A: Polygonal ferrite

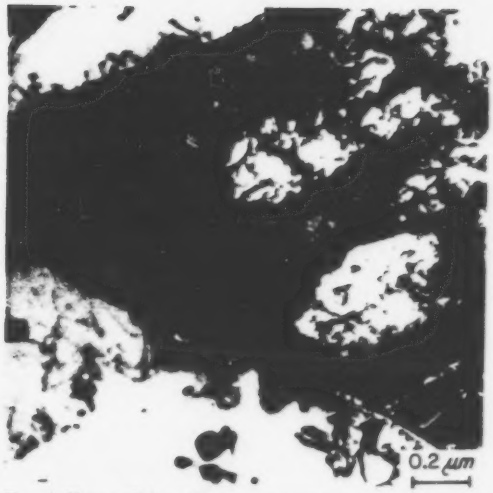

d) Alloy 5A: Degenerate pearlite island

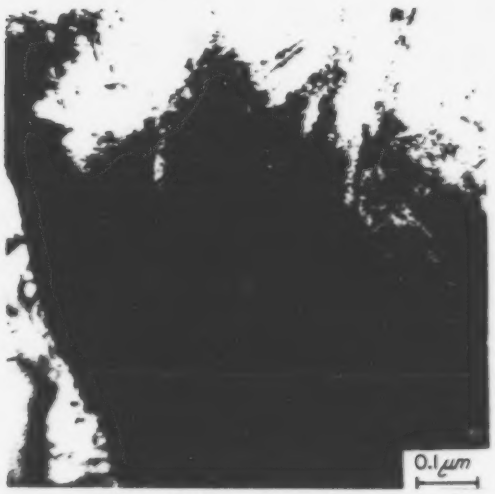

e) Alloy 7A: twinned martensite in MA islands

Fig. 4.3: continued.

hkl	d-spacing (Å) TiN	TiC	NbC
111	2,440	2,517	2,581
002	2,120	2,180	2,235
022	1,496	1,544	1,580
113	1,277	1,316	1,348
222	1,223	1,258	1,290
004	1,059	1,090	1,118
133	0,972	1,000	1,026

Table 4.1: Interplanar Spacings for Various Microalloy Carbides and Nitrides [23].

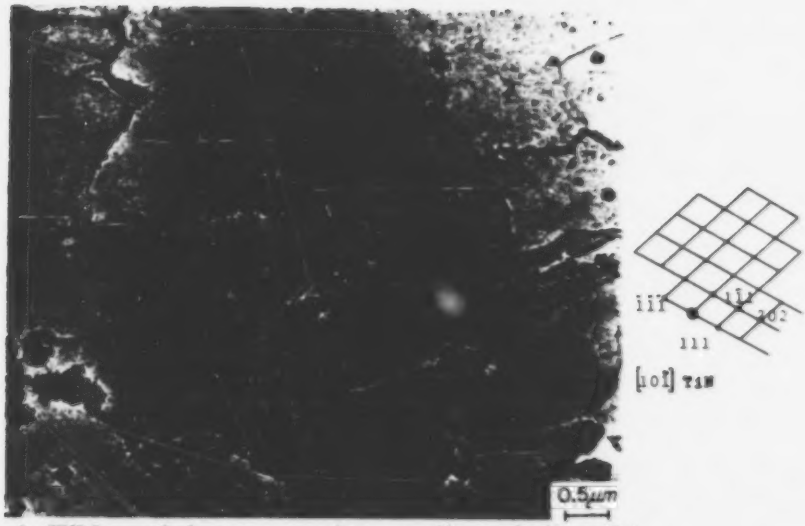

a) TiNprecipitate on carbon replica of alloy 5A

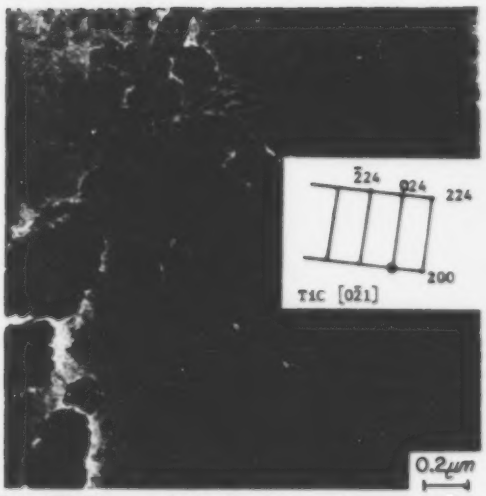

b) TiC precipitate on carbon replica of alloy 5A

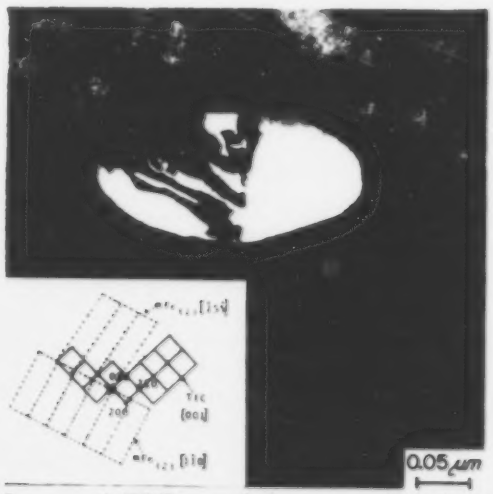

c) TiC precipitate on thin foil of alloy 5 A

Fig. 4.4: Identification of precipitates in as-rolled and air cooled alloys by SAD.

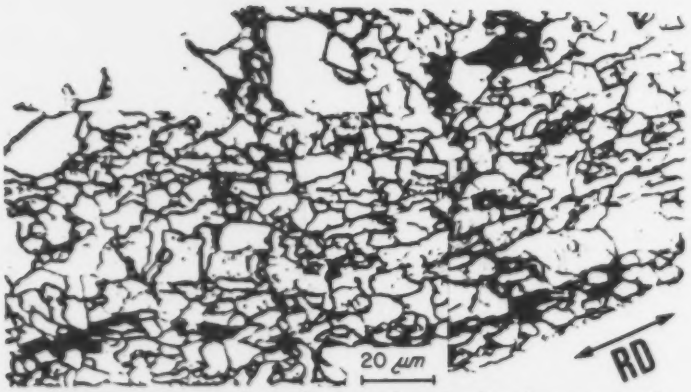

a) Three-dimensional view (optical microscopy)

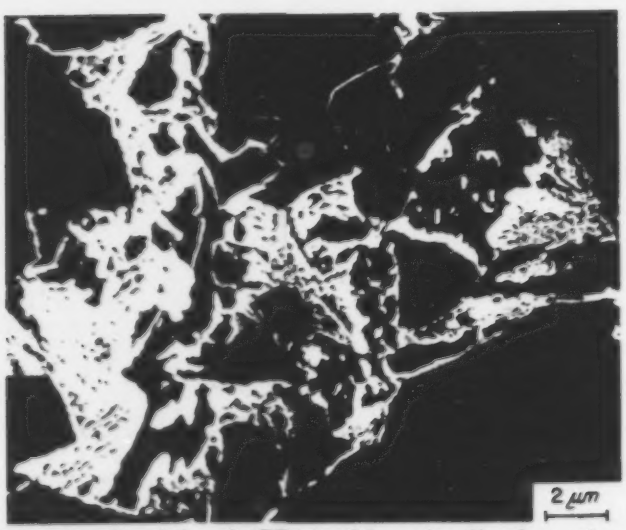

b) Pearlite island (SEM of longitudinal section)

Fig. 4.5: Microstructure of Alloy 0 in the as-rolled and air-cooled state.

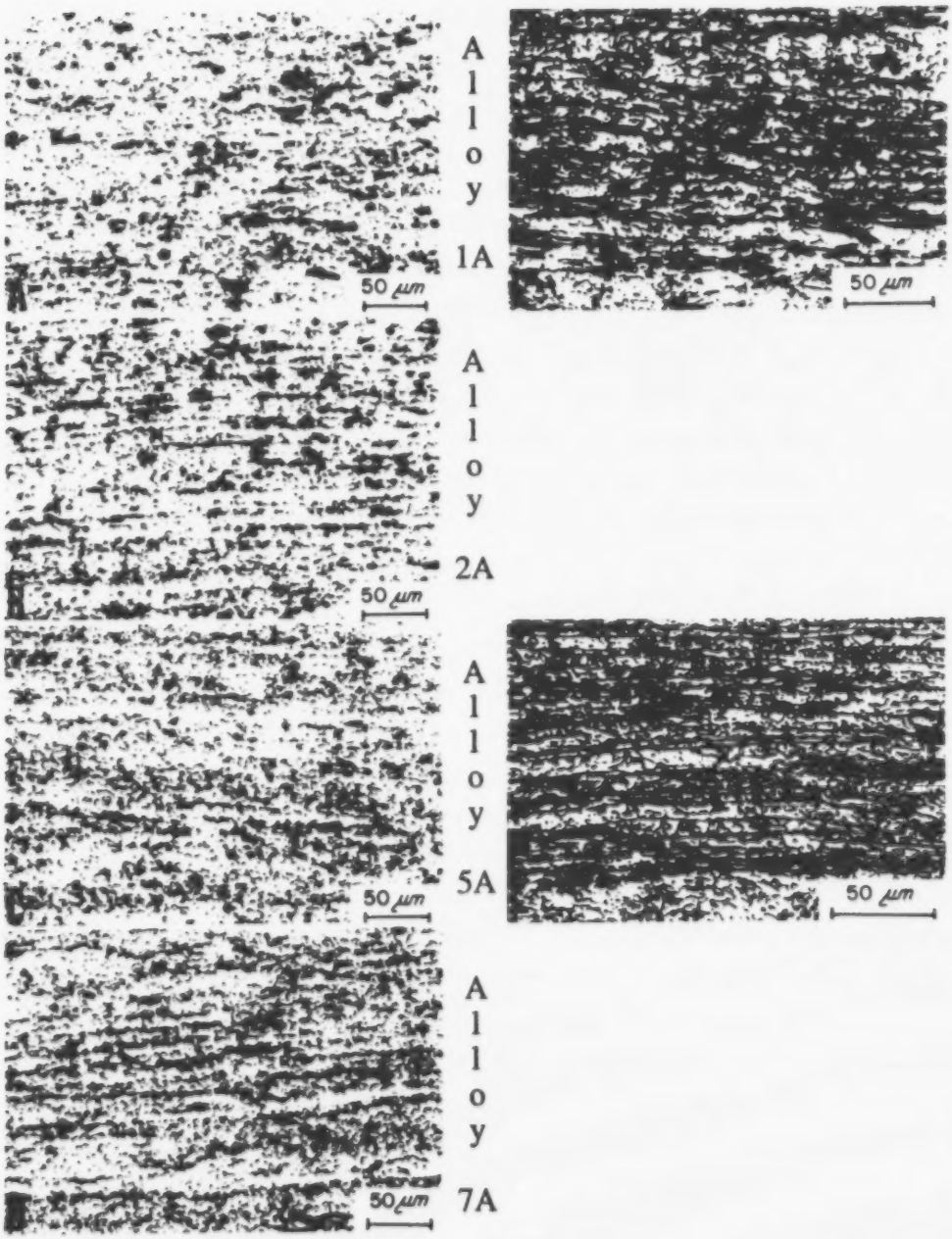

Fig. 4.6: Distribution of boron in as-rolled and air cooled alloys.

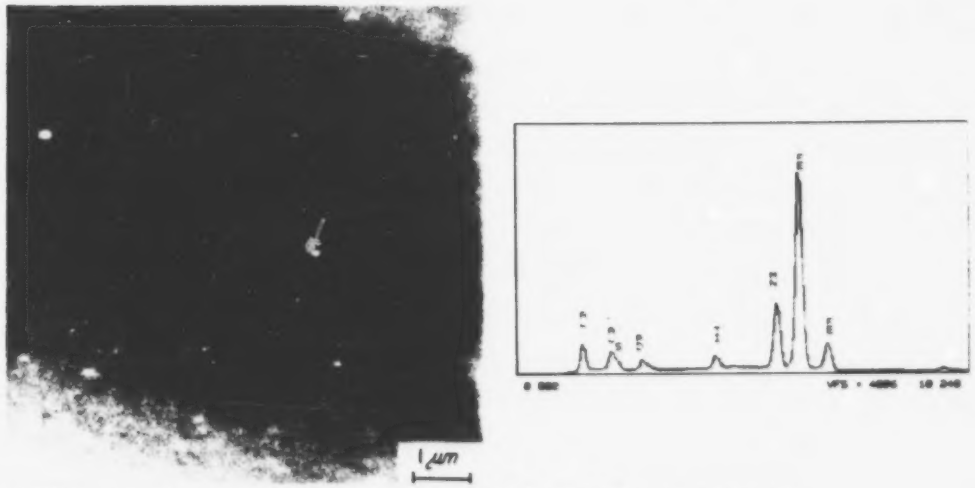

a) Elongated stringer type inclusion (Al-Mn-Ti containing)

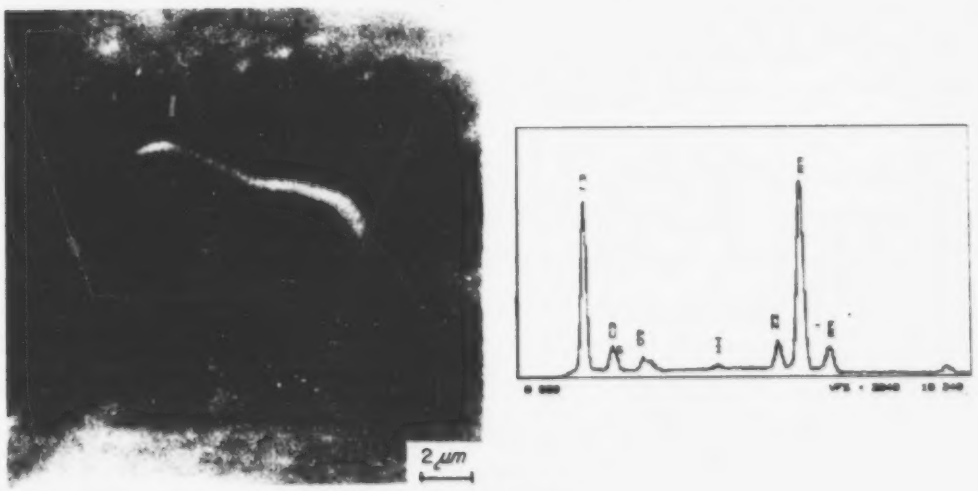

b) Rounded inclusion (Al-Mn containing)

Fig. 4.7: Analysis by EDAX (SEM) of the inclusions in Alloy 2A (as-rolled and air-cooled).

Alloy No.	Y.S. (0.2 %) (MPa)	T.S. (MPa)	El (%)	R.O.A. (%)	v.T.T. (55J) (°C)*	VHN10	Volume Fraction of MA (%)
0	409	473	37	-	<-100	156	-
1 A	426	600	28	63	<-100	205	9.4
2 A	416	584	32.8	74	<-100	186	10.5
5 A	455	611	26.5	55	-95	206	9.5
7 A	391	600	33.2	64	<-100	179	8.2

*Longitudinal specimens

Table 4.2: Mechanical Properties of the Experimental Steels in the As-rolled and Air-cooled Condition.

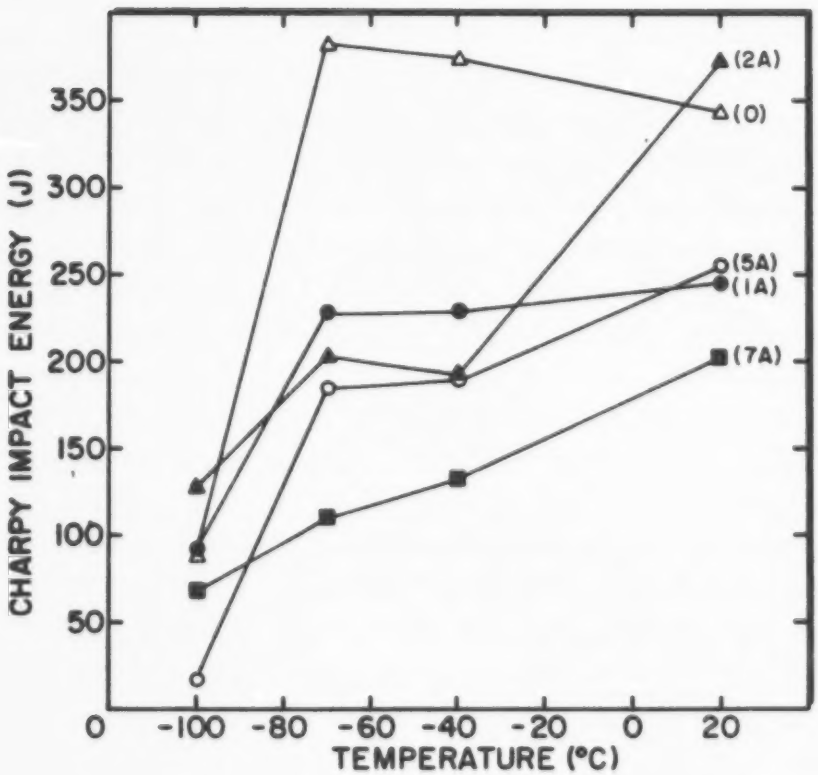

Fig. 4.8 a) Impact properties of as-rolled and air cooled experimental steels.

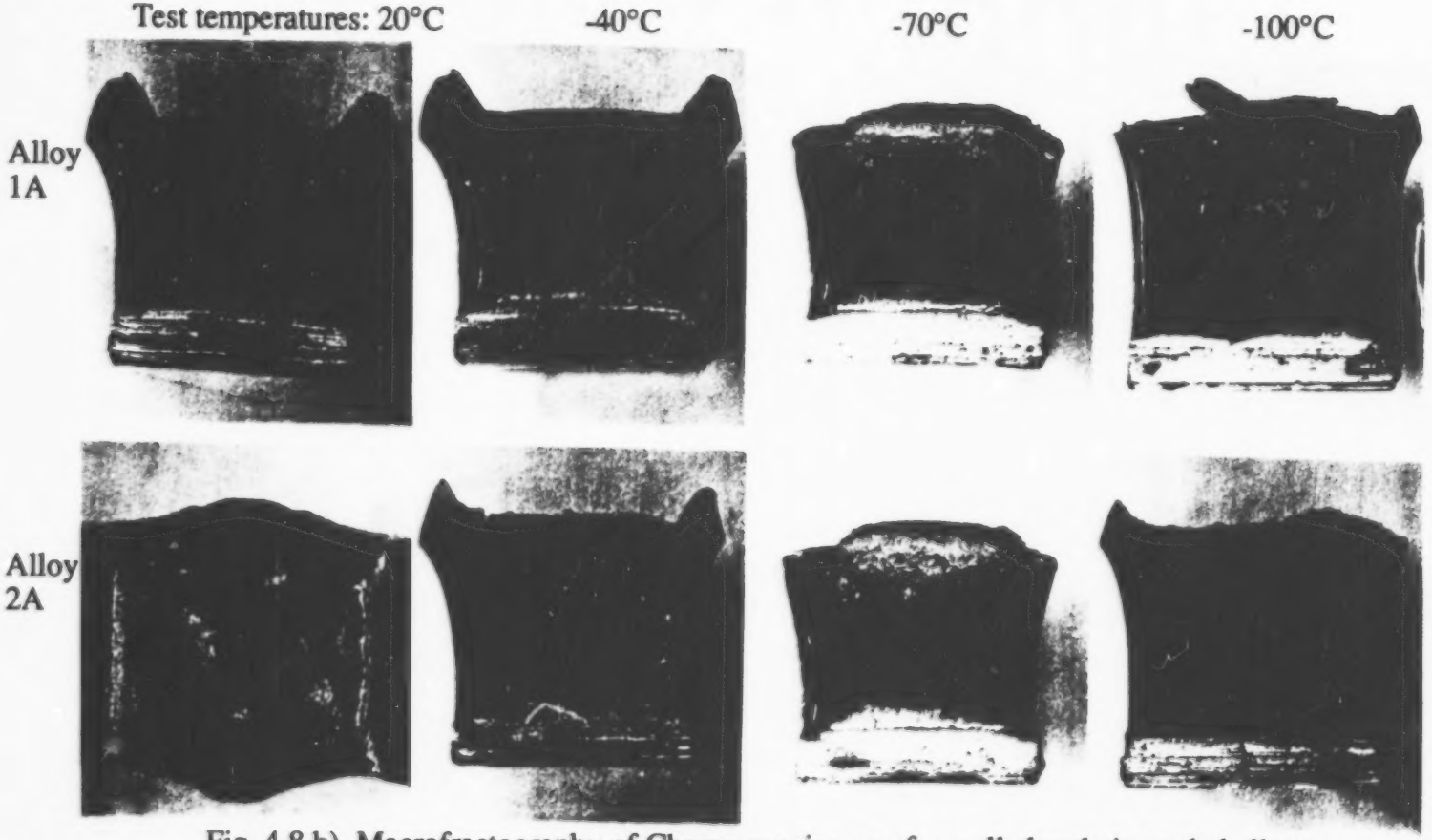

Fig. 4.8 b) Macrofractography of Charpy specimens of as-rolled and air-cooled alloys.

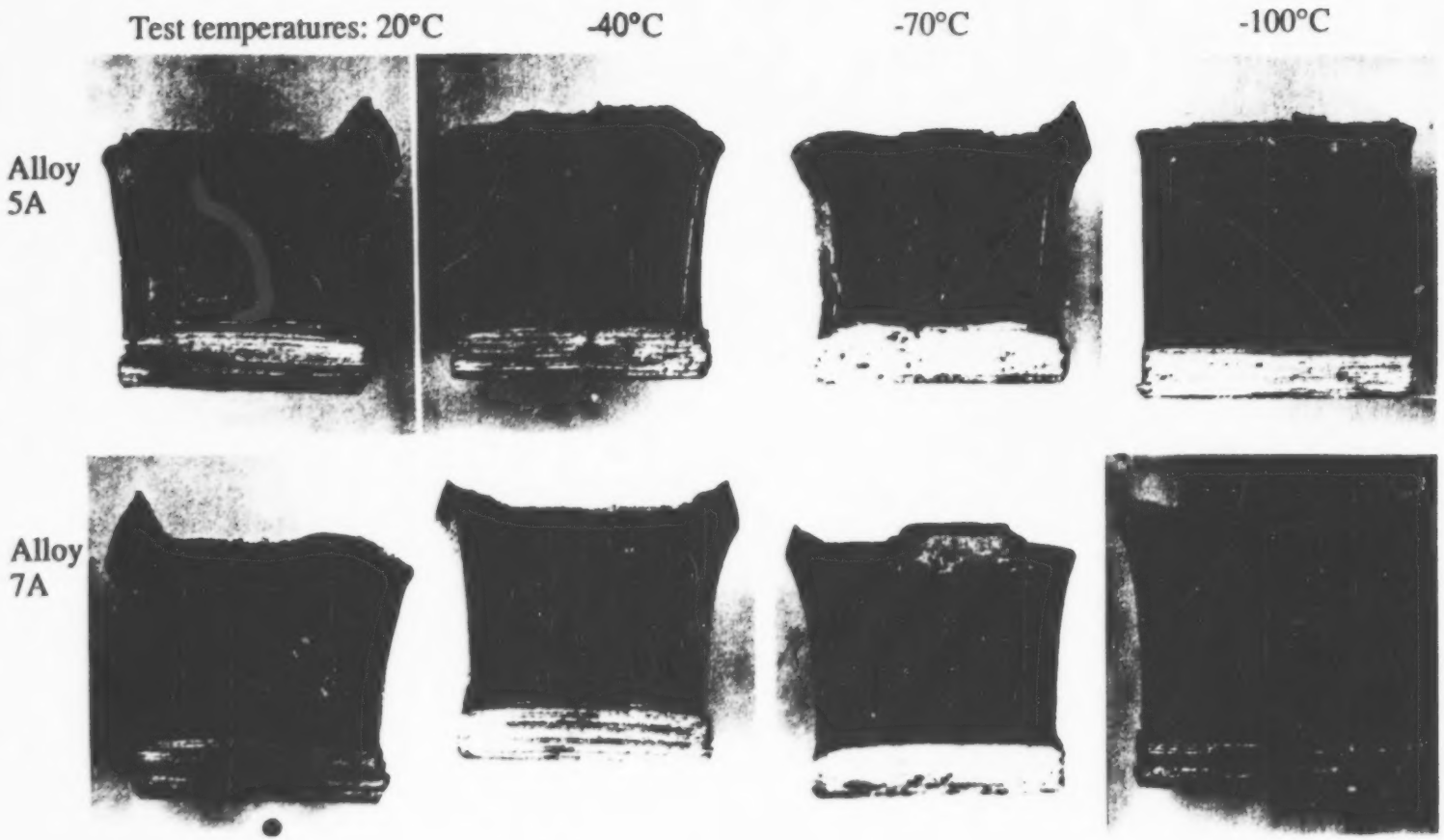

Fig. 4.8 b) continued.

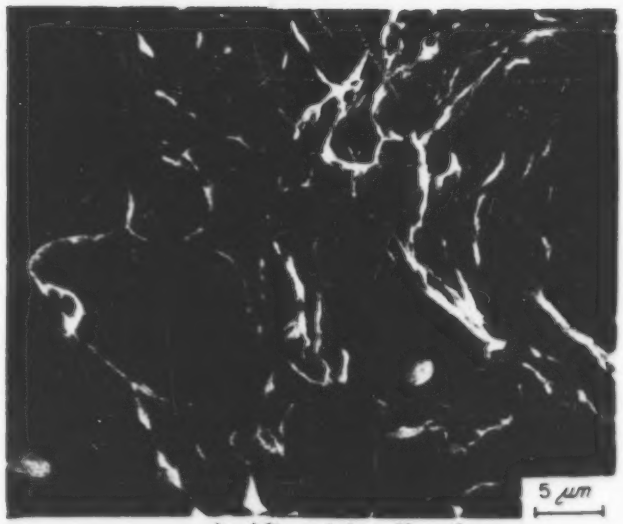

a) Alloy 1A: dimples

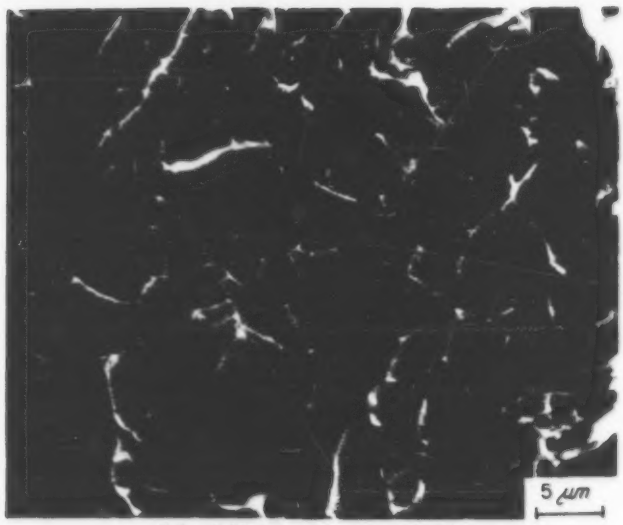

b) Alloy 7A: quasi-cleavage

Fig. 4.9: Fractography of Charpy specimens of as-rolled and air-cooled alloys. (test temperature -100°C)

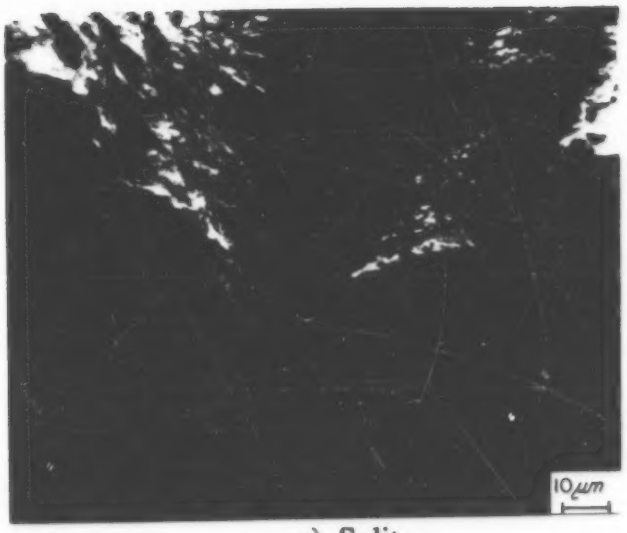

a) Split

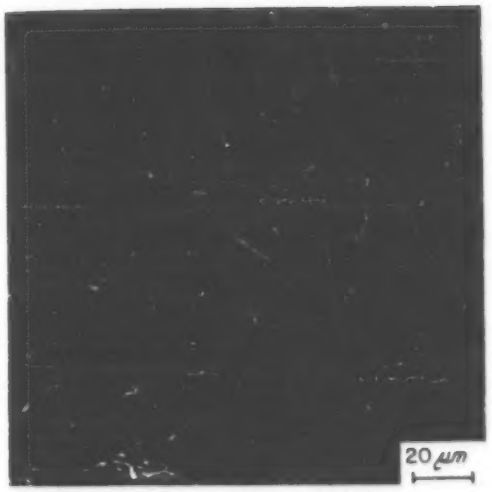

b) Tearing on split wall (1)
Dimples on fracture surface (2)

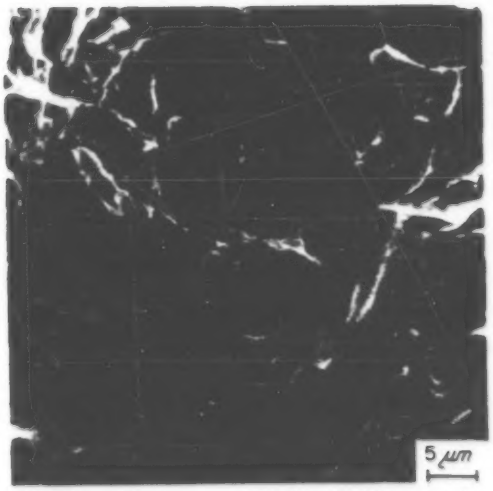

c) Dimples at root of a shallow split

Fig. 4.10: Fractography of Charpy specimen of alloy 2A.
(test temperature -100°C)

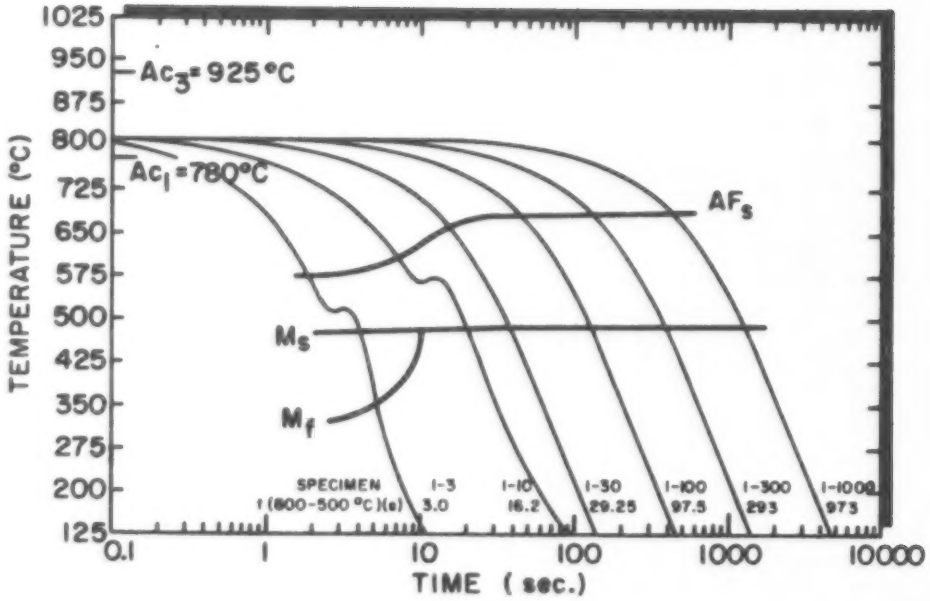

Fig. 4.11: CCT diagram for Alloy 1A.

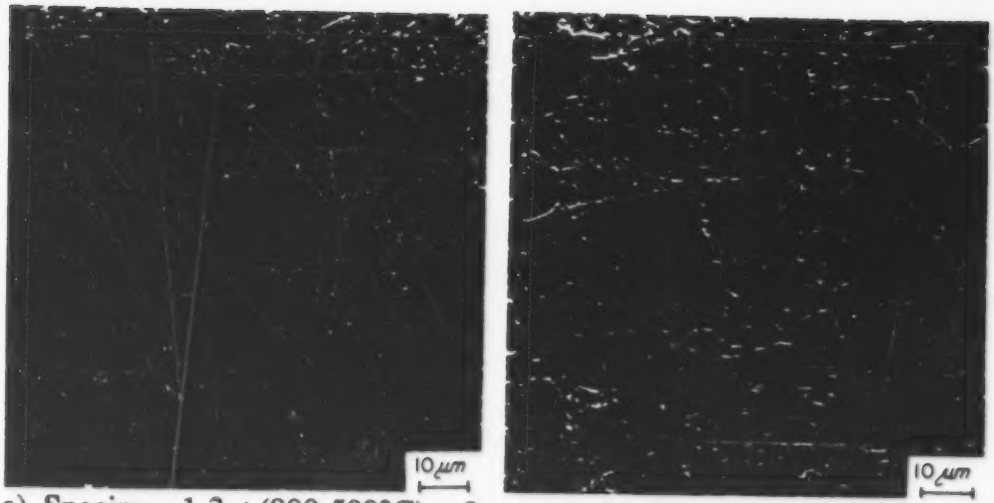

a) Specimen 1-3: t (800-500°C) = 3 s

b) Specimen 1-30:
t (800-500°C) = 29,25 s

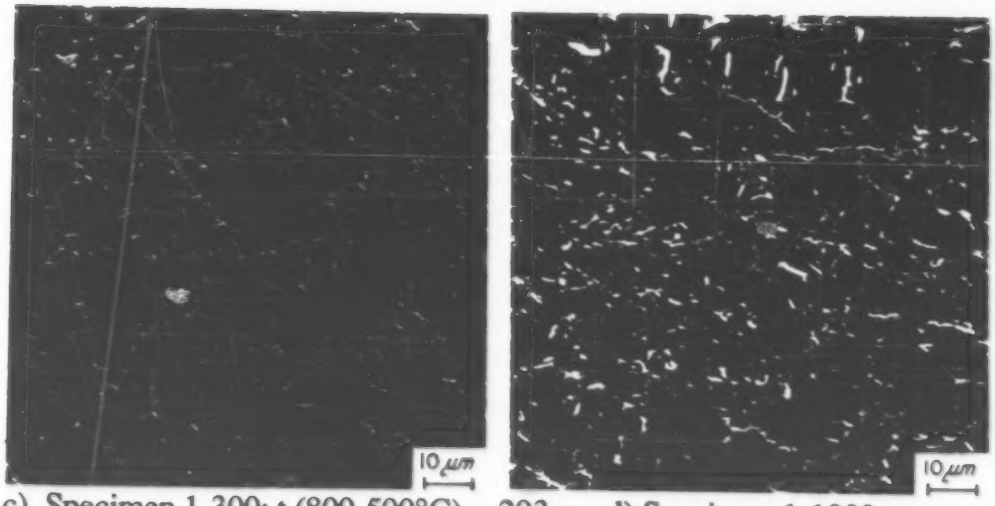

c) Specimen 1-300: t (800-500°C) = 293 s

d) Specimen 1-1000:
t (800-500°C) = 973 s

Fig. 4.12: Effect of cooling rate on the microstructure of alloy 1A.

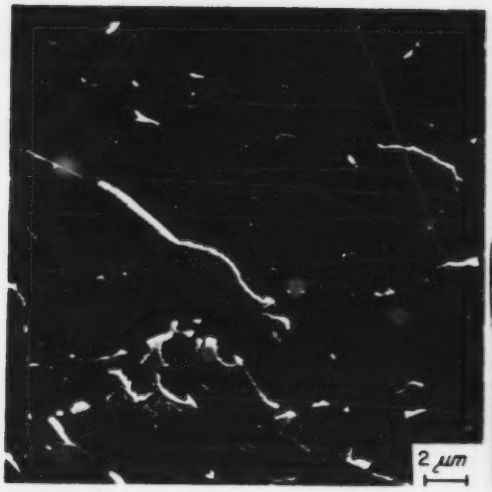

a) Specimen 1-300: bainite islands in acicular ferrite matrix

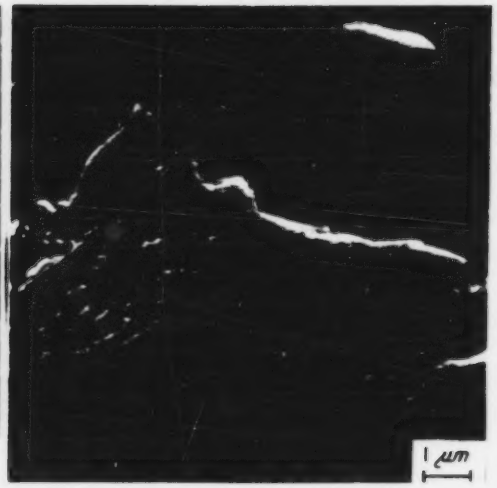

b) Specimen 1-1000: degenerated pearlite islands

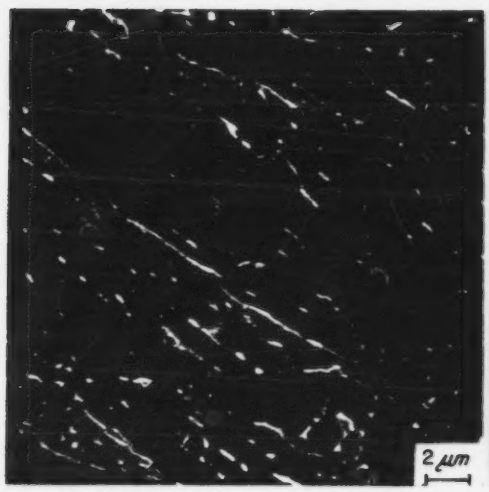

c) Specimen 1-3: mixture of extra-low carbon martensite and lath acicular ferrite

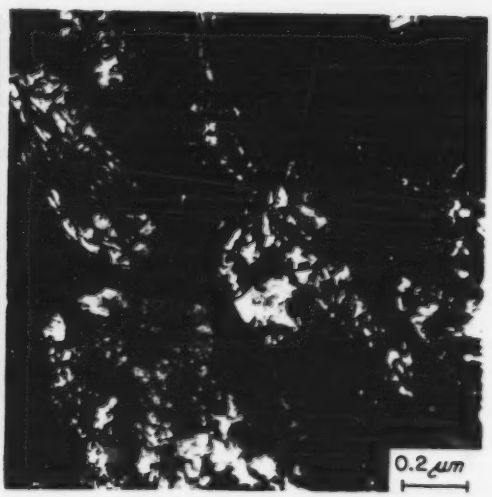

d) Specimen 1-3: martensite laths (TEM of thin foil)

Fig. 4.13: Microstructural features of dilatometry specimens of alloy 1A.

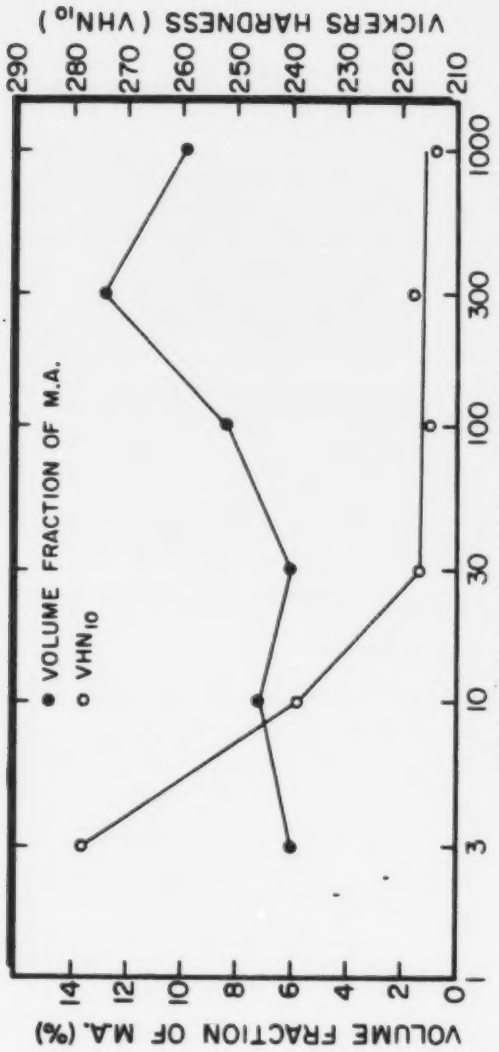

Fig. 4.14: Variation in volume fraction of MA and Vickers hardness of Alloy 1A as a function of the cooling rate.

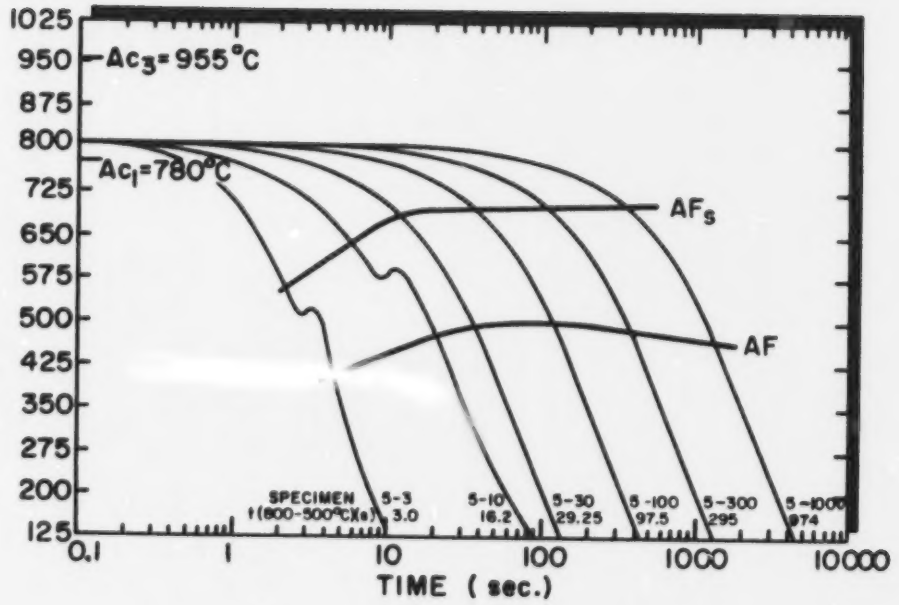

Fig. 4.15: CCT diagram for Alloy 5A.

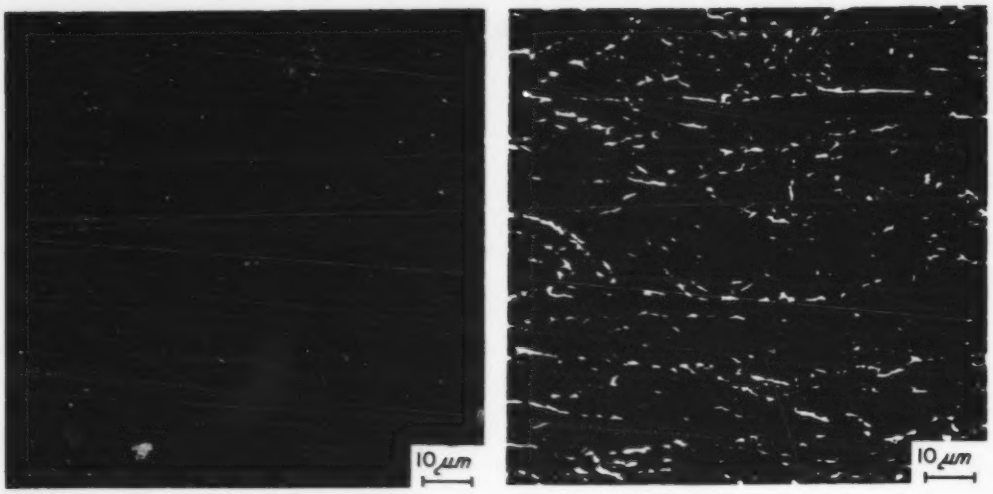

a) Specimen 5-3: t (800-500°C) = 3 s

b) Specimen 5-30: t (800-500°C) = 29,25 s

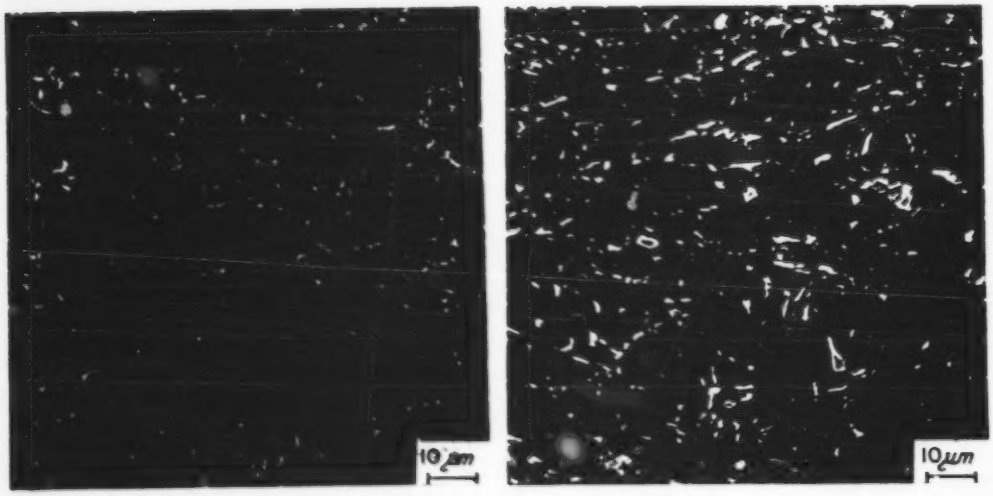

c) Specimen 5-300: t (800-500°C) = 295 s

d) Specimen 5-1000: t (800-500°C) = 974 s

Fig. 4.16: Effect of cooling rate on the microstructure of alloy 5A.

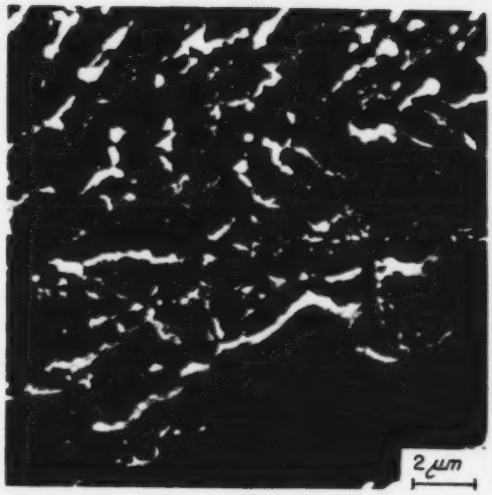

a) Specimen 5-3: acicular ferrite with fine MA islands

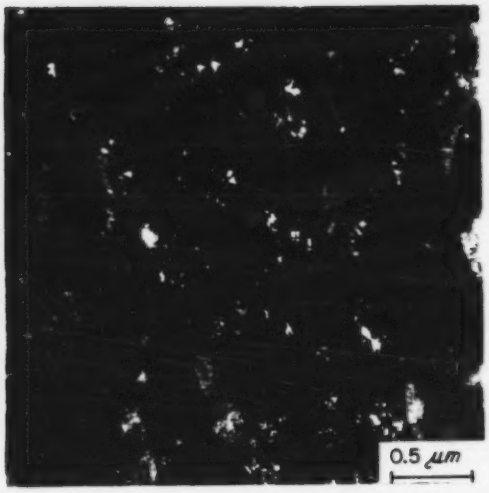

b) Specimen 5-3: Fine grained, high dislocation density acicular ferrite (TEM of thin foil)

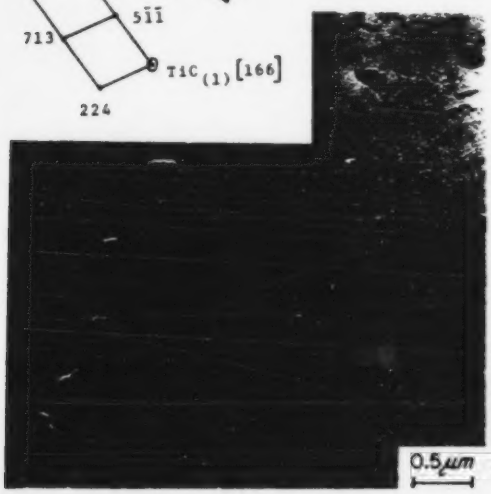

c) Specimen 5-1000: Ti (C,N) precipitates (TEM of carbon replica)

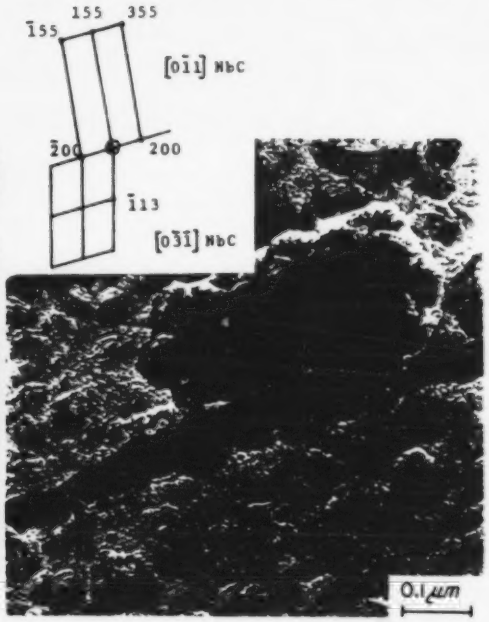

d) Specimen 5-300: NbC precipitate (TEM of carbon replica)

Fig. 4.17: Microstructural features of dilatometry specimens of alloy 5A.

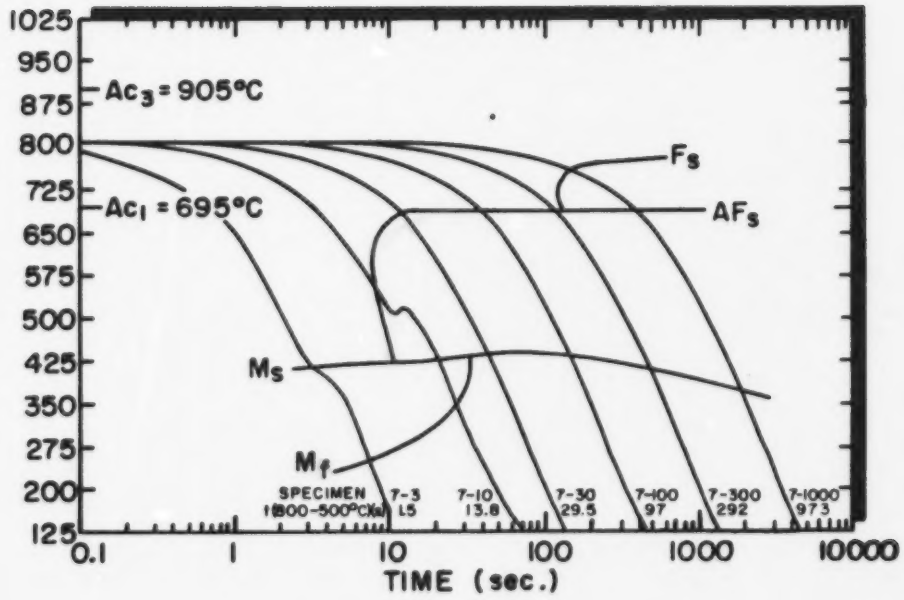

Fig. 4.18: CCT diagram for Alloy 7A.

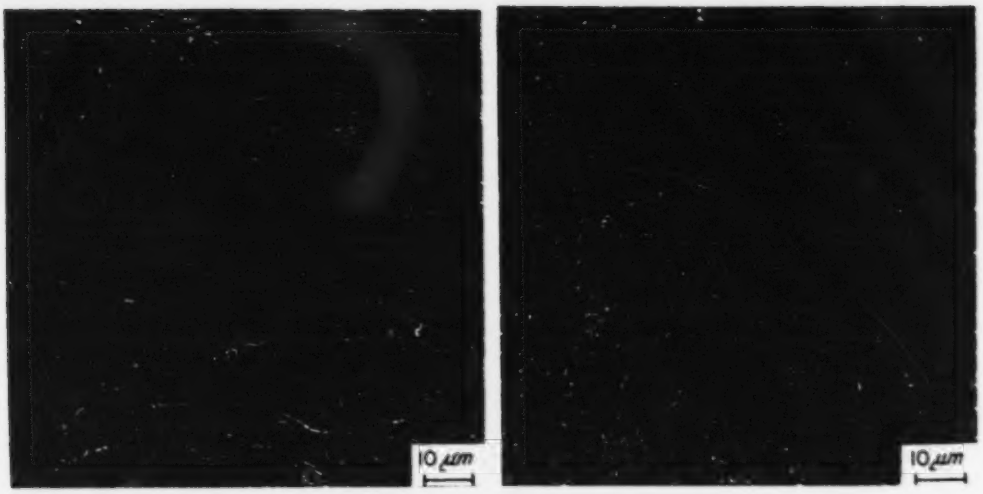

a) Specimen 7-3: t (800-500°C) = 1,5 s

b) Specimen 7-30: t (800-500°C) = 29,5 s

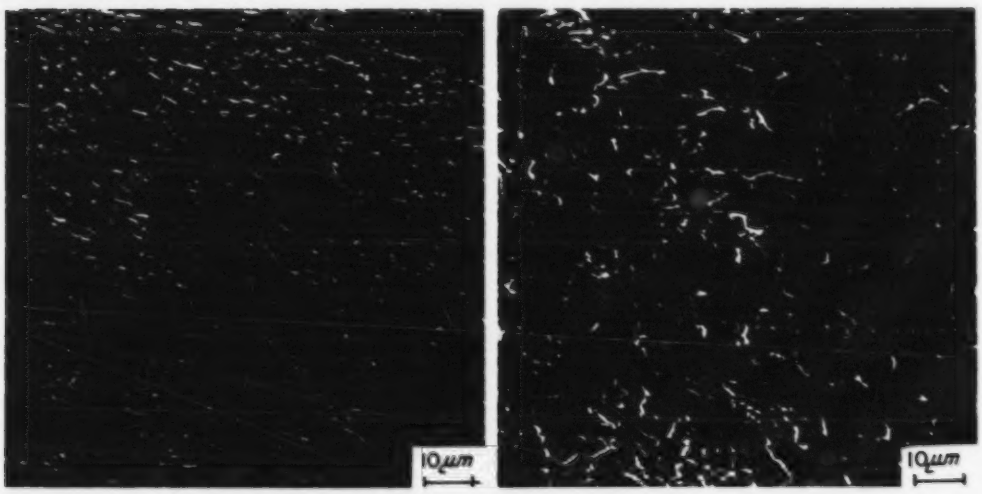

c) Specimen 7-300: t (800-500°C) = 292 s

d) Specimen 7-1000: t (800-500°C) = 973 s

Fig. 4.19: Effect of cooling rate on the microstructure of alloy 7A.

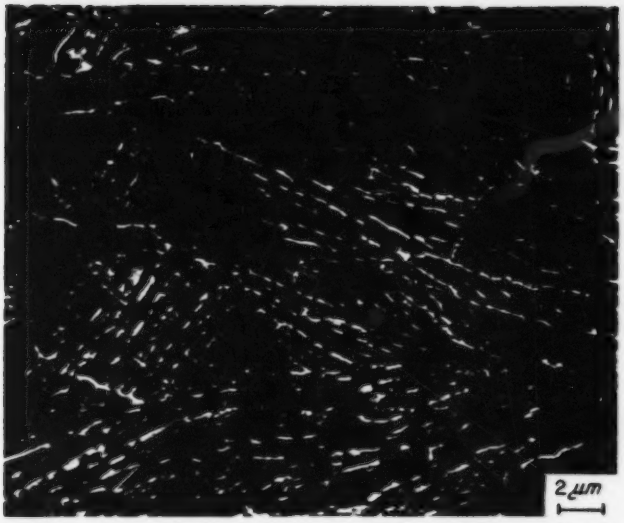

a) Specimen 7-3: lath martensite with small MA islands on lath boundaries

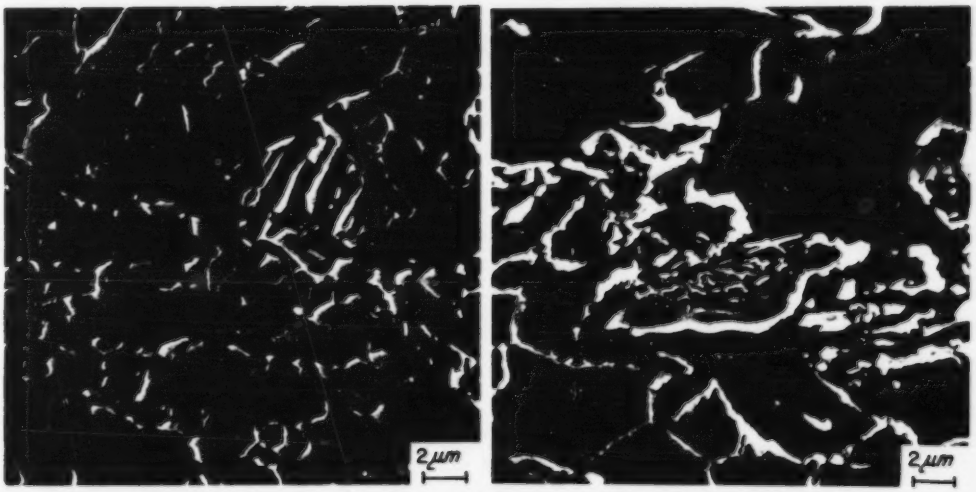

b) Specimen 7-30: acicular ferrite with MA

c) Specimen 7-1000: polygonal ferrite islands on sub boundaries grains with degenerated pearlite and MA islands

Fig. 4.20: Microstructural features of dilatometry specimens of alloy 7A.

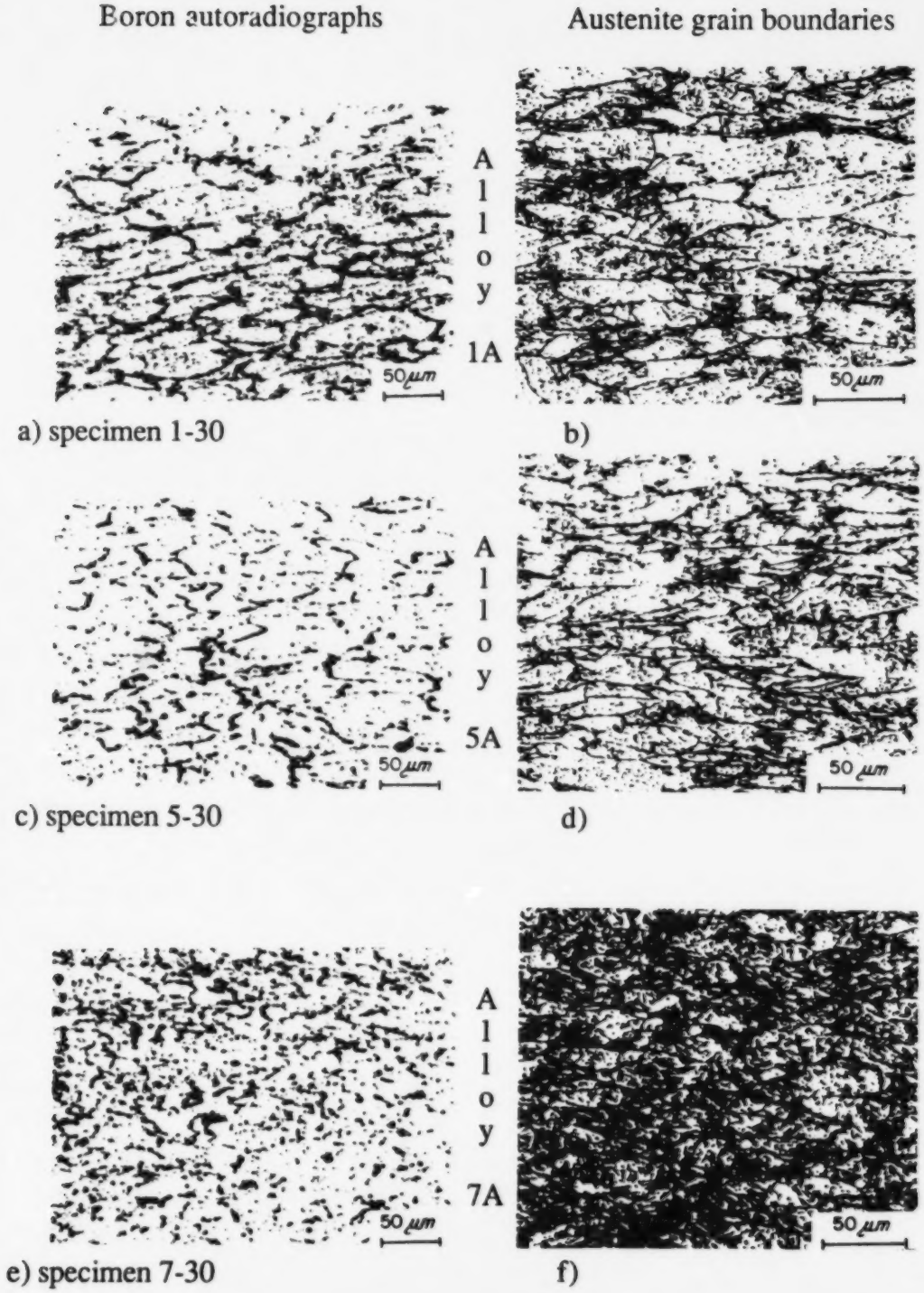

Fig. 4.21: Boron distribution in dilatometry specimens of alloys 1A, 5A and 7A (t (800-500°C) = 30 s).

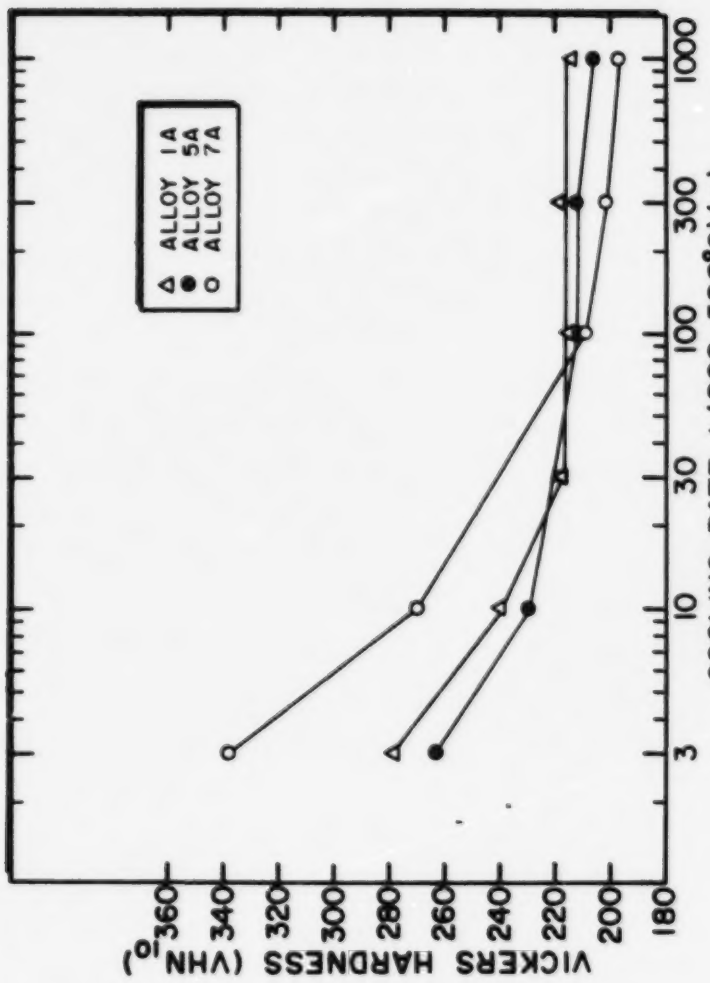

Fig.4.22: Variation of Vickers hardness of alloys 1A, 5A and 7A as a function of the cooling rate.

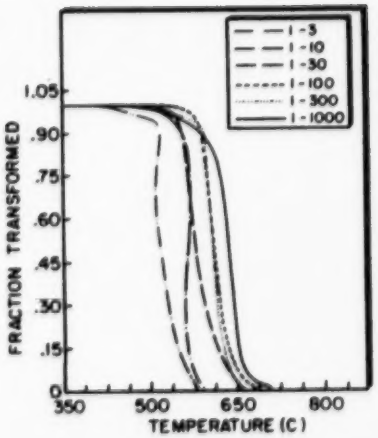

Fig 4.23: Alloy 1A

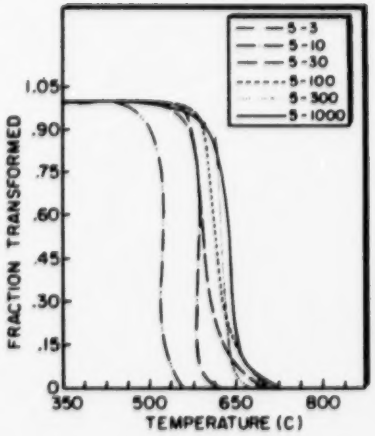

Fig. 4.24: Alloy 5A

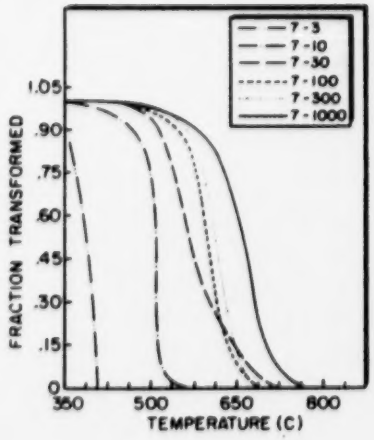

Fig. 4.25: Alloy 7A

Fraction transformed vs temperature plots at various cooling rates.

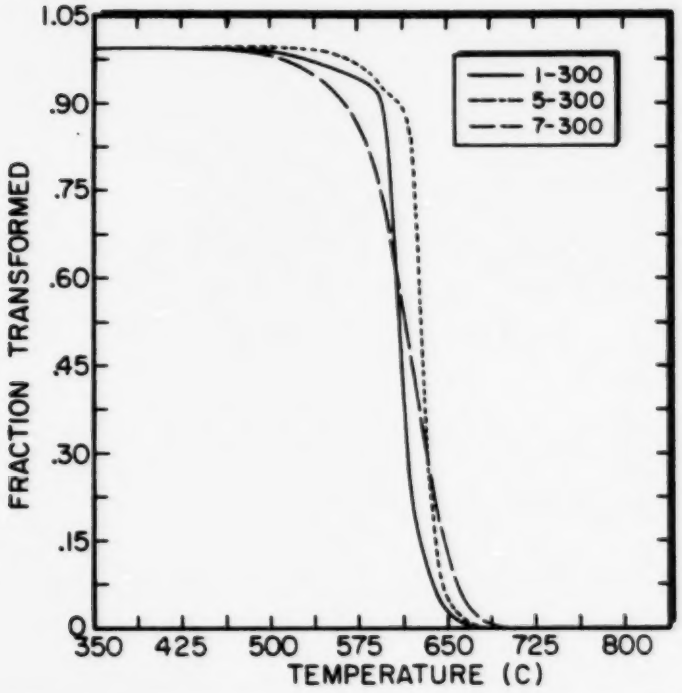

Fig 4.26: Fraction transformed vs temperature plots for specimens 1-300 (Alloy 1A), 5-300 (Alloy 5A) and 7-300 (Alloy 7A) with a cooling rate of 1°C s^{-1}.
(t (800-500°C) = 300 s)

MATERIAL	MICROSTRUCTURE	VHN10
Alloy 1A*	Fine grained polygonal ferrite + acicular ferrite (fig. 4.1a)	205
Specimen 1-300	Acicular ferrite (fig. 4.12c)	218
Alloy 5A*	Fine grained polygonal ferrite +acicular ferrite (fig. 4.1c)	206
Specimen 5-300	Acicular ferrite (fig. 4.16c)	212
Alloy 7A*	Polygonal ferrite + small amount of acicular ferrite (fig. 4.1d)	179
Specimen 7-300	Acicular ferrite (fig. 4.19c)	201

*As-rolled and air-cooled plate

Table 4.3: Comparison of As-rolled and Air-cooled Plates with CCT Diagram Specimens.

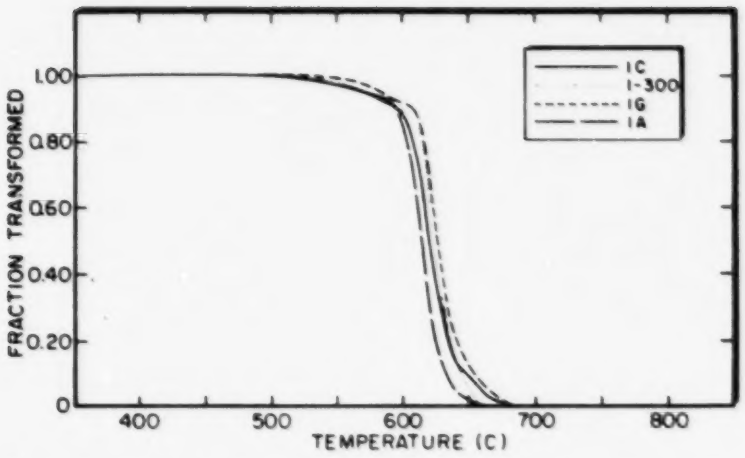

Fig 4.27: Effect of deformation schedule on the transformation behaviour of Alloy 1A.

Specimen No.	Temperature for 50% transformation (°C)	VHN10
1-300	624	218
1 A	616	-
1 C	621	193
1 G	627	206

Table 4.4: Temperature for 50% Transformation and Vickers Hardness for Various dilatometer deformation schedules.

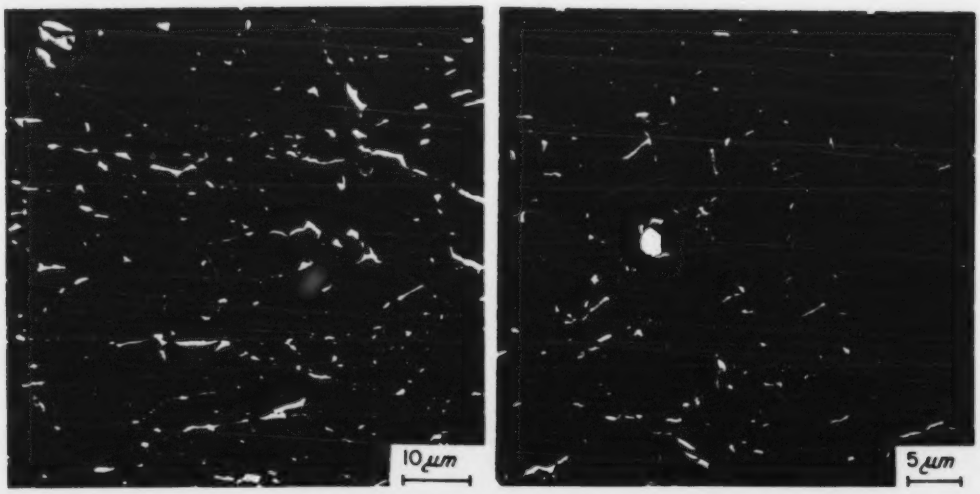

a) Specimen 1A (25% def. at 1050°C + at 25% def. at 825°C)

b) Specimen 1G (25% def. 825°C + 25% def. at 825°C)

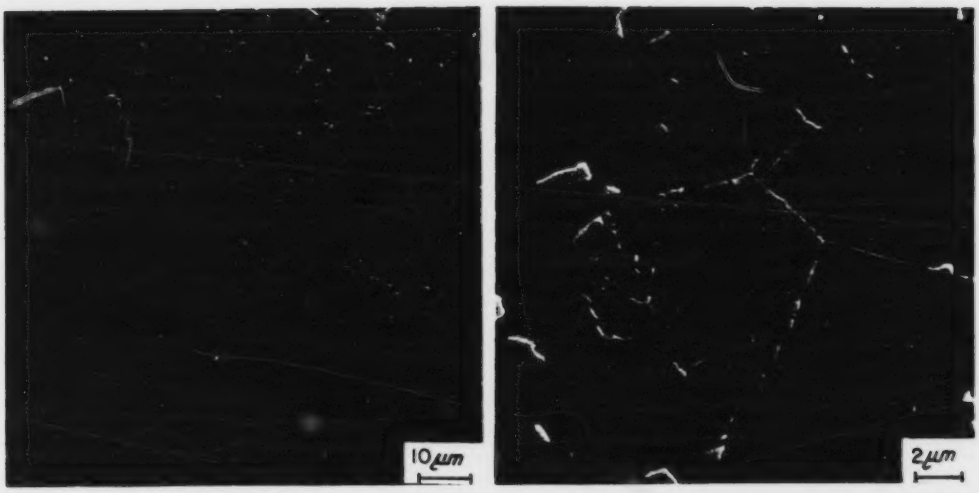

c) Specimen 1C (25% def. at 1050°C + 25% def. at 1050°C)

d) Detail of specimen 1C showing a large bainite island

Fig. 4.28: Effect of deformation schedule on the microstructure of dilatometry specimens of Alloy 1A.

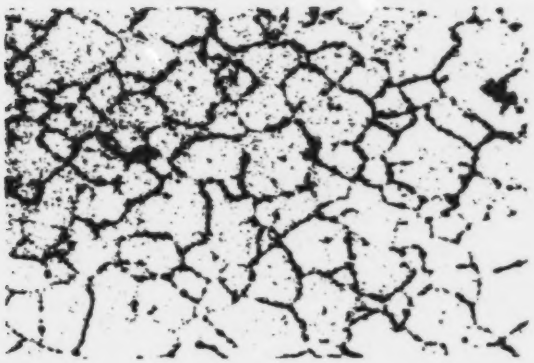

a) Undeformed region of dilatometry specimen

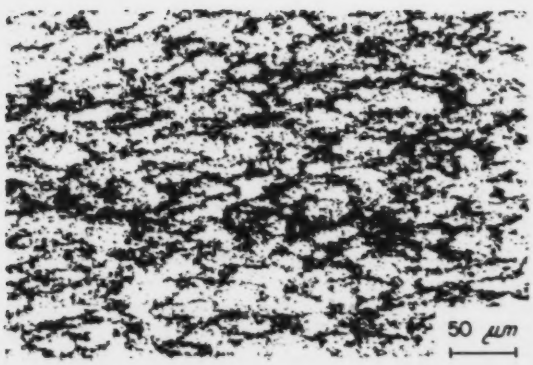

b) Deformed region of dilatometry specimen

Fig. 4.29: Boron autoradiography of dilatometry specimen 1A.

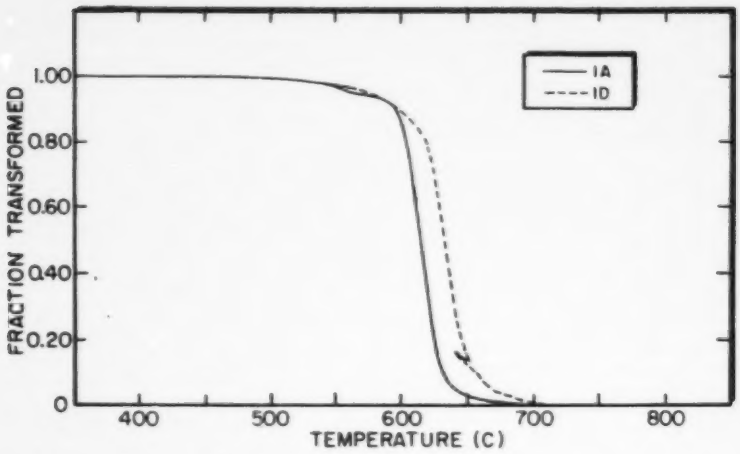

Figure 4.30: Effects of holding time prior to cooling on the transformation behaviour of Alloy 1A.

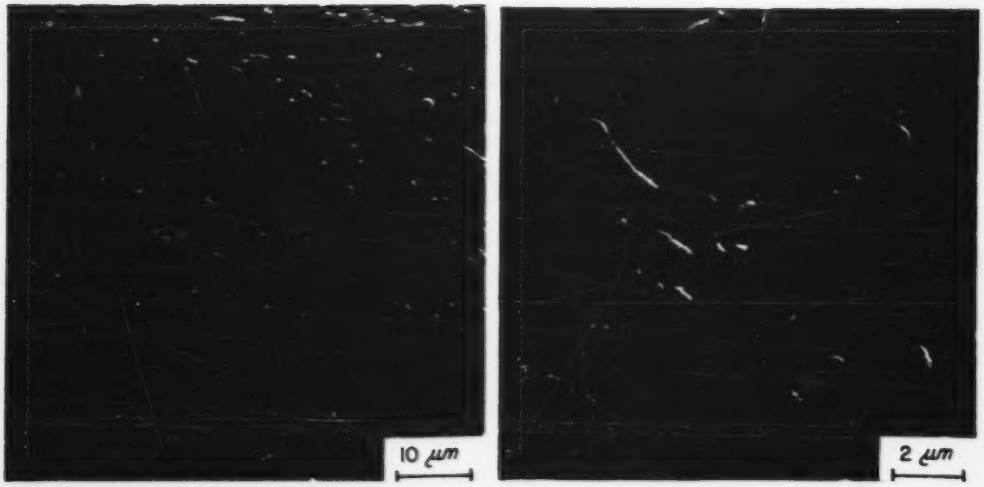

a) General view of specimen 1D

b) Detail of specimen 1D showing fine acicular ferrite grains and MA island on subboundaries

Fig. 4.31: Microstructure of dilatometry specimen 1D.

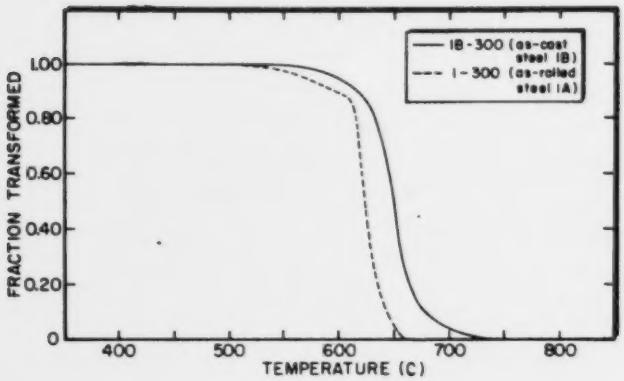

Figure 4.32: Effects of nature of starting material (as-cast vs as-rolled) on the transformation behaviour.

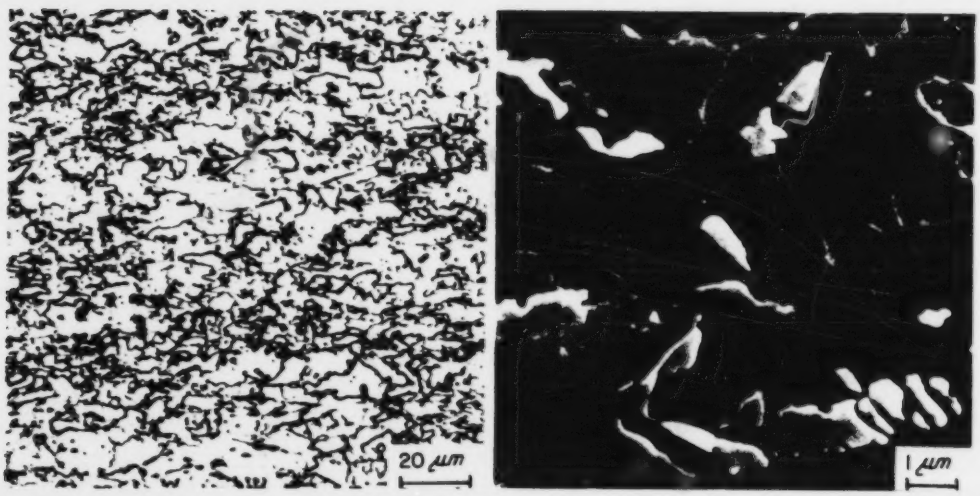

a) Fine grained polygonal ferrite with small amount of acicular ferrite

b) Small MA islands in highly substructured ferrite

Fig. 4.33: Microstructure of dilatometry specimen 1B-300.

Specimen No.	Starting Material	Temperature for 50% transformation (°C)	VHN10
1-300	As-rolled plate of Alloy 1A	625	218
1B-300	As-cast ingot of Alloy 1B	650	188

Table 4.5: Effect of Nature of Starting Material (As-cast vs As-rolled) on Hardenability.

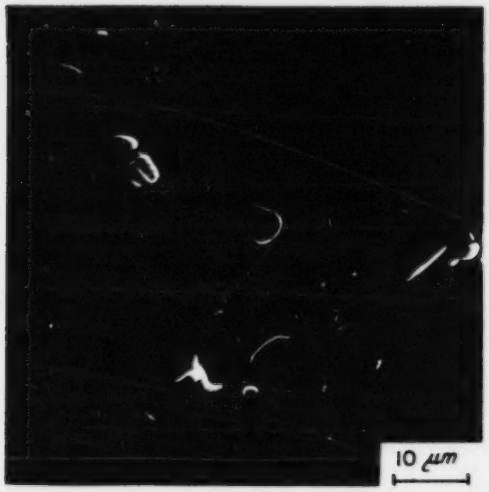

a) Group of inclusions (SEM micrograph)

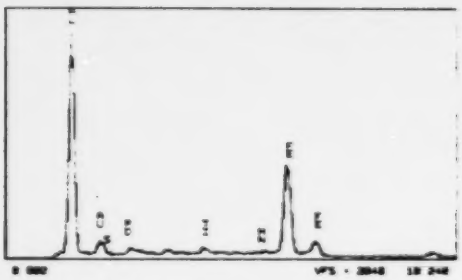

b) Al-rich inclusion (1) (EDAX spectrum)

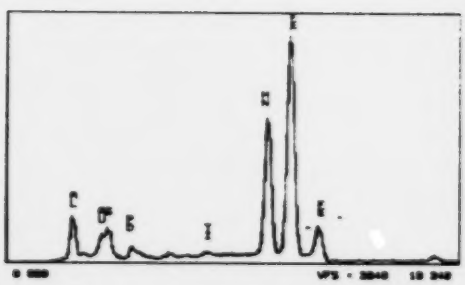

c) Mn-rich inclusion (2) (EDAX spectrum)

d) Mixed inclusion

Fig. 4.34: EDAX analysis of inclusions in dilatometry specimen 1B-300. (Machined from as-cast ingot of alloy 1B)

a) Al-rich inclusion

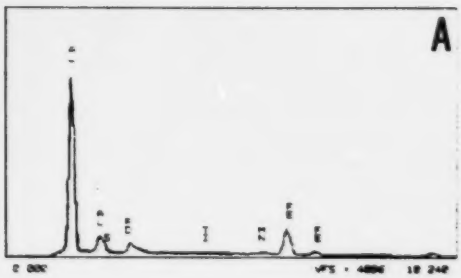

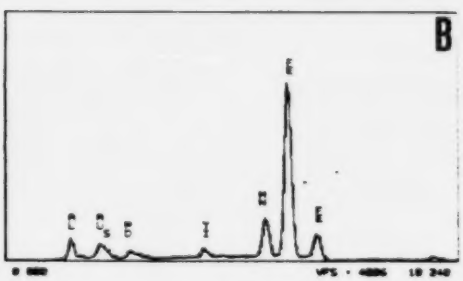

b) Inclusion containing Al, Ti and Mn
(Same type as fig. 4.34 d))

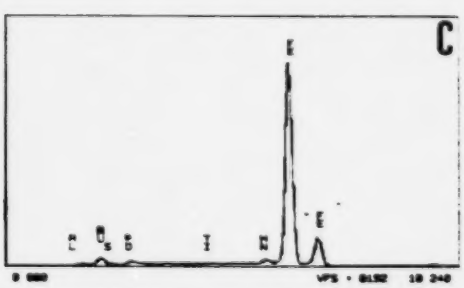

c) Spectrum from matrix

Fig. 4.35: EDAX analysis of inclusions in dilatometry specimen 1-300.
(Machined from as-rolled plate of alloy 1A)

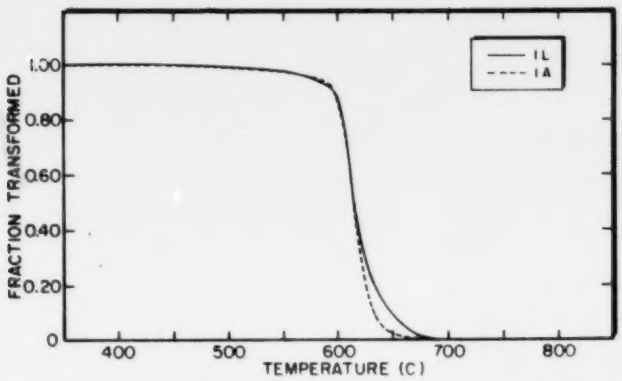

a) Effect of austenitizing practice on transformation kinetics

b) Microstructure of dilatometry specimen 1L

Fig. 4.36: Effect of austenitizing practice on the transformation behaviour of alloy 1A.

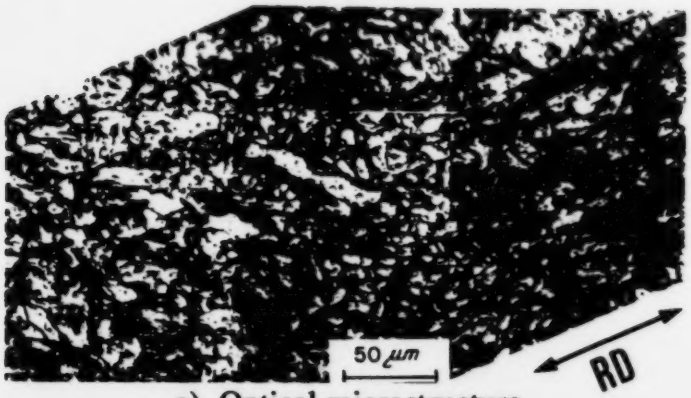

a) Optical microstructure

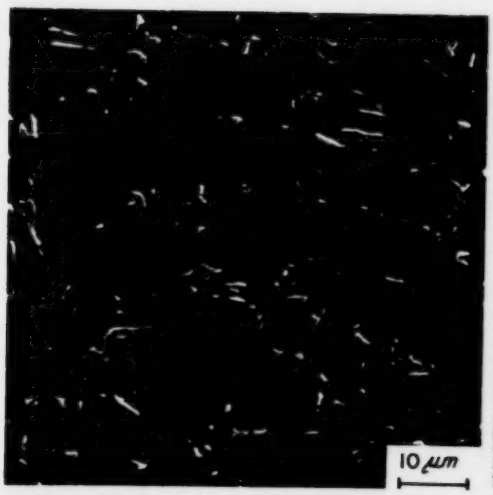

b) Detail showing acicular ferrite with MA islands

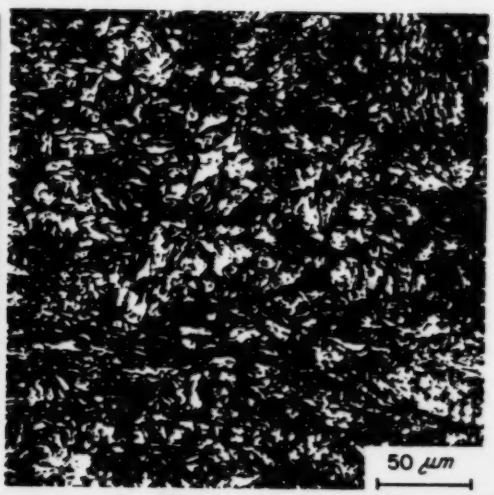

c) Transverse section etched to reveal the austenite boundaries

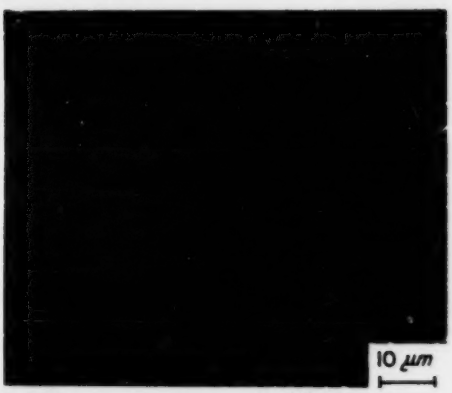

d) Microstructure of dilatometry specimen 1-100

Fig. 4.37: Microstructure of 8 mm thick plate of alloy 1A.

Plate Thickness (nm)	Alloy No.	Y.S. (0,2%) MPa	T.S. MPa	El (%)	ROA (%)	v.T.T. (55J) (°C) *	VHN10
13	1 A	426	600	28	63	<-100	205
8	1 A	478	622	23.7	77	-80	204

*Longitudinal specimens

Table 4.6: Mechanical Properties of Alloy 1A (13 and 8 mm Thick Plates).

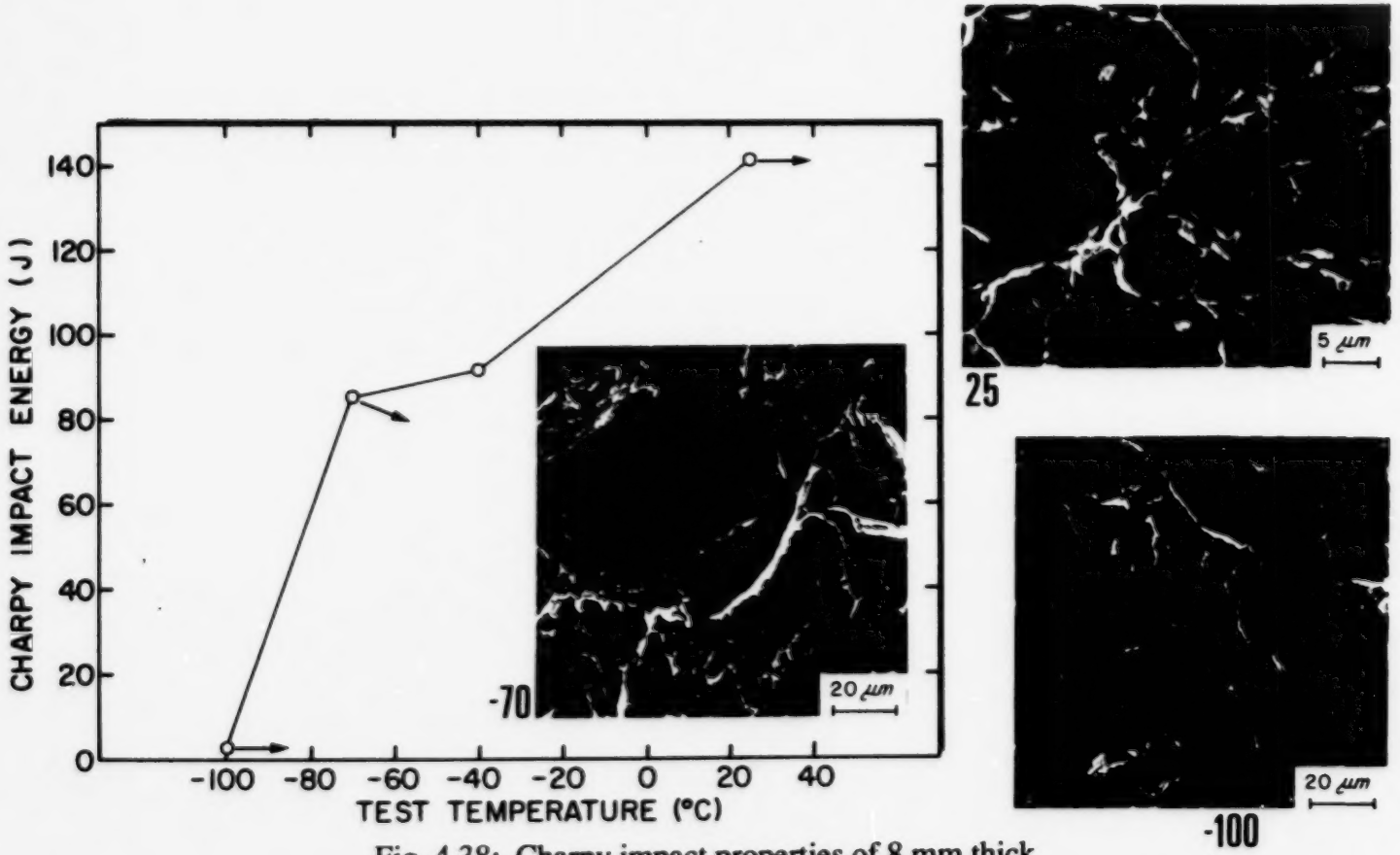

Fig. 4.38: Charpy impact properties of 8 mm thick plate of alloy 1A (longitudinal, half size Charpy specimens).

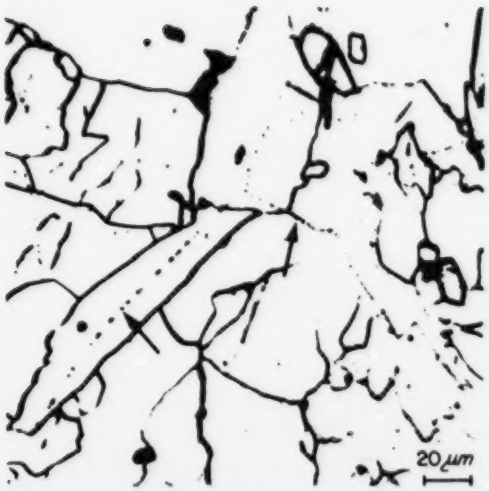

a) Large ferrite grains with austenite grains boundaries outlined by precipitates (Nital etch)

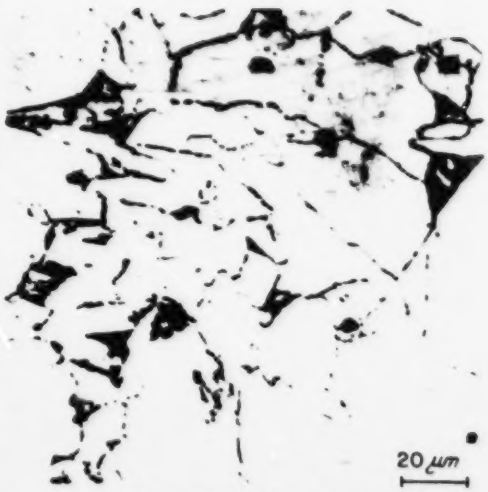

b) Pearlite islands and ferrite grains outlined by precipitates (Boiling saturated aqueous picric acid etch)

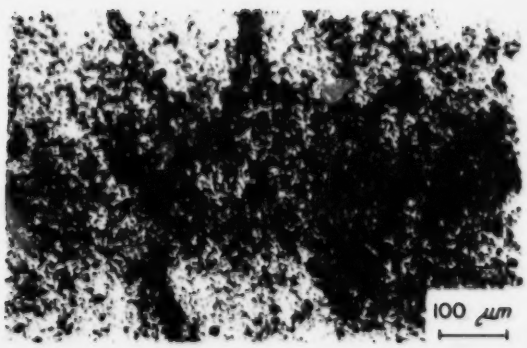

c) Autoradiograph showing boron distribution

Fig. 4.39: Microstructure of as-cast alloy 1B.

a) Non polygonal ferrite grains (Nital etch)

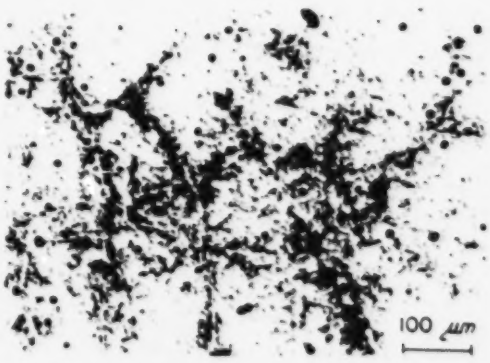

c) Boron autoradiograph showing diffusion of boron away from austenite boundaries

b) Detail of microstructure with very large ferrite grain. Austenite boundaries are outlined by precipitates (Nital etch)

Fig. 4.40: Microstructure of as-cast alloy 5B.

a) Row of dendritic precipitates

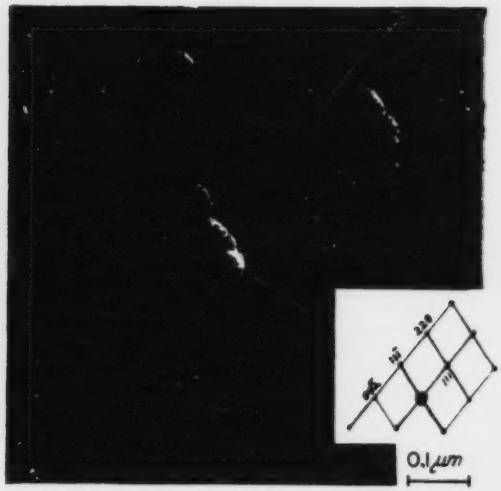

b) Enlarged view showing dendritic (Ti,Nb)C precipitates

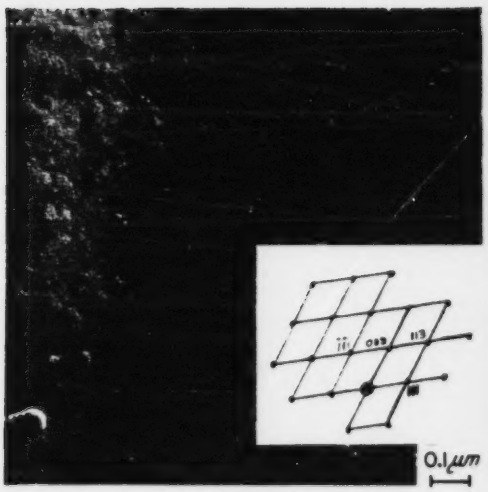

c) Needle-like NbC precipitates

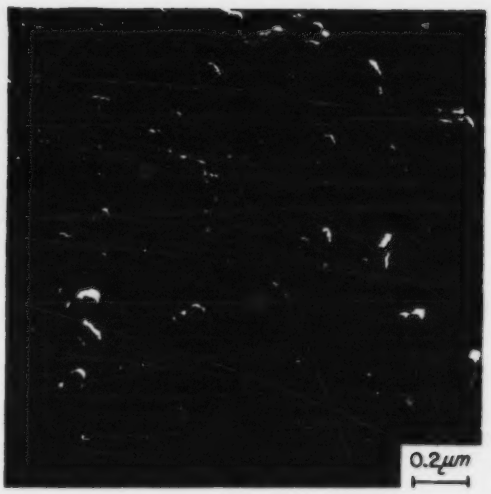

d) General view of precipitates

Fig. 4.41: Analysis by SAD of precipitates in as-cast alloy 1B.
(Carbon replicas)

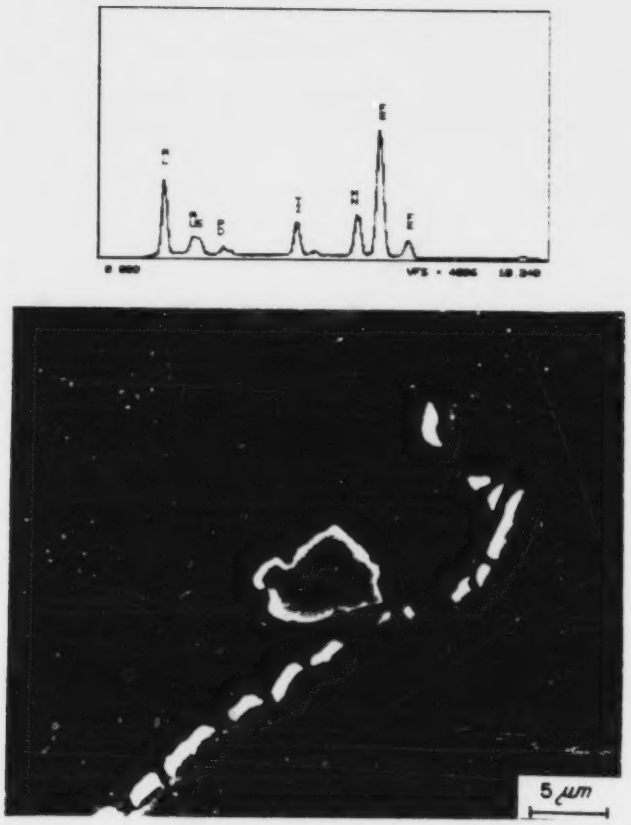

Fig 4.42: EDAX analysis of inclusion in Alloy 1B.
(As-cast material, boiling aqueous saturated picric acid etch)

Specimen No.	Alloy No.	Partial Composition (wt%) C	N(ppm)	Ti	B	Effective Boron (%) Beff=Btot-[N-0,002-Ti/5]
0-300	0	0,020	59	0,025	-	-
1-300	1 A	0,019	32	0,023	0,0016	0,0016
1C-300	1 C	0,022	102	0,025	0,0012	< 0

Table 4.7: Composition of Dilatometry Specimens Used to Evaluate the Influence of Boron and Nitrogen Contents on the Transformation Behaviour.

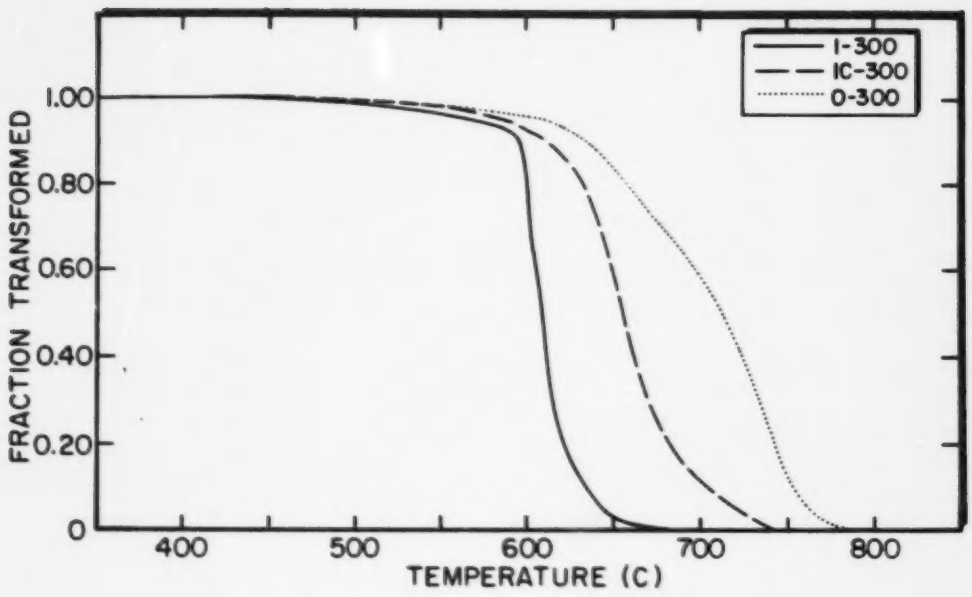

Fig 4.43: Effect of boron and nitrogen contents on the transformation behaviour of the experimental boron steels.

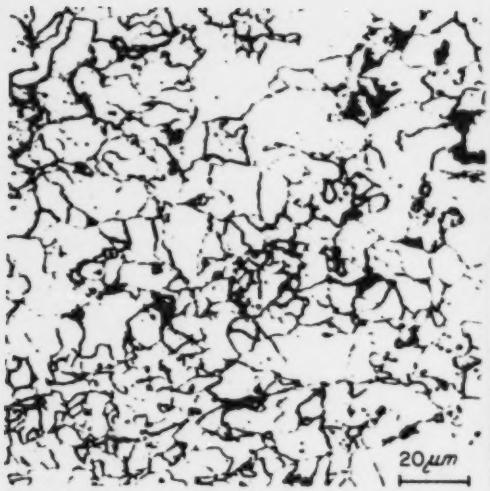

a) Specimen 0-300: polygonal ferrite and pearlite

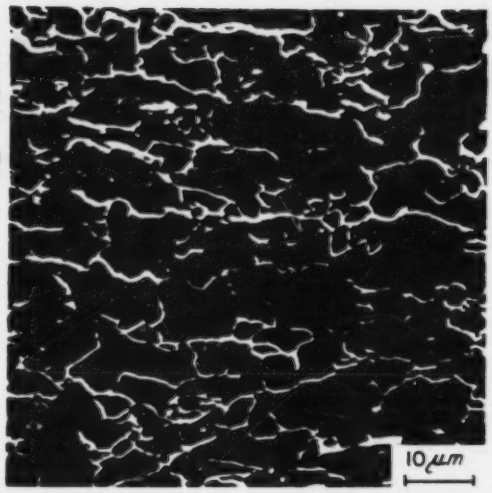

b) Specimen 1C-300: fine grained apolygonal ferrite

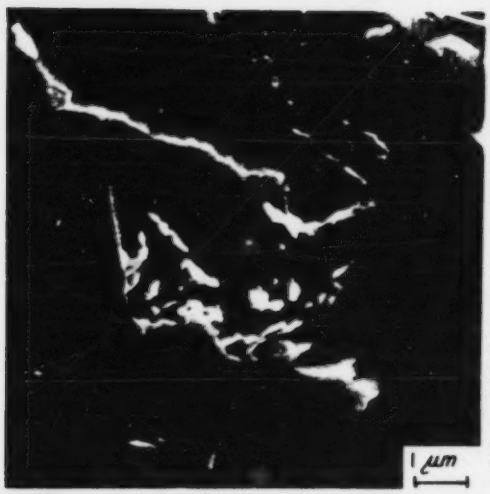

c) Specimen 1C-300: detail showing small MA and degenerate pearlite island

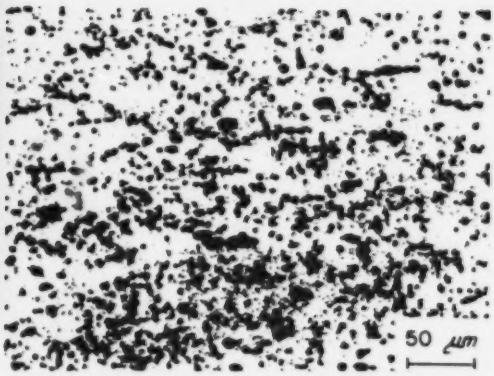

d) Specimen 1C-500: boron autoradiograph showing boron precipitates on grain boundaries and inside the austenite grains

Fig. 4.44: Effect of boron and nitrogen contents on the microstructure of the experimental boron alloys.

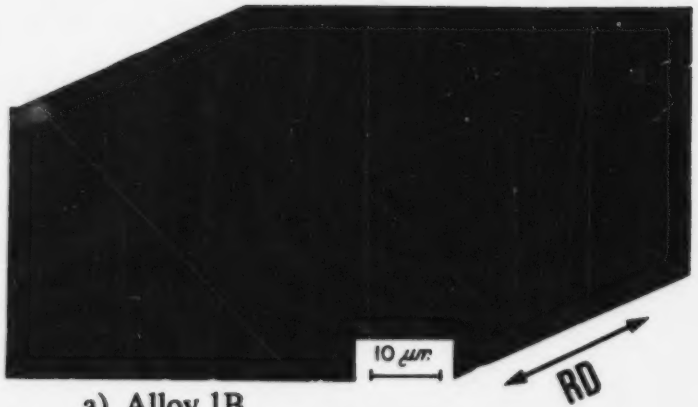

a) Alloy 1B

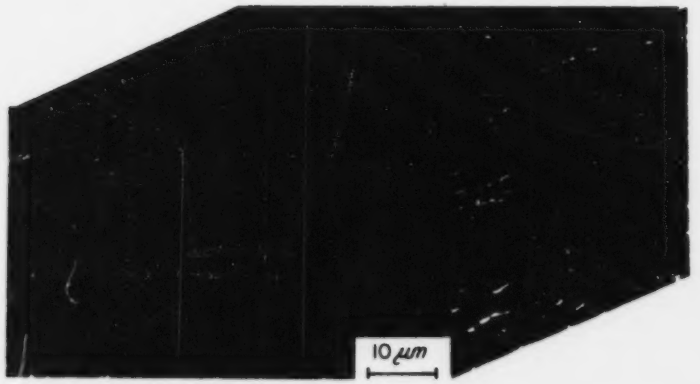

b) Alloy 2B

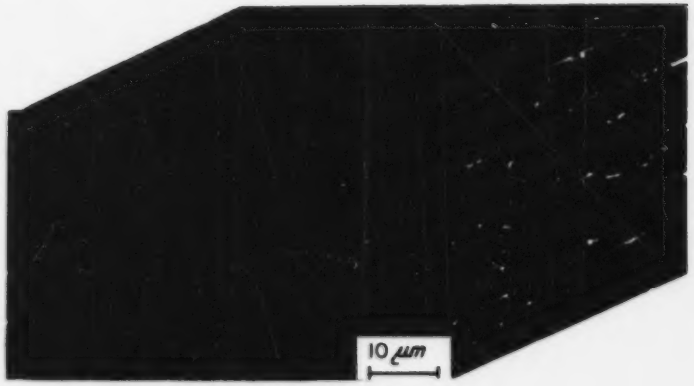

c) Alloy 5B

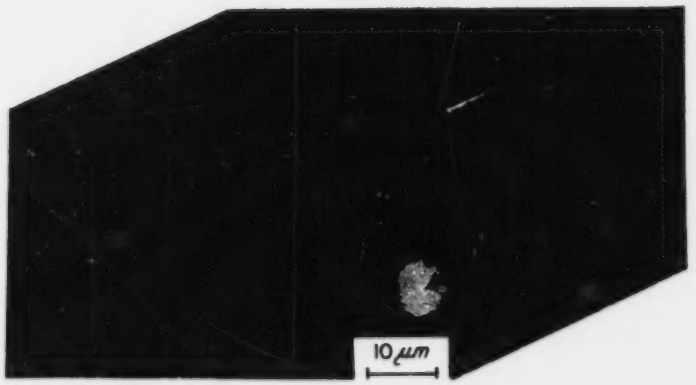

d) Alloy 7B

Fig. 4.45: Microstructure of as-rolled and accelerated cooled steels (SEM).

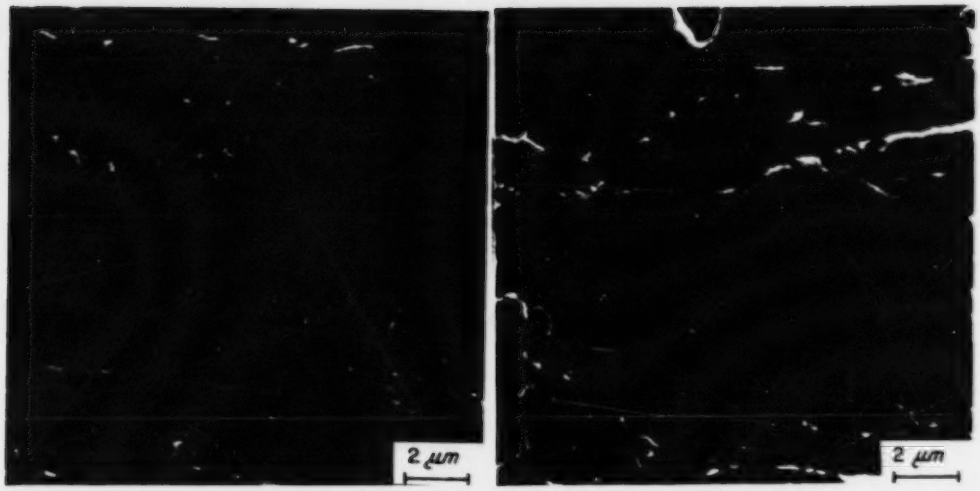

a) Steel 1B (longitudinal section): acicular ferrite with bands of smaller ferrite grains and MA on the subboundaries

b) Steel 2B (transverse section): acicular ferrite with large raised ferrite island and MA on subboundary

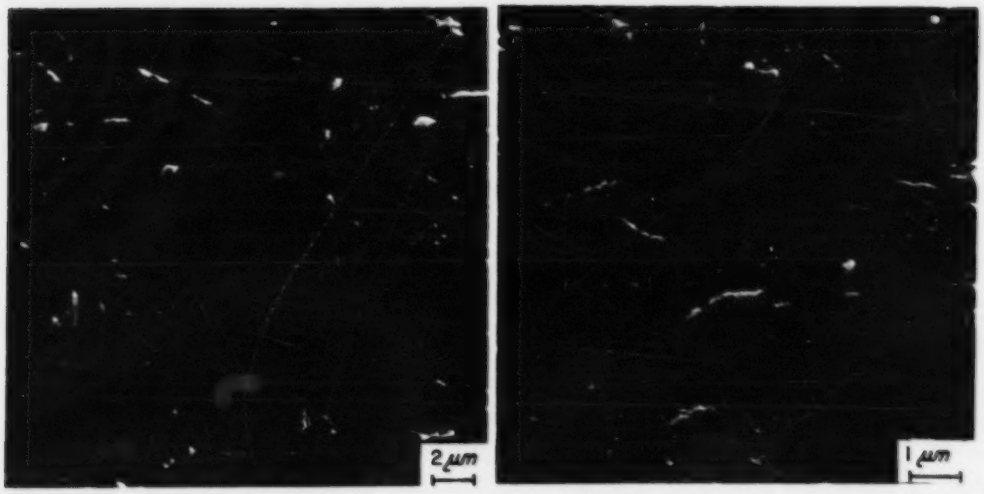

c) Steel 5B (longitudinal section): acicular ferrite and polygonal ferrite grains

d) Steel 7B (transverse section): acicular ferrite with bainite and MA islands

Fig. 4.46: Microconstituents in as-rolled and accelerated cooled steels.

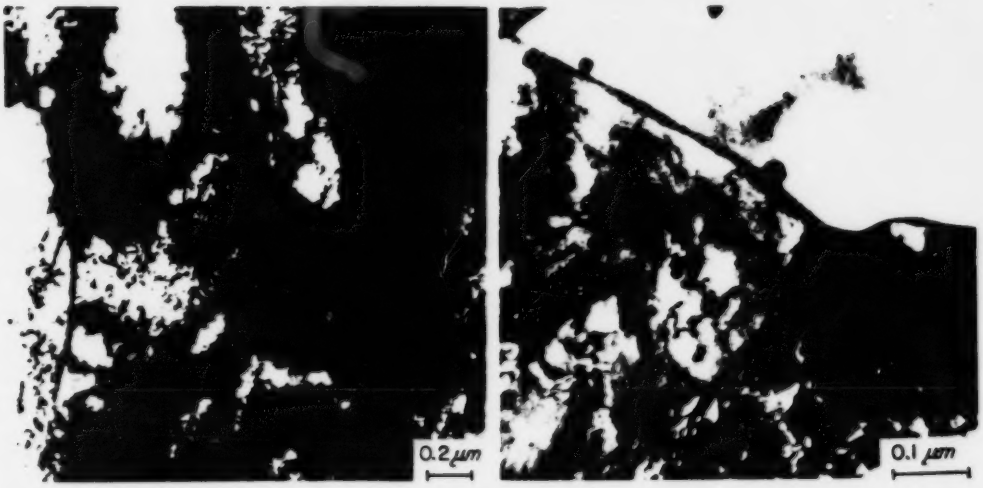

a) Steel 1B: Fine acicular ferrite grains with high dislocation density

b) Steel 1B: detail of dislocation network and small precipitates

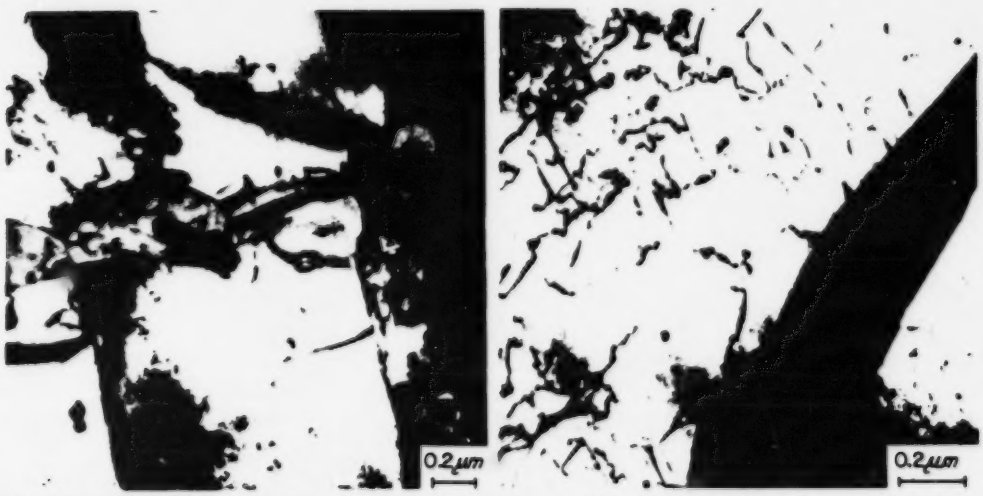

c) Steel 2B: Fine acicular ferrite subgrains with MA islands

d) Steel 5B: large ferrite grain with MA islands.

Fig. 4.47: Transmission electron micrographs of as-rolled and accelerated cooled steels (thin foils).

Alloy No.	Plate Cooling	Y.S. (0,2 %) (MPa)	T.S. (MPa)	El (%)	ROA (%)	v.T.T. (55J) (°C) *	VHN 10	Volume Fraction of MA (%)
1 A	air	426	600	28	63	< -100	205	9.4
1 B	accelerated	459	557	32.4	78	< -100	183	7.8
2 A	air	416	584	32.8	74	< -100	185	10.5
2 B	accelerated	478	612	30.4	75	< -100	195	13.1
5 A	air	455	611	26.5	55	-95	206	9.5
5 B	accelerated	454	545	33.8	77	< -100	180	5.9
7 A	air	391	600	33.2	64	< -100	179	8.2
7 B	accelerated	475	623	32.7	72	< -100	201	13.1

*Longitudinal specimens

Table 4.8: Mechanical Properties of As-rolled Experimental Boron Steels.

Alloy No.	C (%)	Btot (%)	Beff (%)	N (ppm)
1 A	0,019	0,0016	0,0016	32
1 B	0,015-0,018	0,0015	0,0010	65
2 A	0,028	0,0015	0,0015	33
2 B	0,04-0,043	0,0015	0,0015	50
5 A	0,018	0,0037	0,0037	34
5 B	0,023	0,0032	0,0013	79
7 A	0,066	0,0023	0,0017	68
7 B	0,060	0,0010	0,0010	50

$B_{eff} = B_{tot} - [N - 0{,}002 - Ti/5]$ (5, 31)

Table 4.9: Comparison of Carbon Content and Effective Boron Content of As-rolled Experimental Boron Steels.

Alloy No	Plate Cooling	Yielding Behaviour	N (ppm)	Free N* (ppm)	Microstructure
1 A (8mm plate)	air	continuous	32	0	acicular ferrite (AF) + MA
1 B	accelerated	discontinuous	65	5	AF + 7.8% MA
2 B	accelerated	continuous	50	0	AF + 13.1% MA
5 B	accelerated	discontinuous	79	19	polygonal ferrite + AF +5.9%MA
7 B	accelerated	discontinuous	50	0	AF+13.1%MA
6 A	air	continuous	50	0	AF+ 12.7%MA
6 B	accelerated	continuous	50	0	AF+9.9%MA

* Free N = N - 0,002 - Ti/5 (From $B_{eff} = B_{tot}$ - [N-0,002 - Ti/5]

Table 4.10: Yielding Behaviour of Some Experimental Boron Steels.

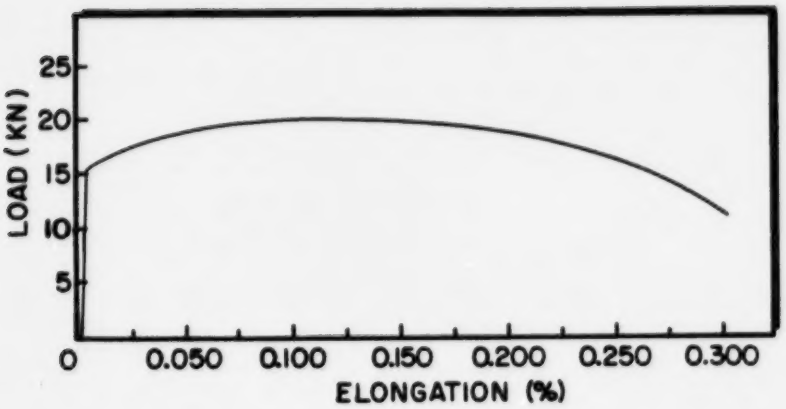

a) Steel 2B

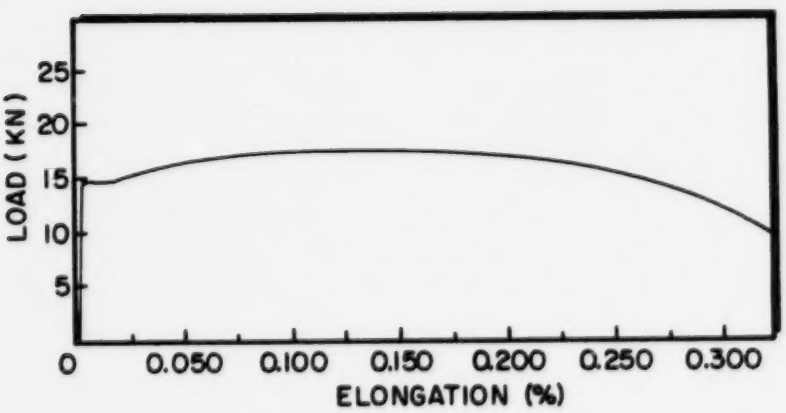

b) Steel 5B

Fig. 4.48: Load vs elongation curves for accelerated cooled steels. (Tensile test)

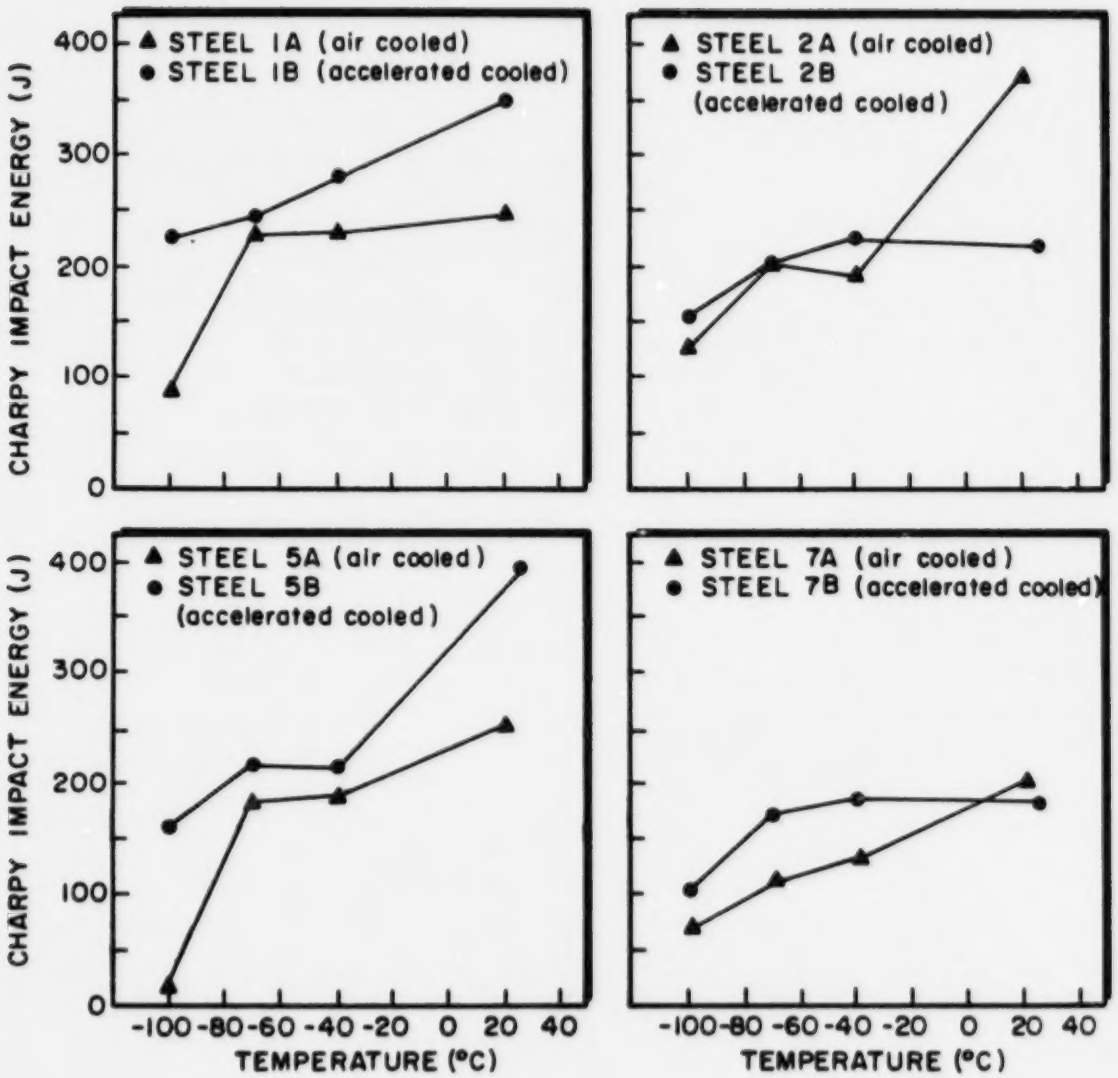

Fig. 4.49: Comparison of impact test results for as-rolled and accelerated cooled steels and for as-rolled and air cooled steels.

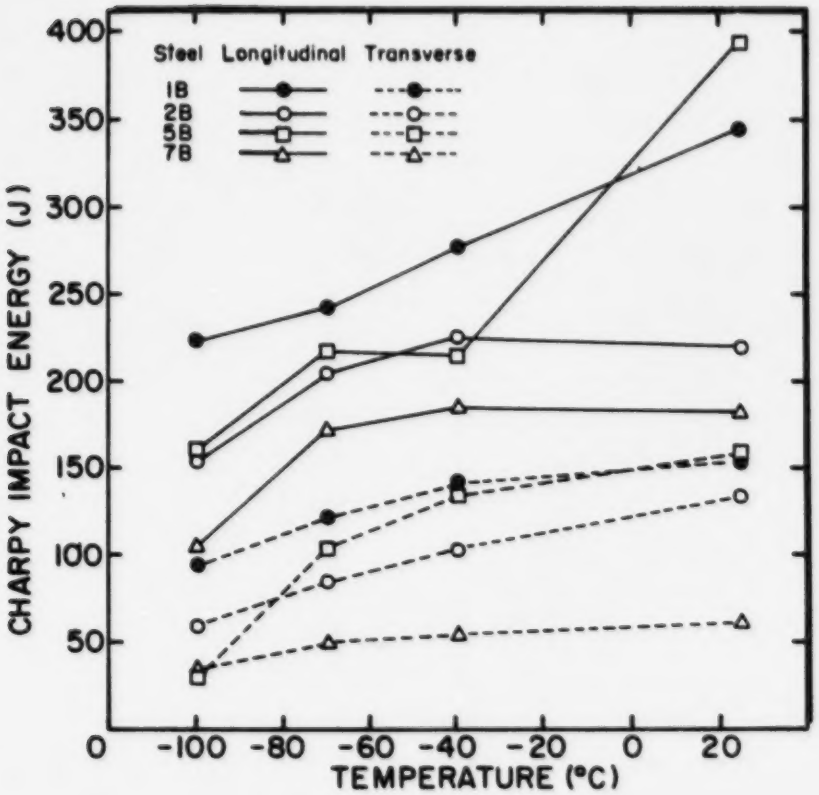

Fig 4.50: Effect of specimen orientation on impact toughness of as-rolled and accelerated cooled steels.

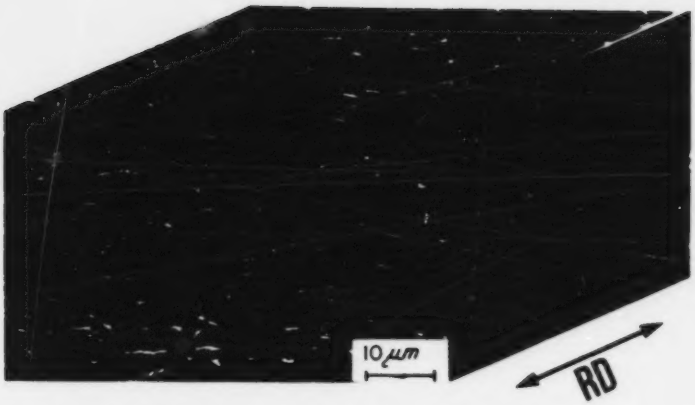

a) Three-dimensional view (SEM)

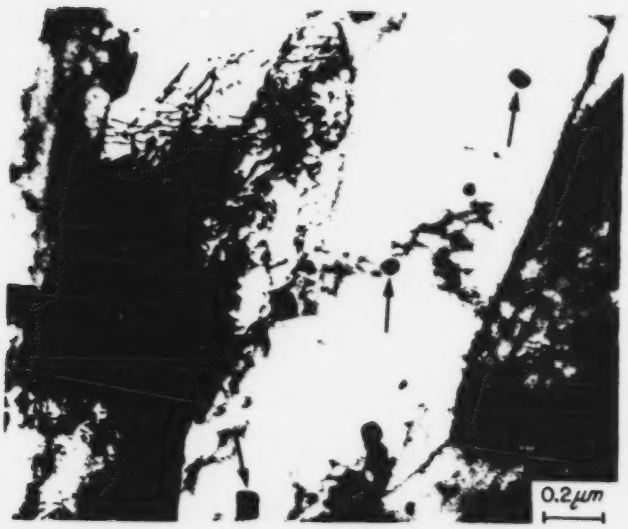

b) Transmission electron micrograph showing acicular ferrite grains with fine (Ti,Nb)(C,N) precipitates

Fig. 4.51: Microstructure of steel 6A (air cooled).

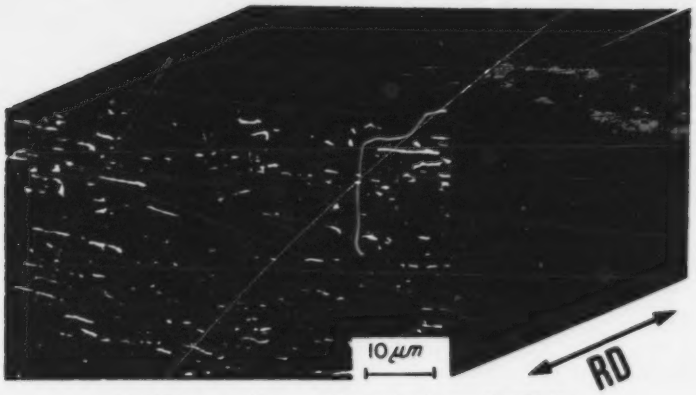

a) Three-dimensional view (SEM)

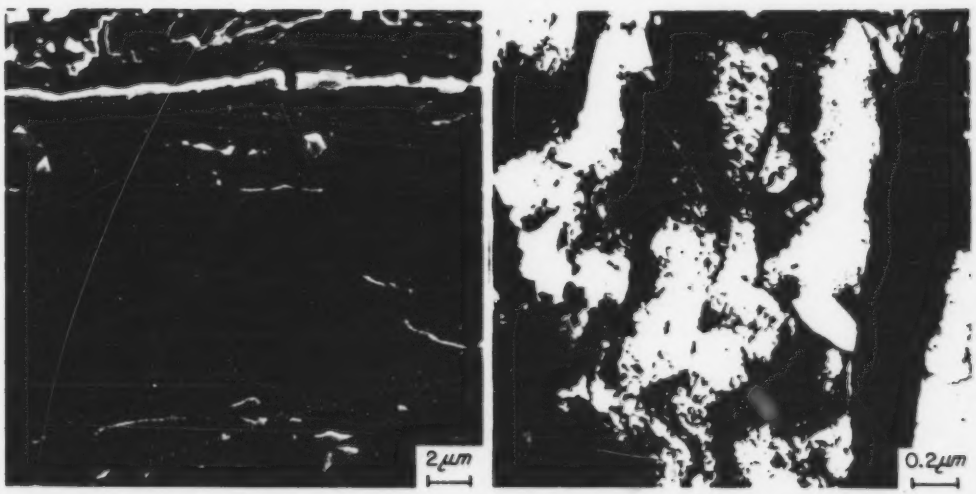

b) Detail of longitudinal section showing elongated MA island on grain boundary

c) Transmission electron micrograph showing high dislocation density acicular ferrite grains and subgrains

Fig. 4.52: Microstructure of steel 6B (accelerated cooled).

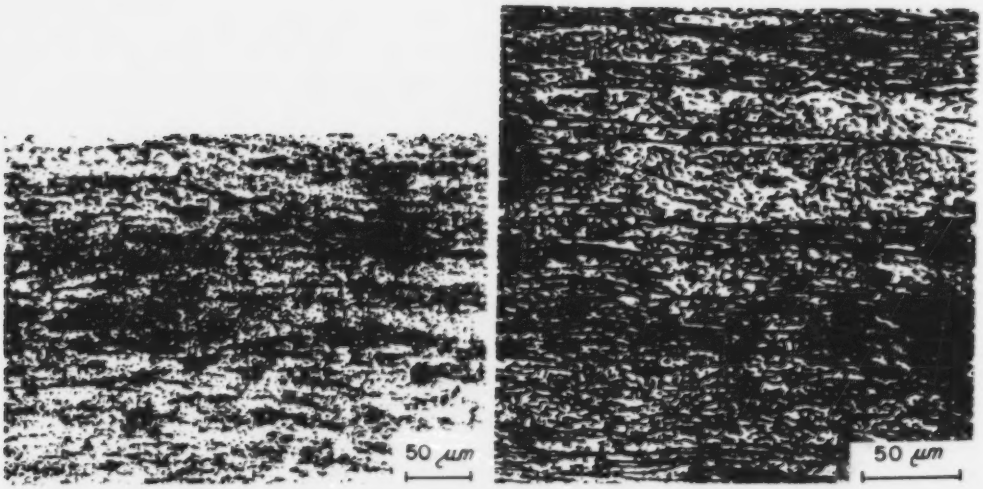

a) Boron autoradiograph

b) Steel 6B etched for austenite grain boundaries

Fig. 4.53: Boron distribution for steel 6B.

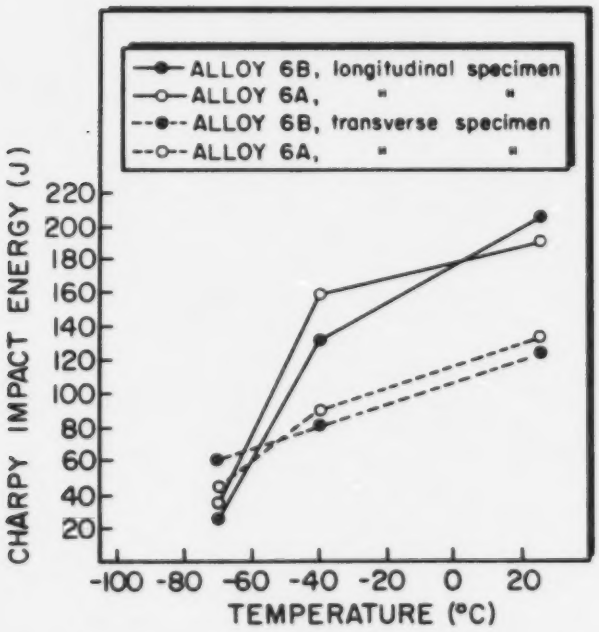

Fig. 4.54: Charpy impact properties of steels 6A and 6B.

Alloy No.	Plate Cooling	Y.S. (0,2% offset) (MPa)	T.S. (MPa)	El (%)	ROA (%)	55J T.T. (°C)	VHN10	Volume Fraction of MA (%)
6 A	air	499	674	25	73	-65	218	12.7
6 B	accelerated	505	688	23.6	75	-62	219	9.9

*Longitudinal specimens

Table 4.11: Mechanical Properties of Cu-Mo-B Steels.

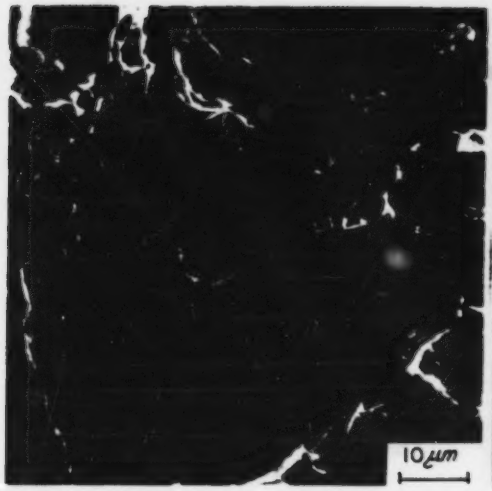

a) Quasi-cleavage and small dimples on fracture surface of steel 6B

b) Path of a secondary crack through microstructure of obliquely sectionned specimen (steel 6B)

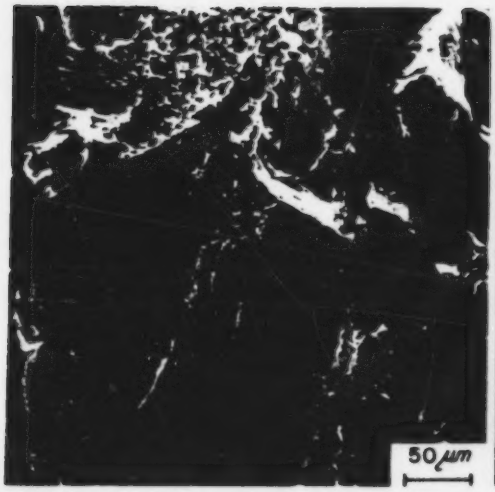

c) Dimples with small amount of quasi-cleavage on fracture surface of steel 6A

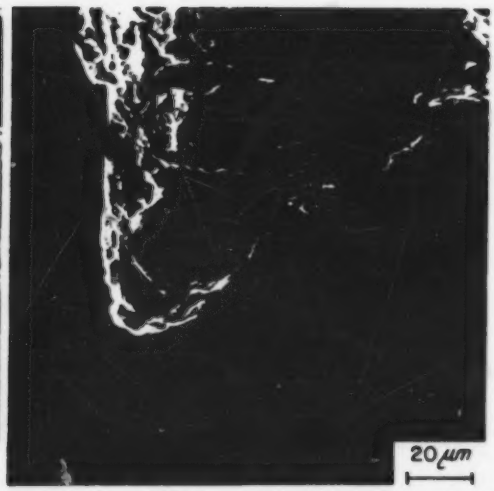

d) Oblique section of steel 6A showing deformed microstructure at the root of a split

Fig. 4.55: Fractography of Charpy specimens of steels 6A and 6B broken at -70°C.

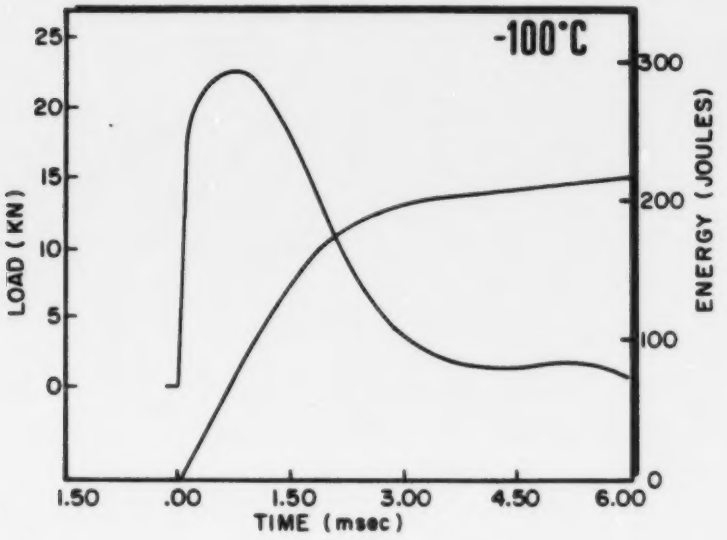

a) Alloy 1B

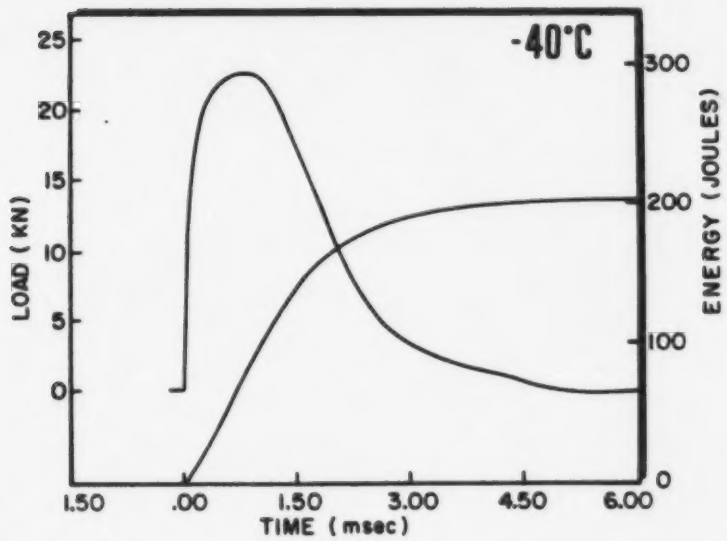

b) Alloy 6B

Fig. 4.56: Instrumented Charpy impact test results.
(Load vs time and energy vs time traces)

Alloy No.	Plate Cooling	Test Temperature (°C)	Initiation Energy (J)	Propagation Energy (J)
1 A	air	20	75	170
		-40	81	148
		-70	85	143
		-100	-	-
1 B	accelerated	25	73, 78	220, 310
		-40	78, 76	174, 230
		-70	68, 83	180, 155
		-100	61, 62	158, 166
6 A	air	25	82, 64	123, 111
		-40	40, 34	150, 93
		-70	5, 4	21, 34
		-100	-	-
6 B	accelerated	25	83, 83	123, 120
		-40	19, 71	39, 133
		-70	5, 5	16, 23
		-100	-	-

Table 4.12: Initiation and Propagation Energies of Some Experimental Boron Alloys During Instrumented Charpy Impact Testing of Longitudinal Specimens.

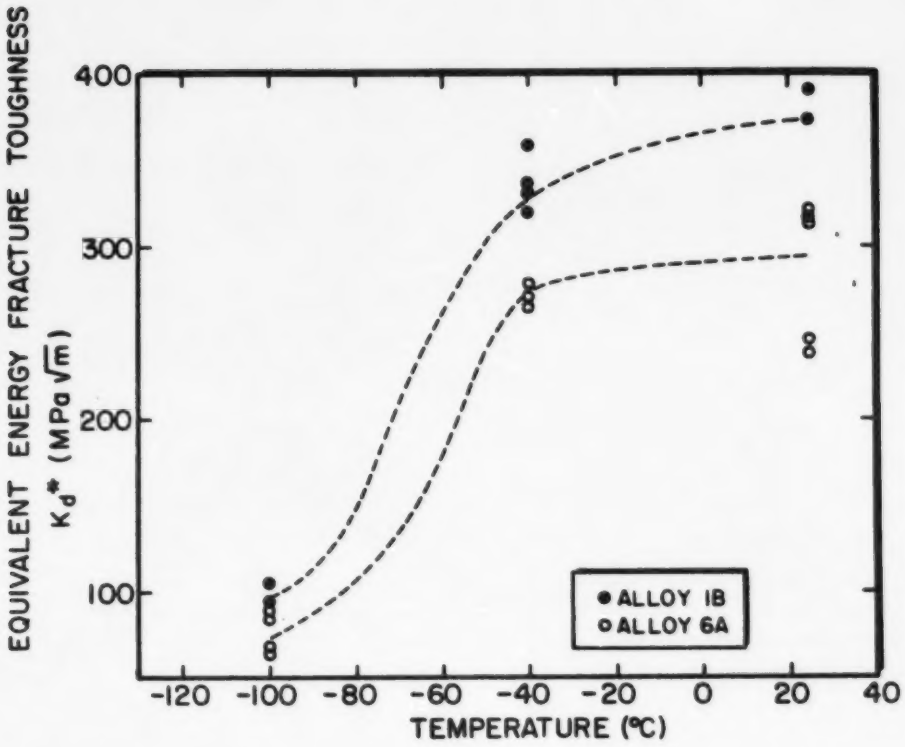

Fig 4.57: Equivalent energy fracture toughness vs temperature for alloys 1B and 6A (precracked Charpy impact test).

Alloy No.	Condition	VHN 10
2 B	as-rolled	195
2 B	quenched and tempered *	211
6 B	as-rolled	219
6 B	quenched and tempered *	230

* 950°C for 1 hour + water quench
+ 600°C for 1 hour + water cool

Table 4.13: Hardness of Alloys 2B and 6B in the As-rolled and in the Quenched and Tempered States.

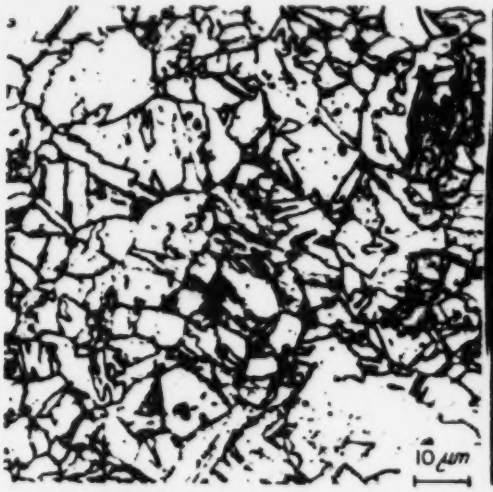

a) Alloy 6B (quenched and tempered)

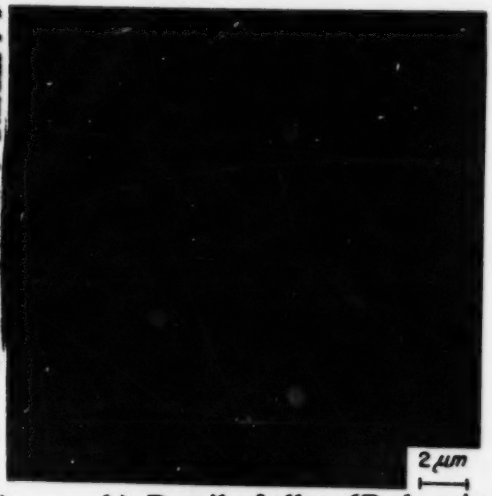

b) Detail of alloy 6B showing lath acicular ferrite with few MA islands

c) Alloy 2B (quenched and tempered)

Fig. 4.58: Microstructure of heat treated experimental boron HSLA steels.

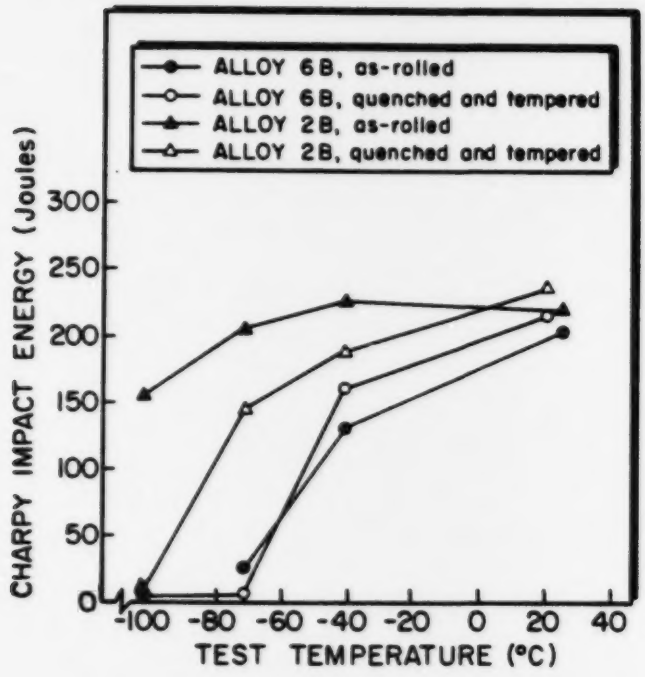

Fig 4.59: Impact properties of heat treated alloys 2B and 6B. (Quenched and tempered)

CHAPTER FIVE

CONCLUSION

5.1 Major Conclusions Arising from this Study

1. In the as-rolled and air cooled experimental boron HSLA steels, boron was only partially effective, resulting in a smaller strength increment than expected. This was explained by a depletion in free boron caused by segregation of boron to MnS and Al_2O_3 containing inclusion stringers. Microstructure of the air cooled boron HSLA steels consisted of a mixture of acicular ferrite, polygonal ferrite and martensite-austenite (M.A.) microconstituents. The steel with similar composition but without boron was composed of polygonal ferrite and pearlite islands.

2. Continuous cooling transformation diagrams were established for three experimental boron alloys (1A, 5A and 7A). The results showed that boron effectively retards the $\gamma \rightarrow \alpha$ transformation even for cooling rates slower than $1°Cs^{-1}$ (air cooling of a 13 mm plate) in the case of alloys 1A and 5A. The resulting microstructures are composed of acicular ferrite and M.A. constituents.

3. When boron is fully effective, a 15 ppm addition is sufficient to obtain fully acicular ferrite microstructures. Adding 37 ppm of boron instead of 15 ppm did not produce any significant improvement of the hardenability.

4. Deformation dilatometry experiments showed that boron confers a cooling rate independance over a wide range of rates to the transformation behaviour which is not obtained when hardenability is attained through increased carbon, manganese and copper contents.

5. No strong correlation could be established between the hardness and the volume fraction of M.A. constituents in these alloys. Strength and hardness of the experimental boron HSLA steels depend upon the relative volume fractions of polygonal ferrite and high dislocation density acicular ferrite.

6. Variations in dilatometer deformation schedules did not produce any significant variations in transformation behaviour, even though some schedules involved recrystallization of the austenite while the others did not. Specimens subjected to different austenitizing temperatures also showed similar transformation behaviour.

7. The hardenability of alloy 1A was decreased somewhat when a longer holding time was used prior to final cooling of the dilatometry specimens. The longer holding time produced a more extensive NbC precipitation, resulting in a depletion of soluble niobium and a decreased hardenability. However, the resulting microstructure was still completely acicular ferrite showing that this is not the critical parameter controlling the hardenability of these boron HSLA steels.

8. Subjecting the as-rolled and air cooled material to a schedule similar to the schedules used during dilatometry experiments (reaustenitization + 50% deformation) is sufficient to fully restore the hardenability by breaking up inclusion stringers and redistributing boron.

9. Even in the higher nitrogen alloy 1C, fine grained apolygonal ferrite with few pearlite islands was obtained. This was caused by enhanced ferrite nucleation on the boron nitride precipitates or may also have been caused by some boron remaining free despite the high nitrogen content. The formula used to predict the effective boron content ($B_{eff} = B_{tot}$ - [N-0,002 -Ti/5] (5,31)) may have overestimated the level of nitrogen free to combine with boron.

10. Using accelerated cooling instead of air cooling produced steels with slightly higher volume fractions of acicular ferrite and less polygonal ferrite. The best results were obtained for higher carbon alloys 2B and 7B, in which all of the boron was effective. Even for these, the strength increment was smaller than expected. It was found that the difference in cooling rate between air cooling (1°C s^{-1}) and accelerated cooling (8°Cs^{-1}) was too small to have a significant effect on the transformation behaviour of these boron HSLA steels.

11. Copper (0,305%) and molybdenum (0,195%) can be added to the boron HSLA composition to improve the strength with only a small decrease in toughness. After heat treatment (950°C for one hour, water quench and tempering at 600°C for one hour), the strength is further increased due to the lath acicular ferrite microstructure produced. The strength increment is also due to solid solution strengthening by copper and molybdenum.

12. All of the experimental boron HSLA steels have excellent toughness. Despite the fact that it has the lowest toughness of all the experimental steels, Cu-Mo-B steel 6B has a 55J transition temperature of -62°C. Fracture surfaces of Charpy specimens broken at -100°C were composed of quasi-cleavage with no trace of intergranular fracture. Load-time traces of instrumented Charpy impact tests performed at -70°C showed that significant plastic deformation occurs before fracture initiation.

5.2 Industrial Applications

Our work has clearly demonstrated that by proper steel making and processing practice, adequate boron hardenability effect can be obtained in HSLA steels. In addition, since boron confers cooling rate independence to the transformation behaviour over a wide range of rates, and since its effect is not altered significantly by changing the deformation schedule, there is enough room for flexibility for the Canadian steel industry to adopt the boron HSLA steel technology. Also the boron-effect can be enhanced by the addition of other alloying elements namely Nb, Mo and Cu, thus permitting the achievement of higher section capacity along with increased strength levels.

These findings have considerable practical significance in terms of Canadian industry taking up the production of advanced boron-containing HSLA steels for a multitude of applications; for example (i) heavy section plates with high heat input welding capability for off-shore structures, ice breakers, naval ships, and deep submersibles, (ii) ultra-low carbon low-nickel steels for LPG storage tanks, (iii) high strength sulfide-stress cracking (SSC) resistant casing and tubing for deep wells, and (iv) dual and tri-phase steels for automotive applications.

Heavy Section Off-shore and Naval Structural Applications

With the emphasis on developing the Hybernia oil fields, and the anticipated construction of Arctic ice breakers, naval ships and submarines, there is the need, in Canada, of developing the indigenous technology of producing advanced HSLA steels with high heat input welding capability. As weld length increases with the increase in size of structures, reducing the welding cost becomes an important factor. The number of welding passes must be decreased by welding with large heat input.

Boron, in addition to conferring hardenability to the base plate, would help, along with titanium, in controlling the HAZ microstructure, thus imparting good resistance for high heat input welding. Although only moderate levels of copper have been used in the study, one can certainly employ at least up to 1,5% copper to increase the strength level to 550 MPa and beyond (up to 690 MPa). Thus one could develop HSLA steels with strength levels in the range 500 to 700 MPa with adequate section capability (50 mm and over) and toughness. Since these steels would have extra low carbon levels due to the hardenability imparted by boron, the costly pre-heating before welding would not be required. Up to now, there is no steel mill in Canada which produces these type of advanced HSLA steels with improved weldability. But, with the acquisition of ladle refining facilities, soon many Canadian mills will have the capability.

Line Pipe For Sourgas Applications

Line pipes used in wet H_2S environment should have a high resistance to HIC (hydrogen induced cracking) and SSCC (Sulfide Stress Corrosion

Cracking). Although canadian codes limit the maximum yield strength for sour service to 550 MPa (and in practice lower yield strength materials are used), one could certainly anticipate a demand for higher strength materials due to the extended applications of sour oil and gas pipelines. Cu-B-Ti steels would be very useful for these applications as copper additions are effective in reducing hydrogen absorption by forming a stable protective film on the steel surface when the copper content is 0.3% or higher. Titanium is well known to provide improved resistance to hydrogen. Boron permits the lowering of carbon level there by improving field weldability, and it also decreases the hardness of segregation zone which is closely related to the susceptibility to HIC. In fact, considerable work is being done in Japan, in developing extra low carbon B-Cu-Ti steels for sour gas line pipes.

2.5 Ni Steels for LPG Storage Tank

Steel plates for LPG storage tanks must meet stringent criterion for toughness for preventing crack initiation in the HAZ and for arresting crack propagation in the base plate. To achieve this, extra to ultra-low carbon levels (0,03 to 0,01%) are necessary. Again, to compensate for the loss in hardenability, boron could be added. Along with minor additions of titanium and copper, one could certainly develop more weldable and tougher steels than presently available.

Dual and Tri-phase Formable Steels for Automotive Applications

Although present work is mainly concerned with the development of plate products, some of the findings have relevance to the use of the steels for automotive applications. Boron containing dual-phase and tri-phase steels could be certainly designed since the experimental boron HSLA steels examined in this study have a microstructure consisting of fine grained ferrite, acicular ferrite and M.A. constituent. Boron and titanium can also be used to produce interstitial free steels for automotive use. These elements combine with nitrogen to form BN and TiN, thereby reducing the free nitrogen content in the material.

5.3 Recommandations for Further Work

1. It would be worthwhile to make thicker plates of some of the experimental boron HSLA steels as means of testing their section capability. Using Jominy testing might also provide a wider range of cooling rates and be more representative of industrial practice.

2. The effects of boron on HAZ toughness of low carbon steels should also be examined as the mechanisms of HAZ grain refinement by boron addition are not yet very clear.

3. There is the definite need to ascertain more clearly the role of inclusions in boron HSLA steels. Comparative studies using ultraclean steels with extremely low sulfur and low nitrogen levels would help in separating the overlapping effects.

4. Higher copper (1,5%) and molybdenum (0,5%) additions should be tried to increase strength levels to 550 MPa and beyond as they increase the strength without causing too much deterioration in toughness of the boron HSLA steels.

5. Identification of the boron phases found at the austenite grain boundaries and at the matrix/inclusion interfaces in the experimental boron steels should be performed. The boron precipitates could be extracted onto replicas using the Selective Potentiostatic Etching technique described by M. Saeki and co-workers (15).

6. The use of boron in forged medium carbon steels should also be investigated. By breaking up inclusion clusters and redistributing the alloying elements more evenly, forging should be an effective means of securing the desired boron hardenability effect.

APPENDIX A

IDENTIFICATION OF PRECIPITATES BY ANALYSIS OF ELECTRON DIFFRACTION PATTERNS

The diffraction of electrons is possible because of their wave-mechanical behaviour [23]. When a focussed (parallel) beam of electrons passes through a crystal, diffraction occurs if the conditions given by the Bragg law are fulfilled:

$$n\lambda = 2d \sin \Theta$$

- λ is the wavelength of the electrons.
- Θ is the angle of incidence between the beam of electrons and a set of crystallographic planes giving rise to the diffraction spot.
- d is the interplanar spacing of these planes.

When n = 1 (first order diffraction) the Bragg law can be rewritten as $1/d = 2\,(1/\lambda) \cdot \sin \Theta$.

Fig. A.1 illustrates the basic geometry of electron diffraction. Because the electron wavelength is very small, the angle Θ small and P' is very near to P (see fig. A.1). By relating distances and angles in the crystal lattice we can write:

$$\frac{d/2}{L} = \tan 2\Theta$$

Since Θ is small, $\tan 2\Theta \approx 2 \sin \Theta \approx 2\Theta$.

Therefore: $D = 2L \cdot 2\Theta$ and by substitution:

$D = 2L \cdot \lambda/d$

$D \cdot d = 2L\lambda = K$ where "K" is the camera constant.

The camera constant is specific for a given acceleration voltage and camera length setting used when the diffraction pattern is obtained. "D" is the diameter of the ring (in a ring pattern) or the distance between spots symetrically placed on either side of the central spot (in a spot pattern). A ring pattern is formed when grains of many orientations have planes in the right positions for diffraction i.e. when diffraction patterns are taken from polycrystalline material.

Calculation of the camera constant

For each acceleration voltage and lens current setting used, the camera constant must be calculated. For this, a ring pattern is obtained from a known standard (in this case, a foil of pure evaporated aluminum). Since aluminum has a face-centred cubic structure, the rings can be indexed by checking that for each ring, the following relationship is obeyed:

$$D_i^2 / D_1^2 \propto h_i^2 + K_i^2 + l_i^2$$

where D is the measured diameter of the i^{th} ring.
D_1 is the diameter of the smallest ring (nearest to the central spot).
$(h_i\ K_i\ l_i)$ are the Miller indices of the crystallographic planes giving rise to the i^{th} ring.

The actual camera constant is then taken as the mean of the Di • di products for each ring:

$$K = 1/m \sum_{i=1}^{m} D_i \cdot d_i$$

where "m" is the number of rings measured. The ring diameters can be measured with a precision of +/- 0,02 mm.

Identification of unknown phases

Unknown phases such as precipitates or inclusions in carbon replicas of thin foils can be identified by means of their diffraction patterns. The diffraction patterns are obtained by using a diffraction lens aperture of 30 μm diameter (Pt) to obtain a selected area on the specimen of approximately 1 μm in diameter. For very small precipitates the microprobe mode was used. In this case, the electron beam is focussed directly on the specimen so that the size of the area is selected by the choice of spot size. A spot size of 100 mm was used for microprobe work in this study.

To identify an unknown phase, a diffraction spot pattern is taken from this phase and "D" is measured for at least three spots near the central spot with a precision of +/- 0,02 mm. The interplanar spacings corresponding to each spot are calculated using the relationship:

$$d = K/D$$

where K is the appropriate camera constant
D is the distance between two symetrical spots of either side of the central spot.

The angles between the spots are also measured (see fig. A.2). The "d" values are then compared with those of substances suspected to be the unknown phase and the spots are tentatively indexed. The indexing is verified by comparing the measured angles between the spots with the known angles between planes for the crystal system of the suspected phase. The angles should match +/- 2°. The hkl values assigned to the spots should satisfy the zone axis relationship.

$$hu + kv + lw = 0$$

where (u v w) is the zone axis or lattice orientation

and $u = k_1l_2 - l_1k_2$

$v = l_1h_2 - h_1l_2$

$w = h_1k_2 - k_1h_2$

for any two planes $(h_1\ k_1\ l_1)$ and $(h_2\ k_2\ l_2)$ belonging to the pattern.

Interplanar spacings for various substances can be found in references (23) and (69). Reference (23) also gives tables for angles between planes for cubic and hexagonal crystals and equations to calculate these angles for other lattices.

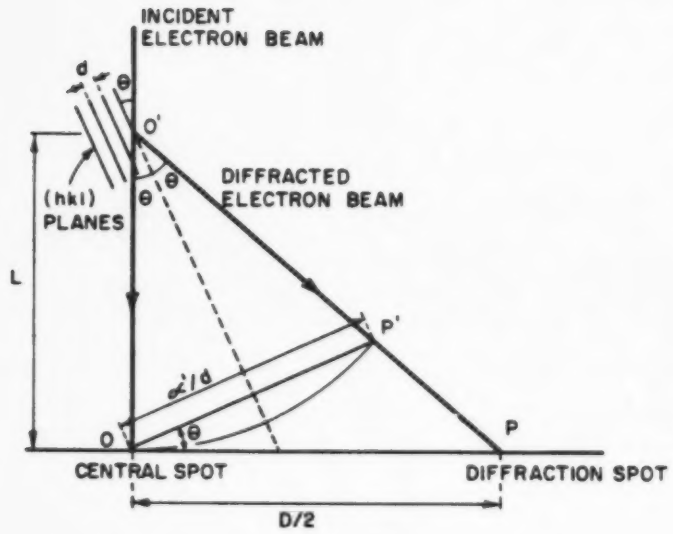

Fig. A.1: Basic geometry of electron diffraction.

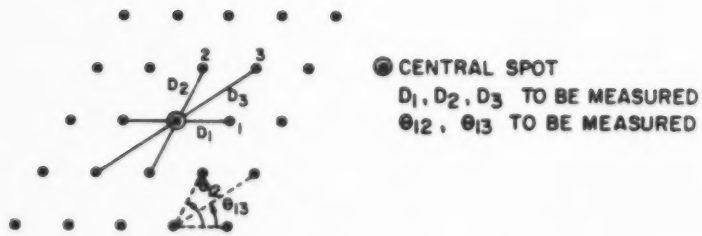

Fig. A.2: Measurements required for interpretation of a single crystal electron diffraction pattern.

References

(1) J.F. Jandeska and J.E. Morral, "The Distribution of Boron in Austenite", Metallurgical Transaction 3 (11) (1972) 2933-2937.

(2) S.R. Keown and F.B. Pickering, "Some Aspects of the Occurence of Boron in Alloy Steels", Metal Science 7 (1977) 225-234.

(3) P. Maîtrepierre et al., "The Influence of Boron on the Decomposition of Austenite in Low Carbon Alloyed Steels", Metallurgical Transaction A, 6(2) (1975) 287-301.

(4) P. Maîtrepierre, J. Rofès-Vernis and D. Thivellier, "Structure Properties Relationships in Boron Steels", Boron in Steel ed. S.K. Banuji and J.E. Morral (Warrendale, PA: The Metallurgical Society of AIME, 1980) 1-18.

(5) B.M. Kapadia, "Prediction of the Boron Hardenability Effect in Steel - A Comprehensive Review", Hardenability Concepts with Applications to Steel, ed. D.V. Doane and J.S. Kirkaldy (Warrendale, PA: The Metallurgical Society of AIME, 1978) 448-480.

(6) B.J. Thomas and G. Henry, "Boron in Austenitic Stainless Steels", Boron in Steel, ed. S.K. Banuji and J.E. Morral (Warrendale, PA: The Metallurgical Society of AIME, 1980) 80-105.

(7) S. Watanabe and H. Ohtani, "Precipitation Behaviour of Boron in High Strength Steel", Transactions ISIJ 23 (1983) 38-42.

(8) O.M. Ankelsen, Ø. Grong and P.E. Kvaale, "A Comparative Study of the Heat Affected Zone (HAZ) Properties of Boron Containing Low Carbon Steel", Metallurgical Transactions A 17 (9) (1986) 1529-1536.

(9) Y. Ohmori and K. Yamanaka, "Hardenability of Boron Treated Low Carbon Low Alloy Steels", Boron in Steel, ed. S.K. Banuji and J.E. Morral (Warrendale, PA: The Metallurgical Society of AIME, 1980) 44-60.

(10) S. Watanabe, H. Ohtani and T. Kunitake, "The Influence of Hot Rolling and Heat Treatments on the Distribution of Boron in Steel", Transactions ISIJ 23 (1983) 31-37.

(11) H. Tamehiro et al. "Optimum Microalloying of Niobium and Boron in HSLA Steel for Thermomechanical Processing", Transactions ISIJ 27 (1987) 120-129.

(12) H. Tamehiro et al., "Optimum Chemical Composition and Thermomechanical Processing Condition for Niobium-Boron Steel" Transactions ISIJ 27 (1987) 130-138.

(13) R.G. Howe, "Grain Boundary Segregation and Grain Growth Inhibition in Silicon Iron: The Effect of Boron and Nitrogen", Metallurgical Transactions A 10 (8) (1979) 997-1011.

(14) S. Veda, M. Ishikawana and N. Ohashi, "Enhanced Nucleation of Polygonal Ferrite grain in the Interior of Austenite Grain in Boron-bearing Steel". Boron in Steel, ed. S.K. Banuji and J.E. Morral (Warrendale, PA: The Metallurgical Society of AIME, 1980) 181-198.

(15) M. Saeki, F. Kurosawa and M. Matsuo, "Micro and State Analysis as the Basis for Microalloying Techniques", Transactions ISIJ 26(1986) 1017-1035.

(16) Y. Okamura et al., "Development of New 100 kg F/mm^2 Class High Tensile Strength Steel", Transactions ISIJ 25(1985) B-268.

(17) K. Sugimoto et al., "Effects of Boron and Nitrogen on Fracture Toughness of Boron-treated 0,35% C Steels Tempered at Low Temperatures", Transactions ISIJ 26 (1986) 328-386.

(18) P. Maîtrepierre et al., "Influence of $M_{23}(C,B)_6$ Precipitation on the Properties of Low Alloy Boron-Containing Steels", Heat Treatment '76 (Stratford-upon-Avon: Metals Society, 1976) 177-187.

(19) K.E. Thelming, "Evaluation and Practical Application of the Hardenability of Boron Steel", Boron in Steel, ed. S.K. Banuji and J.E. Morral (Warrendale, PA: The Metallurgical Society of AIME, 1980) 127-146.

(20) T. Inove and Y. Ochida, "A Fisision-track Etching Study of Boron Hardenability in Ausforge-quenched Steel Products", Transactions ISIJ 23 (1983) B-180.

(21) S. Watanabe, H. Ohtani and T. Kunitake, "The Influence of Dissolution and Precipitation Behaviour of $M_{23}(C,B)_6$ on the Hardenability of Boron Steels", Transactions ISIJ 23 (1983) 120-129.

(22) P. Maîtrepierre et al. "Microstructure and Hardenability of Low-Alloy Boron-containing Steels", Hardenability Concepts with Applications to Steel, ed. D.V. Doane and J.S. Kirkaldy (Warrendale, PA: The Metallurgical Society of AIME, 1978) 421-447.

(23) K.W. Andrews, D.J. Dyson and S.R. Keown, Interpretation of Electron Diffraction Patterns (New York, NY: Plenum Press, Second Edition, 1971).

(24) T. Kikutake et al., "Effects of Processing Variables on the Mechanical Properties of Boron Bearing Low Alloy Steel", Transactions ISIJ 26 (1986) B-278.

(25) J.E. Morral and T.B. Cameron, "Boron Hardenability Mechanisms", Boron in Steel, ed. S.K. Banuji and J.E. Morral (Warrendale, PA: The Metallurgical Society of AIME, 1980) 19-32.

(26) G. Thomas and Y.L. Chen, "Structure and Mechanical Properties of Fe-Cr-Mo-C Alloys with and without Boron", Metallurgical Transactions A 12 (6) (1981) 933-950.

(27) L. F. Porter, "The Present Status and Future of Boron Steels", Boron in Steel, ed. S.K. Banuji and J.E. Morral (Warrendale, PA: The Metallurgical Society of AIME, 1980) 198-211.

(28) T. Hazama et al. "Production of Boron Steels by Continuous Casting" Transactions ISIJ 23 (1983).

(29) Y. Iwasaki et al. "Production of HSLA Seamless Steel Pipes for Offshore Structures and Linepipes by Direct-quench and Tempering", Transactions ISIJ 25 (1985) 1059-1068.

(30) T. Funakoshi et al. "Heavy Plate of Quenched and Tempered Steel with 80 kg/mm^2 Tensile Strength" Translated from Kawasaki Steel Technical Report 4 (3) (1972) 59-69.

(31) B.M. Kapadia, R.M.Brown and W.J. Murphy, "The Influence of N,Ti and Zr on the Boron Hardenability Effect in Constructional Low Alloy Steels" Transaction AIME 242 (8) (1968) 1689-1694).

(32) G.T. Eldis and W.C. Hagel, "Effects of Microalloying on the Hardenability of Steel", Hardenability Concepts with Applications to Steel, ed. D.V. Doane and J.S. Kirkaldy (Warrendale, PA: The Metallurgical Society of AIME, 1978) 397-420.

(33) G.J. Sojka, M.R. Krishnadev and S.K. Banuji, "Boron in HSLA Steels: Potentialities, State of the Art and the Prospects", Boron in Steel, ed. S.K. Banuji and J.E. Morral (Warrendale, PA: The Metallurgical Society of AIME, 1980) 165-180.

(34) M.R. Krishnadev et al., "HSLA Steels Microalloyed with Boron: Their Physical Metallurgy and Engeneering Applications" Japan-Canada Seminar on Secondary Steel making, (Tokyo, Japan: The Iron and Steel Institute of Japan, 1985) C. 10.1 - C-10.15.

(35) L.J. Cuddy, "The Effect of Microalloy Concentration on the Recrystallisation of Austenite During Hot Deformation", Thermomechanical Processing of Microalloyed Austenite, ed. A.J. De Ardo, G.A. Ratz and P.J. Wray (Warrendale, PA: The Metallurgical Society of AIME, 1982) 129-139.

(36) R.K. Amin and F.B. Pickering, "Austenite Grain Coarsening and the Effect of Thermomechanical Processing on Austenite Recrystallization" Thermomechanical Processing of Microalloyed Austenite, ed. A.J. De Ardo, G.A. Ratz and P.J. Wray (Warendale, PA: The Metallurgical Society of AIME, 1982) 1-?.

(37) D.R. DiMicco and A.T. Davenport, "Austenite Recrystallization and Grain Growth During the Hot Rolling of Microalloyed Steels", Thermomechanical Processing of Microalloyed Austenite, ed. A.J. De Ardo, G.A. Raty and P.J. Wray (Warendale, PA: The Metallurgical Society of AIME, 1982) 59-?.

(38) W.J. Tegart and A. Gittins, "The Hot Deformation of Austenite", The Hot Deformation of Austenite, ed. J. Ballance (Warrendale, PA: The Metallurgical Society of AIME, 1977) 1-46.

(39) S.R. Keown and W.G. Wilson, "Prediction of Precipitate Phases in Microalloy Steels Containing Niobium, Carbon, Nitrogen and Aluminum", Thermomechanical Processing of Microalloyed Austenite ,ed. A.J. De Ardo, G.A. Ratz and P.J. Wray (Warrendale PA: The Metallurgical Society of AIME, 1982) 343-356.

(40) N. Shams, "Microstructure of Continuous Cooled Niobium Steels" Journal of Metals, 12 (1985) 21-24.

(41) H. Tamehiro, N. Yamada and H. Matsuda, "Effect of Thermomechanical Control Process on the Properties of High-Strength Low Alloy Steel", Transactions ISIJ 25 (1985) 54-61.

(42) J.-L. Verger-Gauguy, G.Ocampo and J.D. Embury, "Microanalysis of Ti Nb Carbonitudes in HSLA Steels", Metallography, 18 (1985) 381-393.

(43) D.C. Houghton, G.C. Weatherly and J.D. Embury, "Characterization of Carbonitudes in Ti bearing HSLA Steels", Thermomechanical Processing of Microalloyed Austenite, ed. A.J. De Ardo, G.A. Ratz and P.J. Wray (Warrendale, PA: The Metallurgical Society of AIME, 1982) 267-292.

(44) Y. Kusuhara et al., "Properties of High Strength Pipe Line Steel Plates for Low-temperature Use by Accelerated Cooling", Transaction ISIJ 24 (1984) B-357.

(45) H. Takechi et al. "Application of Bainite and Ferrite-Martensite Structure for High Strength Heavy Gage Line Pipe", Micon'82: Optimization of Processing, Properties and Service Performance through Microstructural Control, ed H.J. Alrams, E. Clark, J. Hood and B. Seth (ASTM Publication, STP 792, 1983) 149-171.

(46) H. Nakasugi, M. Matsuda and H. Tamehiro, "Development of Controlled-Rolled Bainitic Steel for Large-Diameter Line-Pipe", International Conference on Steel Rolling, Science and Technology of Flat Rolled Products, Vol. 2 (Tokyo, Jap: The Iron and Steel Institute of Japan, 1980) 1028-1039.

(47) N. E. Hannerz, "Critical Hot Plasticity and Transverse Cracking in Continuous Slab Casting with Particular Reference to Composition" Transaction ISIJ 25 (2) (1985) 149-158.

(48) T. Tsumura, Y. Okada and H. Ohtani, "Effect of Microalloying Elements on the Hardenability and the Properties after Tempering at High Temperature in Boron-Treated Cr-Mo-Nb Steels", Tetsu-To-Hagani 72 (1986) 1367.

(49) Y Kawashima et al., "Basic Principle of Improvement of HAZ Toughness for Steel for Low Temperature Service Under High Heat Input Welding Condition", Transactions ISIJ 22 (1982) B-400.

(50) T. Kan, M. Hiromatsu and H. Kaji, "Improvement in HAZ Toughness of Low Temperature Service Al-Killed Steel for High Heat Input Welding", Transactions ISIJ 25 (1985) B-157.

(51) S. Watanabe et al., "Effect of Al and B Contents on Toughness of Large Heat Input Welds of Steel Plates for Arctic Offshore Structures", Transactions ISIJ 26 (1986) B-284.

(52) "Ti-B Weld Metal for Low Temperature Service Steel Structures", Japan Ind. Technol. Bull. 9 (1981) 20.

(53) Y. Horii et al., "Development of the high-COD Titanium Boron Bearing Covered Electrodes", Fundamental and Practical Approaches to the Reliability of Welded Structures, Vol. 2. (Osaka, Japan: Japan Welding Society, 1982) 553-558.

(54) G.T. ELdis, "A Critical Review of Data Sources for Isothermal Transformation and for Continuous Cooling Transformation Diagrams", Hardenability Concepts with Applications to Steel, ed. D.V. Doane and J.S. Kirkaldy (Warrendale, PA: The Metallurgical Society of AIME, 1978) 126-148.

(55) Y.E. Smith and C.A. Siebert, "Transformation kinetics of Thermomechanically Worked Austenite by Deformation Dilatometry" Application of Modern Metallographic Techniques (American Society for Testing and Materials, STP 480, 1970) 131-151.

(56) G.L. Fisher and R.H. Geils, "A Method for Obtaining Quantitative Dilatometric Data from Alloys Undergoing a Phase Transformation," Metallography 3 (1970) 229-233.

(57) G.F. Vander Voort, Metallography: Principles and Practice (McGraw-Hill, 1984) 632-647.

(58) R.L. Bodnar, V.E. MacGraw and A.V. Brandemarte, Technique for Revealing Prior Austenite Grain Boundaries in CrMoV Turbine Rotor Steel", Metallography 17 (1984) 109-114.

(59) R.A. Storer et al., eds, Annual Book of ASTM Standards Vol. 03.01 Metals-Mechanical Testing; Elevated and Low-Temperature Tests (Philadelphia, PA: American Society for Testing and Materials, 1983).

(60) R.A. Storer et al., eds, Annual Book of ASTM Standards Vol. 03.03 Metallography; Nondestructive Testing (Philadelphia, PA: American Society for Testing and Materials, 1983).

(61) T.B. Cameron and J.E. Morral, "Methods of Detecting Boron in Steel", Boron in Steel ed. S.K. Banuji and J.E. Morral (Warrendale, PA: The Metallurgical Society of AIME, 1980) 61-79.

(62) X.L. He and Y.Y. Chu, "The Application of the $^{10}B(n,\alpha)^{7}$ Li Fission Reaction to Study Boron Bevaviour in Materials" J. Phys. D.: Appl. Phys. 16 (1983) 1145-1158.

(63) J.S. Armijo and H.S. Rosenbaum, "Boron Detection by Alpha-Particle Tracking", Journal of Applied Physics 38 (5) (1967) 2064-2069.

(64) Y.E. Smith, A.P. Coldren and R.L. Cryderman, "Manganese-Molybdenum-Niobium Acicular Ferrite Steels with High Strength and Toughness", Toward Improved Ductility and Toughness (Tokyo, Japan: The Japan Institute of Metals and Climax Molybdenum Co, 1971) 119-142.

(65) W.C. Leslie, The Physical Metallurgy of Steels, (McGraw-Hill, 1981) 201-203.

(66) F.B. Pickering, "The Spectrum of Microalloyed High Strength Low Alloy Steels", HSLA Steels: Technology and Applications (Philadelphia, PA: American Society.or Metals, (1984) 1-31.

(67) D.A. Porter and K.E. Easterling, Phase Transformations in Metals and Alloys (Wokingham, England: Van Nostrand Reinhold Co., (1981) 389-397.

(68) J.M. Dowling, J.M. Corbett and H.W. Kerr, "Inclusion Phases and The Nucleation of Acicular Ferrite in Submerged Arc Welds in High Strength Low Alloy Steels", Metallurgical Transactions 17A (9) (1986) 1611-1623.

(69) Index to the Powder Diffraction File (Philadelphia: American Society for testing and Materials).

(70) W.L. Sewer, D.R. Ireland and R.A. Wullaert, "Strength and Toughness Evaluation From an Instrumented Impact Test", (Report TR 74-29R, Effects Technology Inc., 1974).

(71) I. Kozasu, "Overview of Accelerated Cooling of Plate", Accelerated Cooling of Steel, ed. P.D. Southwick (Warrendale, PA: The Metallurgical Society of AIME, 1986) 15-31.

(72) L.E. Collins et al., "Laboratory Development of Accelerated Cooling of Microalloyed Plate Steels", Accelerated Cooling of Steel, ed. P.D. Southwick (Warrendale, PA: The Metallurgical Society of AIME, 1986) 261-282.

(73) H. Morikawa and T. Hasegawa, "Microstructures and Strengthening Factors of Accelerated Cooled Steel", Accelerated Cooling of Steel, ed. P.D. Southwick (Warrendale, PA: The Metallurgical Society of AIME 1986) 83-95.

(74) A.J. De Ardo, "The Influence of Thermomechanical Processing and Accelerated Cooling on Ferrite Grain Refinement in Microalloyed Steels", Accelerated Cooling of Steel, ed. P.D. Southwick (Warrendale, PA: THe Metallurgical Society of AIME , 1986) 97-119.

(75) O.M. Akselsen, Ø. Grong and J.K. Solbert, "Structure-Property Relationship in Intercritical Heat Affected Zone of Low-Carbon Microalloyed Steels", Material Science and Technology 3 (8) (1987) 649-655.

(76) Z. Chen, M.H. Loretto and R.C. Cochrane, "Nature of Large Precipitates in Titanium-containing HSLA Steels", Material Science and Technology 3 (10) (1987) 836-844.

(77) C. Yougi and H. Xinlai, "A Study of Austenite Grain Boundary Segregation of Boron and its Effect on the Hardenability of Steel", High Strength Low Alloy Steels, ed. D.P. Dunne and T. Chandra (Wollongong, Australia: AIME and Australian Institute of Metals, 1984) 327-331.

(78) I. Lemay and M.R. Krishnadev, "Fundamental Metallurgical Considerations", The Role of Copper in Iron and Steels, ed. I. Lemay and L. Schetky (New York: International Copper Research Association, 1980).

(79) J.D. Embury and G. Burger, "The Role of Microstructure in the fracture of Structural Steels", Inclusions and Residuals in Steels: Effects on Fabrication and Service Behaviour, ed. J.D. Boyd and C.S. Champion (CANMET and CSIRA, 1985) 265-287.

TABLE OF CONTENTS

Page

Summary 1

Chapter One: Introduction 2

Chapter Two: Review of Literature 5

2.1 Distribution of Boron in Steel 5
- 2.1.1 Boron in Solution 5
- 2.1.2 Segregation of Boron to Austenite Grain Boundaries 5
- 2.1.3 Boron Phases 7
  - Boron Nitride 7
  - Borocarbides 8
  - Other Boron-rich Phases 9

2.2 Boron Hardenability Mechanisms 10
- 2.2.1 Reduction in Austenite Grain Boundary Energy 10
- 2.2.2 Reduction in Diffusivity 10
- 2.2.3 Reduction in Number of Nucleation Sites 11
- 2.2.4 Nucleation of Ferrite on Borocarbides 11

2.3 Factors Controlling Effective Boron Content 11
- 2.3.1 Optimum Boron Content for Hardenability 13
- 2.3.2 Effects of Carbon on Boron Hardenability 13
- 2.3.3 Effects of Other Microalloying Elements on Boron Hardenability 14
- 2.3.4 Niobium Containing Boron HSLA Steels 14
  - Effects of Niobium on Recrystallization of Austenite 14
  - Effects of Niobium on Hardenability of HSLA Steels 15
  - Niobium in Boron Steels 15

- *Precipitation Kinetics of Niobium Phases* 16

2.4 Effects of Boron on Steel Properties 17
2.4.1 Applications of Boron Microalloyed Steels 17
2.4.2 Effects of Boron on Impact Toughness 18
2.4.3 Effects of Boron on Weldability 18

Chapter Three: Experimental Procedure 22

3.1 Composition and Processing of Experimental HSLA Steels 22
3.1.1 Composition 22
3.1.2 Processing 23
3.1.3 Simulation of Dilatometry Schedule on Rolling Mill 24

3.2 Deformation Dilatometry 24

3.3 Microstructural Characterization 24
3.3.1 Optical Microscopy 24
3.3.2 Scanning Electron Microscopy 25
3.3.3 Transmission Electron Microscopy 25
3.3.4 Determination of Volume Fraction of Microconstituents 26

3.4 Determination of Mechanical Properties 27
3.4.1 Tensile Properties 27
3.4.2 Impact Properties 28
3.4.3 Dynamic Fracture Toughness 28
3.4.4 Hardness Measurements 30

3.5 Determination of Boron Distribution 30

Chapter Four: Results and Discussion 43

4.1 As-Rolled and Air-Cooled Experimental Boron HSLA 43
4.1.1 Microstructure 43
4.1.2 Boron Distribution 46
4.1.3 Mechanical Properties 47

4.2 Influence of Cooling Rate on Transformation Behaviour of the Experimental Boron HSLA Steels 49
4.2.1 CCT Diagram and Typical Microstructures of Alloy 1A ... 49
4.2.2 CCT Diagram and Typical Microstructures of Alloy 5A ... 50
4.2.3 CCT Diagram and Typical Microstructures of Alloy 7A ... 51
4.2.4 Fraction Transformed vs Temperature Plots for Alloy 1A, 5A and 7A 53

4.3 Influence of Processing Parameters on the Transformation Behaviour of the Experimental Boron HSLA Steels 54
4.3.1 Comparison of As-Rolled and Air-Cooled Steels with the CCT Diagram Results 54
4.3.2 Effects of Dilatometer Processing Schedule on the Transformation Behaviour 55
- Effect of Deformation Schedule 55
- Effect of Holding Time Between Deformation Steps 57
4.3.3 Effects of the Boron Distribution Prior to Processing on the Transformation Behaviour 58
- Nature of the Starting Material 58
- Effect of Austenizing Practice 60
4.3.4 Simulation of the Dilatometer Testing on the Rolling Mill. 61
4.3.5 Microstructure of the Experimental Boron HSLA Steels in the As-Cast State 62

4.4 Influence of Effective Boron Content on the Transformation Behaviour of the Experimental Boron HSLA Steels 63

4.5 As-rolled and Accelerated Cooled Experimental Boron HSLA Steels 65
4.5.1 Review of Accelerated Cooling 65
4.5.2 Microstructure 67
4.5.3 Mechanical Properties 68

4.6 Experimental Cu-Mo-B HSLA Steels 71
4.6.1 Microstructure 71
4.6.2 Mechanical Properties 72

4.6.3 Comparison of Cu-Mo- B Steels with Other Experimental Boron Alloys 73
4.6.4 Effects of Heat Treatment on Experimental Boron HSLA Steels 74

Chapter Five: Conclusion 145

5.1 Major Conclusions Arising From this Study 145

5.2 Industrial Applications 147

5.3 Recommandations for Further Work 150

Appendix A: Identification of Precipitates by Analysis of Electron Diffraction Patterns 151

References 156

Table of contents 164